MNRAS **533**, 4104–4149 (2024) Advance Access publication 2024 September 3



Downloaded from https://academic.oup.com/mnras/article/533/4/4104/7748750 by guest on 25 November 2024

Survey of complex organic molecules in starless and pre-stellar cores in the Perseus molecular cloud

Samantha Scibelli ¹⁰, ^{1,2}★† Yancy Shirley ¹⁰, Andrés Megías ¹⁰ and Izaskun Jiménez-Serra ¹⁰

Accepted 2024 August 19. Received 2024 August 2; in original form 2024 May 23

ABSTRACT

Cold (\sim 10 K) and dense ($\sim 10^5$ cm⁻³) cores of gas and dust within molecular clouds, known as starless and dynamically evolved pre-stellar cores, are the birthplaces of low-mass ($M \le$ few M_{\odot}) stars. As detections of interstellar complex organic molecules, or COMs, in starless cores has increased, abundance comparisons suggest that some COMs might be seeded early in the star formation process and inherited to later stages (i.e. protostellar discs and eventually comets). To date observations of COMs in starless cores have been limited, with most detections reported solely in the Taurus molecular cloud. It is therefore still a question whether different environments affect abundances. We have surveyed 35 starless and pre-stellar cores in the Perseus molecular cloud with the Arizona Radio Observatory (ARO) 12 m telescope detecting both methanol, CH₃OH, and acetaldehyde, CH₃CHO, in 100 per cent and 49 per cent of the sample, respectively. In the sub-sample of 15 cores where CH₃CHO was detected at $> 3\sigma$ (~18 mK) with the ARO 12 m, follow-up observations with the Yebes 40 m telescope were carried out. Detections of formic acid, t-HCOOH, ketene, H2CCO, methyl cyanide, CH3CN, vinyl cyanide, CH2CHCN, methyl formate, HCOOCH3, and dimethyl ether, CH₃OCH₃, are seen in at least 20 per cent of the cores. We discuss detection statistics, calculate column densities, and compare abundances across various stages of low-mass star formation. Our findings have more than doubled COM detection statistics in cold cores and show COMs are prevalent in the gas before star and planet formation in the Perseus molecular cloud.

Key words: astrochemistry – stars: formation – ISM: molecules.

1 INTRODUCTION

The detection of organic molecules in the interstellar medium (ISM) is intriguing, since these molecules are key to understanding the origins and evolution of organic chemistry, the basis for life on Earth. The complexity of organic molecules detected in the ISM has grown significantly over the years, from the simple diatomic carbon monoxide (CO; Wilson, Jefferts & Penzias 1970) to large rings such as the polycyclic aromatic hydrocarbon benzonitrile (c-C₆H₅CN; McGuire et al. 2018).

An organic molecule observed in the ISM is traditionally considered complex if it has more than five atoms and at least one carbon-atom (Herbst & van Dishoeck 2009). These interstellar complex organic molecules, or COMs, have been observed for a long time to be abundant in dynamic star-forming environments such as towards the Galactic Center (Ball et al. 1970; Brown et al. 1975; Gardner & Winnewisser 1975; Hollis, Lovas & Jewell 2000; Requena-Torres et al. 2008; Zeng et al. 2018; Jiménez-Serra et al. 2020; Rivilla et al. 2022), as well as towards the star forming region in the Orion Nebula (Snyder et al. 1974; Kolesniková et al. 2014; Sakai, Kobayashi & Hirota 2015).

Beyond these quintessential regions, it is also the prevalence of COMs, and their relevance to pre-biotic chemistry, in the earliest

† Jansky Fellow of the National Radio Astronomy Observatory.

stages of low-mass $(M \le \text{few } M_{\odot})$ star and planet formation that has sparked the interest of astrochemists and astrobiologists. COMs have now been detected in virtually each stage of the low-mass star formation process, including low-mass protostars (Öberg et al. 2011; Taquet et al. 2015; Imai et al. 2016; López-Sepulcre et al. 2017), protoplanetary discs (Walsh et al. 2016; Favre et al. 2018; Loomis et al. 2018), the atmospheres of solar system moons (Lai et al. 2017; Thelen et al. 2020), and comets (Biver & Bockelée-Morvan 2019; Rubin et al. 2019; Schuhmann et al. 2019).

To best probe the initial chemical conditions at the earliest stage of low-mass star formation, it is imperative to study cold (10 K) and dense (105 cm⁻³) starless cores and pre-stellar cores (e.g. Bergin & Tafalla 2007). A starless core is used as a generic term for any dense cold core, whereas pre-stellar cores are those that have overcome turbulence, thermal and magnetic pressure and will eventually dynamically collapse due to gravity and external cloud pressure to form an infant star. Planetesimals are likely to inherit at least some of their organic chemistry from the starless and pre-stellar core phase, which can in turn drive additional chemical complexity in later stages of star and planet formation (Drozdovskaya et al. 2019; van Gelder et al. 2020; Booth et al. 2021; Scibelli et al. 2021). Observational constraints on the complex molecular content of starless and pre-stellar cores are therefore important for piecing together the astrochemical origins of the composition of solar and planetary systems (Öberg & Bergin 2021).

In hotter regions, during the 'warm-up' of ices on the outer layers of grains at temperatures of 20-40 K, it has been shown that

¹National Radio Astronomy Observatory, 520 Edgemont Road, Charlottesville, VA 22903, USA

²Steward Observatory, University of Arizona, 933 North Cherry Avenue, Tucson, AZ 85721, USA

³Centro de Astrobiología (CAB), CSIC-INTA, Carretera de Ajalvir, km 4, E-28805 Torrejón de Ardoz, Spain

^{*} E-mail: sscibell@nrao.edu

COMs can form and be released into the gas-phase through thermal desorption and/or diffusive surface radical chemistry facilitated by UV radiation from cosmic rays (see reviews Jørgensen, Belloche & Garrod 2020; Ceccarelli et al. 2022). For cold (10 K) and quiescent starless and pre-stellar cores, alternative models with gas-phase reactions of smaller species, namely CH₃OH and smaller radicals, have been developed to explain how additional COMs form (Vasyunin & Herbst 2013; Balucani, Ceccarelli & Taquet 2015). Updated models for COMs support this formation process called reactive desorption, where the precursor molecules form on icy surfaces of interstellar grains, and then get ejected into the gas to form larger molecules (Minissale et al. 2016; Vasyunin et al. 2017).

Attempts to use the Minissale et al. (2016) and Vasyunin et al. (2017) models to match the high abundances of COMs observed towards younger and less dense starless cores, such as L1521E, overpredict CH₃OH and underpredict larger COMs (e.g. see Scibelli et al. 2021). Models with updated non-diffusive surface reaction networks (Jin & Garrod 2020; Garrod et al. 2022), as well as the addition of cosmic ray chemistry (Shingledecker et al. 2018), supply additional mechanisms for getting these large COMs off the grains into the gas-phase, but have only been tested against few well-known cold cores (i.e. L1544 and TMC-1; see Vasyunin et al. 2017; Shingledecker et al. 2018; Jin & Garrod 2020). To guide these modeling efforts and constrain COM formation routes, additional abundance constraints from a larger sample of starless and pre-stellar cores are needed to compare to models.

Much of the search for COMs in starless and pre-stellar cores in low-mass star forming environments has been restricted to the Taurus molecular cloud. It is in Taurus where the famous cold (10 K) dark cloud TMC-1 resides, which has a rich inventory of complex chemistry (Matthews, Friberg & Irvine 1985; Kaifu et al. 2004; Soma et al. 2015, 2018; McGuire et al. 2018, 2021; Agúndez et al. 2021; Cernicharo et al. 2021). Additionally, within Taurus is the chemically and dynamically evolved pre-stellar core L1544, which shows high levels of CO depletion and high central densities $> 10^7$ cm⁻³ (Caselli et al. 1999, 2019; Crapsi et al. 2007; Keto & Caselli 2010), and many COM detections (e.g. species such as acetaldehyde, CH₃CHO, methyl formate, CH₃OCHO, dimethyl ether, CH₃OCH₃, and vinyl cyanide, CH₂CHCN; Vastel et al. 2014; Jiménez-Serra et al. 2016). More recently, there were numerous COM detections in the chemically young core L1521E (Scibelli et al. 2021) as well as nitrogen bearing (N-bearing) COMs observed in the dynamically young core L1498 (Jiménez-Serra et al. 2021), both in Taurus. Megías et al. (2023) have suggested a scenario in which N-bearing and oxygen bearing (O-bearing) COMs form at different stages in the evolution of starless cores. However, the number of cores studied by these authors was small. Beyond these few case studies, Scibelli & Shirley (2020) conducted a survey towards 31 starless and pre-stellar cores in the L1495 filament of the Taurus molecular cloud, finding a prevalence of both methanol, CH₃OH, in 100 per cent of the cores targeted and CH₃CHO in 70 per cent. It is still unknown whether Taurus is a unique environment and if other molecular clouds show a similar prevalence of COMs in a larger sample of starless and pre-stellar cores.

For this study we have focused on conducting a survey of COMs towards 35 starless and pre-stellar cores in the Perseus molecular cloud. Perseus is one of the most studied active nearby (\sim 300 pc) star-forming regions, with recent *Herschel* cataloging finding a total 684 starless and pre-stellar cores and 132 protostars (Class 0, I, and II) in the region (Pezzuto et al. 2021). It is important to note that it is in Perseus where the first COM detections near the dense star-forming core B1-b were observed, in close proximity (within \sim 30 arcsec) to a protostar and outflow (Öberg et al. 2010; Cernicharo et al. 2012).

Recent focus has been on the COM content of protostars in Perseus, with studies such as the CALYPSO survey which looked at 26 solar-type protostars (Belloche et al. 2020), and the complementary Perseus ALMA Chemistry Survey, or PEACHES, which probed warm-phase complex chemistry towards 50 embedded protostars in Perseus finding COM emission in 58 per cent of the sources (Yang et al. 2021). Here we investigate whether we see a similar prevalence of chemical complexity during the cold gas-phase chemistry within starless and pre-stellar cores in the same cloud.

We begin by detailing in Section 2 the source selection and catalogue matching for each of the starless and pre-stellar cores targeted in the survey. Then, we describe the molecular line observations and data reduction techniques in Section 3. The detection statistics and column density calculations are presented in Section 4. In Section 5 we analyse COM abundances correlations, compare COM abundances to starless and pre-stellar cores in other molecular clouds as well as to objects at other stages of low-mass star formation, and discuss the implications for COM formation routes. We summarize and conclude in Section 6.

2 SOURCE SELECTION

Each of the 35 starless and pre-stellar cores targeted first by the ARO 12 m were selected by cross-referencing with Perseus core catalogues compiled from Bolocam 1.1 mm continuum maps (Enoch et al. 2008), ammonia, NH₃, observations (Rosolowsky et al. 2008), as well as the higher resolution Herschel core catalogue (Pezzuto et al. 2021). We include cores that have corresponding NH₃ data because this molecule does not appear to be affected by dramatic freeze-out like CO does until high densities (> 10⁶ cm⁻³; Caselli et al. 2022; Pineda et al. 2022; Lin et al. 2023), making it a useful probe of structure as well as kinetic temperature, T_k in dense pre-stellar cores (Tafalla et al. 2002; Seo et al. 2015; Friesen et al. 2017; Chen et al. 2019a, b, 2020). Additionally, the 31 starless and pre-stellar cores in the Taurus molecular cloud that were targeted in the Scibelli & Shirley (2020) survey were also selected based on NH₃ mapping results from Seo et al. (2015). For the 35 cores in Perseus we target, T_k ranges from 9.5 to <20 K and the NH₃ column density, $N_{\rm NH_2}$, ranges from 0.6–89 × 10¹³ cm⁻² (Rosolowsky et al. 2008).

In Table 1 the core numbers for each catalogue are listed, and we refer to each core by their Herschel number and corresponding coordinates throughout the remainder of the paper. It should be noted that in some cases the corresponding NH₃ peak is slightly offset from the Herschel peak. Observations with the Green Bank 100 m dish probing how NH₃ follows the dust (from SCUBA observations) also show that in a sample of these cores there are slight offsets in the peak positions (Morgan et al. 2014), but negligible within our single-dish beam sizes. For consistency, it is the Herschel dust peak position that is used when carrying out our observations. The coordinates of each of the starless and pre-stellar cores were also checked to make sure there was no overlap (within an ARO 12 m 62 arcsec beam) with any other core, including protostellar sources, that were listed in Pezzuto et al. (2021) and this narrowed our catalogue down to the final 35 cores. The Herschel data provides us with corresponding H_2 column density, $N(H_2)$, information as well as dust temperatures, T_{dust} , for each core, with T_{dust} ranging from 8 to 15 K, peak $N(H_2)$ ranging from $0.45-23 \times 10^{22} \text{ cm}^{-2}$ and core masses ranging from 0.3–5.5 M_{\odot} (Pezzuto et al. 2021). In the cases where T_k is uncertain, and only an upper limit is provided in Rosolowsky et al. (2008), we use the T_{dust} value (see Table 1). In general, T_k and T_{dust} do not differ by more than a factor of 1.6.

Table 1. Perseus starless and pre-stellar core catalogue.

Region	Core # ¹ (<i>Herschel</i>)	Core # ² (NH ₃)	Core # ³ (Bolocam)	RA ⁴ (J2000)	DEC ⁴ (J2000)	D ⁵ (pc)	$N(\rm H_2)^6$ $10^{22} \rm cm^{-2}$	$n({\rm H_2})^6$ $10^5~{\rm cm}^{-3}$	$T_{ m k}^{\ 7}$ K
L1451	54	6	Per-Bolo4	03:25:17.89	+ 30:18:56.6	283	1.10	0.40	10.3
	67	11	Per-Bolo7	03:25:35.11	+30:13:12.8	283	1.38	0.52	10.4*
L1455	130	24	Per-Bolo19	03:27:02.78	+30:15:21.7	286	0.95	0.35	10.4
	231	42	Per-Bolo27	03:28:34.16	+30:19:38.8	286	1.02	0.38	10.7
	256	49	Per-Bolo32	03:28:43.14	+30:31:08.6	286	1.07	0.40	10.5*
NGC1333	264	51	Per-Bolo34	03:28:47.14	+31:15:11.4	294	2.06	0.75	10.8
	317	69	Per-Bolo44	03:29:04.93	+31:18:44.4	294	2.63	0.96	13.6
	321	72	Per-Bolo45	03:29:07.17	+31:17:22.1	294	3.65	1.33	12.6
	326	73	Per-Bolo46	03:29:08.97	+31:15:17.2	294	7.88	2.87	12.3
	339	79	Per-Bolo50	03:29:15.81	+31:20:31.6	294	2.11	0.77	15.5
	344	82	Per-Bolo53	03:29:18.39	+31:25:07.2	294	1.46	0.53	11.9
	355	86	Per-Bolo56	03:29:23.77	+31:36:12.6	294	1.02	0.37	9.8
Per6	398	93	Per-Bolo61	03:30:25.08	+30:27:42.6	290	0.82	0.30	10.5
B1	413	96	Per-Bolo63	03:30:46.74	+30:52:44.8	297	1.17	0.42	10.5
	414	97	Per-Bolo64	03:30:50.76	+30:49:21.6	297	0.48	0.17	9.8
	479	108	Per-Bolo70	03:32:43.72	+30:59:48.5	297	2.56	0.93	10.2
	491	117	Per-Bolo76	03:33:10.91	+31:21:44.7	297	1.00	0.36	10.8*
	504	124	Per-Bolo82	03:33:25.31	+31:05:37.5	297	1.80	0.65	9.7
B1-E	543	132	Per-Bolo87	03:35:23.02	+31:06:50.6	301	0.67	0.24	11.7*
IC348	615	141	Per-Bolo88	03:40:14.92	+32:01:40.8	314	1.03	0.35	10.3*
	627	142	Per-Bolo89	03:40:49.53	+31:48:40.5	314	0.93	0.32	12.4
	642	144	Per-Bolo91	03:41:20.42	+31:47:32.7	314	0.69	0.24	13.3*
	656	145	Per-Bolo92	03:41:40.64	+31:58:05.4	314	0.97	0.33	9.5
	657	146	Per-Bolo93	03:41:45.86	+31:48:10.8	314	0.87	0.30	10.3*
	658	147	Per-Bolo94	03:41:46.68	+31:57:29.4	314	0.81	0.28	9.6
	709	156	Per-Bolo99	03:43:38.06	+32:03:07.4	314	1.48	0.51	13.5
	715	158	Per-Bolo101	03:43:46.34	+32:01:43.5	314	1.45	0.49	14.8
	739	168	Per-Bolo109	03:44:05.28	+32:00:38.8	314	1.53	0.52	9.2*
	746	170	Per-Bolo111	03:44:14.38	+31:58:00.7	314	1.42	0.49	10.6
	747	171	Per-Bolo112	03:44:15.08	+32:09:13.1	314	0.71	0.24	12.9
	752	174	Per-Bolo114	03:44:23.10	+32:10:01.0	314	0.63	0.22	14.7
	768	180	Per-Bolo117	03:44:48.83	+ 32:00:31.6	314	1.43	0.49	10.8
HPZ6	780	183	Per-Bolo119	03:45:16.47	+ 32:04:47.6	318	0.98	0.33	10.7
B5	799	188	Per-Bolo121	03:47:31.31	+32:50:56.9	325	1.01	0.33	10.4
	800	192	Per-Bolo122	03:47:38.97	+32:52:16.6	325	1.93	0.64	11.7

Note. Catalogue of Herschel cores for the Perseus region (Pezzuto et al. 2021). Rosolowsky et al. (2008) provided a list of NH₃ clumps for the Perseus region. Bolocam naming convention for the Perseus cores is from Enoch et al. (2008). ARA and DEC values in this table are those that correspond with the most recent Herschel data. Distance, D, is the mean distance for that particular region as listed in table 5 in Pezzuto et al. (2021). Median value from Herschel maps within the ARO 12m 62 arcsec beam. Kinetic temperature values for RADEX calculations derived from NH₃ as in Rosolowsky et al. (2008), except for cores marked by where only upper limits are presented and instead the HerschelT_{dust} value is used [table A.2. in Pezzuto et al. (2021)].

The starless and pre-stellar cores targeted in this survey span across the entire \sim 10 pc of Perseus and thus different distances need to be adopted for each individual sub-region. For example, the eastern region of IC348 and the western region of NGC1333 are at different distances of 321 \pm 10 pc and 293 \pm 22 pc, respectively, according to Ortiz-León et al. (2018), who use VLBA and Gaia data. Zucker et al. (2019) went on to derive a distance map of Perseus (along with other clouds) using 'per-star distance-extinction estimates' along with stellar distances from Gaia Data Release 2 (DR2) parallax measurements (Gaia Collaboration 2016, 2018), and find similarly distances in Perseus range from 234 to 331 pc. For this paper we adopt the mean distance for each sub-region based on more recent distances also derived from Gaia DR2 results as described in Pezzuto et al. (2021), and listed here in column 7 of Table 1. These distances agree well within < 10 per cent to those derived in both Ortiz-León et al. (2018) and Zucker et al. (2019).

Lastly, we note that each core has been labelled 'pre-stellar' in the *Herschel* catalogue, based first on the fact that no internal source of energy (e.g. protostar) is present and on if the core's self-gravity exceeds its pressure support. Because there is increasing evidence to suggest that gravity is not the only term that should be considered when determining if a core is likely to form a star (Galloway-Sprietsma et al. 2022; Offner et al. 2022; Pattle et al. 2023; Scibelli et al. 2023), we continue to refer to these objects as a whole as both 'starless and pre-stellar' cores. In Fig. 1 the location of each starless and pre-stellar core is labelled.

3 OBSERVATIONS AND DATA REDUCTION

Molecular line observations of COMs were taken with the Arizona Radio Observatory (ARO) Telescope 12 m dish on Kitt Peak outside of Tucson, Arizona as well as with the 40 m radio telescope of the Yebes Observatory (Guadalajara, Spain), known as the Yebes 40 m. Lines targeted and analysed in this paper are listed in Table 2.

3.1 ARO 12 m

Single pointing observations on the ARO 12 m for all 35 sources (Table 1 and Fig. 1) were carried out from 2021 October to 2022 April and again from April to May of 2023 with the 3 mm sideband

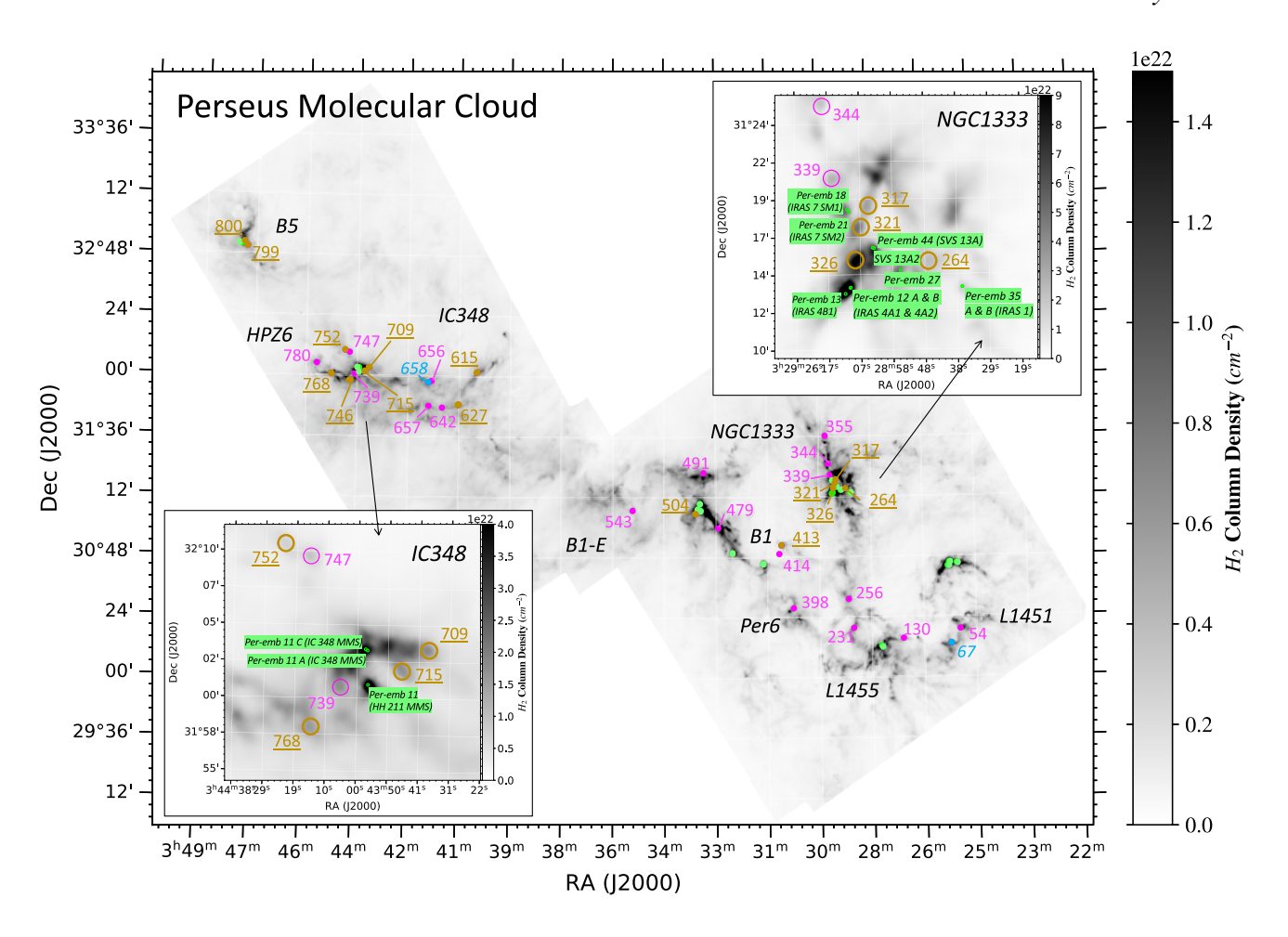


Figure 1. Perseus molecular cloud H_2 column density map from *Herschel* (Pezzuto et al. 2012; Sadavoy et al. 2012, 2014). Overplotted are the numbered starless and pre-stellar cores observed (pink, gold, and orange points) and those with underlined labels (in gold) have had successful ARO 12 m CH₃CHO detections at the $\sigma_{T_{mb}} = 6$ mK level and were followed up with the Yebes 40 m telescope. Labels for cores 67 and 658 are italicized (labelled in blue), denoting these are the cores that were followed up with additional ARO 12 m observations probing down to $\sigma_{T_{mb}} = 2.5$ mK. The remaining labels for the denoted starless and pre-stellar cores are not underlined or italicized (in magenta). In all cores CH₃OH has been detected. For comparison, as smaller circles (in green) are the locations of the 27 protostars from the PEACHES sample with CH₃OH detections (see their table 5 in Yang et al. 2021). The apparent overlap in sources is a projection effect, as seen from the zoom-in insert panels for regions IC348 and NGC1333. The size of the starless and pre-stellar core circles are at a FWHM of 62 arcsec.

separating dual polarization receiver. Each scan was 5 min using absolute position switching (APS) between the source and the off position void of emission every 30 s. Pointing was checked every $\sim\!1\text{--}2\,h$ on a nearby quasar or planet. The AROWS spectrometer, with a resolution of 39 kHz, was used for all observations with the two polarizations (vertical and horizontal) tuned to simultaneously observe favourable transitions of CH₃OH, CH₃CHO, and CH₂CHCN (see Table 2). An error/noise level of at least 10 per cent in brightness temperature was adopted based on the monitoring of standard sources (see Fig. A1 in Appendix A).

Data reduction was performed using the CLASS program of the GILDAS package (Pety 2005; Gildas Team 2013). For each polarization, a median efficiency percentage for each planet was calculated, along with estimated errors, during the different observing season and ranged from $\sim 80-89$ per cent (see Appendix A). A main beam temperature was set by this beam efficiency, η , where $T_{\rm mb} = T_A^*/\eta$ (Mangum 1993). The baselined, hanning smoothed (by 2 channels), and scaled spectra were then fit with Gaussian line profiles within the

CLASS routine and plotted using the MATPLOTLIB package (Hunter 2007) in PYTHON. The reduced spectra and Gaussian fits for the detected transitions of CH₃OH and CH₃CHO are plotted in Figs 2 and 3, respectively (detection statistics detailed in Section 4.1). In Fig. 1 the locations of each core are labelled based on CH₃CHO detections and, for additional reference, the location of the protostellar sources with at least CH₃OH detected from the PEACHES sample is also shown (Yang et al. 2021).

3.2 Yebes 40 m

Follow-up observations for 15 of the 35 cores with initial ARO $12 \,\mathrm{m}$ CH₃CHO detections ($\sigma_{T_{\mathrm{mb}}} = 6 \,\mathrm{mK}$; see Section 4.1) were done with the Yebes 40 m telescope during the 2022 spring and 2023 spring seasons (projects 22A022 and 23A025; PI: Scibelli). Each core was observed with the dual (horizontal and vertical) linear polarization Q-band receiver (Tercero et al. 2021) using the frequency switching technique with a standard throw of $10.52 \,\mathrm{MHz}$. The wideband nature of the receiver allows for a total bandwidth of $18.5 \,\mathrm{GHz}$ spanning from 31.5– $50 \,\mathrm{GHz}$ (6–9 mm) with a resolution of $38.0 \,\mathrm{kHz}$ (0.38 km s⁻¹–0.23 km s⁻¹). Pointing corrections were obtained by

³http://iram.fr/IRAMFR/GILDAS/

Table 2. COM line list.

Telescope: Receiver	Molecule	Transition	Rest frequency, ν (GHz)	E_u/k (K)	g_u	A_{ul} (s ⁻¹)	$\theta_{ m beam}^{-1}$ arcsec
ARO 12 m: 3 mm							
	CH ₃ OH	$2_{-1,2} - 1_{-1,1} E$	96.739363	12.5	20	2.6E-06	62.3
		$2_{0,2} - 1_{0,1} A$	96.741377	7.0	20	3.4E-06	62.3
		$2_{0,2} - 1_{0,1}$ E	96.744549	20.1	20	3.4E-06	62.3
	CH ₃ CHO	$5_{0,5} - 4_{0,4} E$	95.947439	13.9	22	3.0E-05	62.8
		$5_{0,5} - 4_{0,4} \text{ A}$	95.963465	13.8	22	3.0E-05	62.8
	CH ₂ CHCN	$10_{0,10} - 9_{0,9}$	94.276641	24.9	63	6.2E-05	64.0
		$10_{1,9} - 9_{1,8}$	96.982446	27.8	63	7.2E-05	62.2
Tebes 40 m: Q-band							
	t-HCOOH	$2_{1,2} - 1_{1,1}$	43.303709	6.2	5	5.7E-07	41.8
		$2_{0,2} - 1_{0,1}$	44.911750	3.2	5	8.2E-07	40.3
		$2_{1,1} - 1_{1,0}$	46.581226	6.5	5	7.1E-07	38.8
	H_2CCO	$2_{1,2} - 1_{1,1}$ o-	40.039022	15.9	15	4.5E-07	45.2
		$2_{0,2} - 1_{0,1}$ p-	40.417950	2.9	5	6.2E-07	44.8
		$2_{1,1} - 1_{1,0}$ o-	40.793832	16.0	15	4.7E-07	44.3
	CH_3OH	$1_{0,1} - 0_{0,0}$ A	48.372460	2.3	12	3.6E-07	37.4
		$1_{-0,1} - 0_{-0,0}$ E	48.376887	15.4	12	3.6E-07	37.4
	CH ₃ CN	$2_1 - 1_1$	36.794765	9.8	10	1.8E-06	49.2
		$2_0 - 1_0$	36.795474	2.6	10	2.5E-06	49.2
	CH ₃ CHO	$2_{1,2} - 1_{1,1} A$	37.464204	4.9	10	1.2E-06	48.3
		$2_{1,2} - 1_{1,1} E$	37.686932	5.0	10	1.1E-06	48.0
		$2_{0,2} - 1_{0,1}$ E	38.506035	2.8	10	1.7E-06	47.0
		$2_{0,2} - 1_{0,1}$ A	38.512079	2.8	10	1.7E-06	47.0
		$2_{1.1} - 1_{1.0} E$	39.362537	5.2	10	1.3E-06	46.0
		$2_{1,1} - 1_{1,0} A$	39.594289	5.1	10	1.4E-06	45.7
	CH ₂ CHCN	$4_{1.4} - 3_{1.3}$	37.018922	6.6	27	3.6E-06	48.9
		$4_{0,4} - 3_{0,3}$	37.904849	4.5	27	4.1E-06	47.7
		$4_{2,3} - 3_{2,2}$	37.939620	13.2	27	3.1E-06	47.7
	$HCOOCH_3$	$3_{0,3} - 2_{0,2}$ E	36.102224	3.5	14	6.2E-07	50.1
		$3_{0,3} - 2_{0,2} A$	36.104793	3.5	14	6.2E-07	50.1
		$3_{2,2}-2_{2,1}$ E	36.678607	6.2	14	3.3E-07	49.3
		$3_{2,2} - 2_{2,1} A$	36.657467	6.2	14	3.6E-07	49.3
		$4_{1,4} - 3_{1,3}$ E	45.395795	6.1	18	1.2E-06	39.8
		$4_{1.4} - 3_{1.3} \text{ A}$	45.397380	6.1	18	1.2E-06	39.8
		$4_{0,4} - 3_{0,3}$ E	47.534093	5.8	18	1.5E-06	38.1
		$4_{0,4} - 3_{0,3}$ A	47.536915	5.8	18	1.5E-06	38.0
	CH ₃ OCH ₃	$3_{1,2} - 3_{0,3}$	32.977274	7.0	70	3.4E-07	54.8
		AE + EA					
		$3_{1,2} - 3_{0,3}$ EE	32.978232	7.0	112	3.4E-07	54.8
		$3_{1,2} - 3_{0,3}$ AA	32.979187	7.0	70	3.4E-07	54.8
		$4_{1,3} - 4_{0,4}$ AE + EA	35.592414	10.8	54	4.0E-07	50.8
		$4_{1,3} - 4_{0,4}$ EE	35.593408	10.8	144	4.0E-07	50.8
		$4_{1.3} - 4_{0.4} \text{ AA}$	35.594402	10.8	54	4.0E-07	50.8

Note. Values for CH₃CN, CH₃CHO, and HCOOCH₃ from JPL catalogue¹ (Pickett et al. 1998) and for the remaining transitions from CDMS data base² (Müller et al. 2001, 2005; Endres et al. 2016). ¹The beam size corresponding to the selected molecular transition.

observing strong nearby quasars or SiO masers during each observing

Once the data were obtained, they were inspected, reduced, and put on the main beam temperature, $T_{\rm mb}$, scale using publicly available PYTHON-based scripts⁴ developed by Megías et al. (2023), which invokes the CLASS program of the GILDAS package for the combining of the spectra (see Appendix B for more detail). Then, additional CLASS scripts were run to search for the following COMs (Tables 2 and B1): the five-atom precursor COMs formic acid; t-HCOOH, and ketene;

 H_2CCO , which for simplicity we will continue to label as 'COMs,' as well as the six-atom COMs CH₃OH, methyl cyanide; CH₃CN, and the even larger species CH₃CHO, CH₂CHCN, HCOOCH₃, and CH₃OCH₃, in order to compare to literature values (Vastel et al. 2014; Jiménez-Serra et al. 2016, 2021; Scibelli & Shirley 2020; Scibelli et al. 2021; Megías et al. 2023). The online tool SPLATALOGUE⁵ was used to identify COM transitions, where the molecular data come from the Cologne Database of Molecule Spectroscopy (CDMS; Müller et al. 2001, 2005; Endres et al. 2016) and the Jet Propulsion

¹https://spec.jpl.nasa.gov/

²https://cdms.astro.uni-koeln.de

⁴https://github.com/andresmegias/gildas-class-python/

⁵https://splatalogue.online

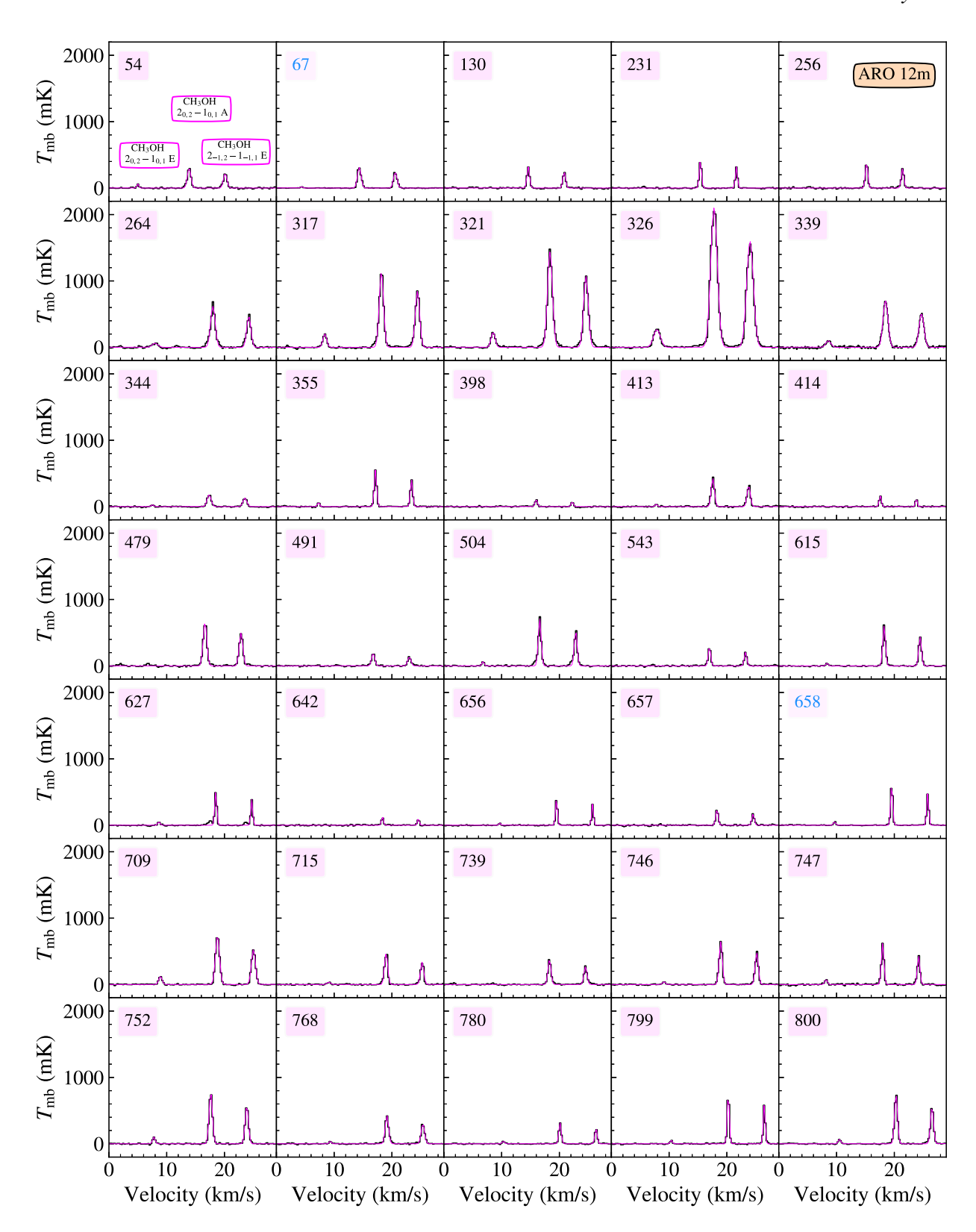


Figure 2. Methanol, CH₃OH, spectrum (in black) in units of $T_{\rm mb}$ (K) versus velocity (km s⁻¹) from the ARO 12 m for each of the 35 starless and pre-stellar cores targeted in this Perseus survey. Core numbers are labelled in the upper left of each panel. Gaussian fits are overplotted (in magenta). There are three 2–1 transitions observable in the spectral window, labelled in the uppermost left panel. Longer integration time on cores 67 and 658 (also labelled in blue), resulted in RMS values around $\sigma_{T_{\rm mb}} = 3$ mK. For the remaining cores, the average RMS value is $\sigma_{T_{\rm mb}} = 7$ mK.

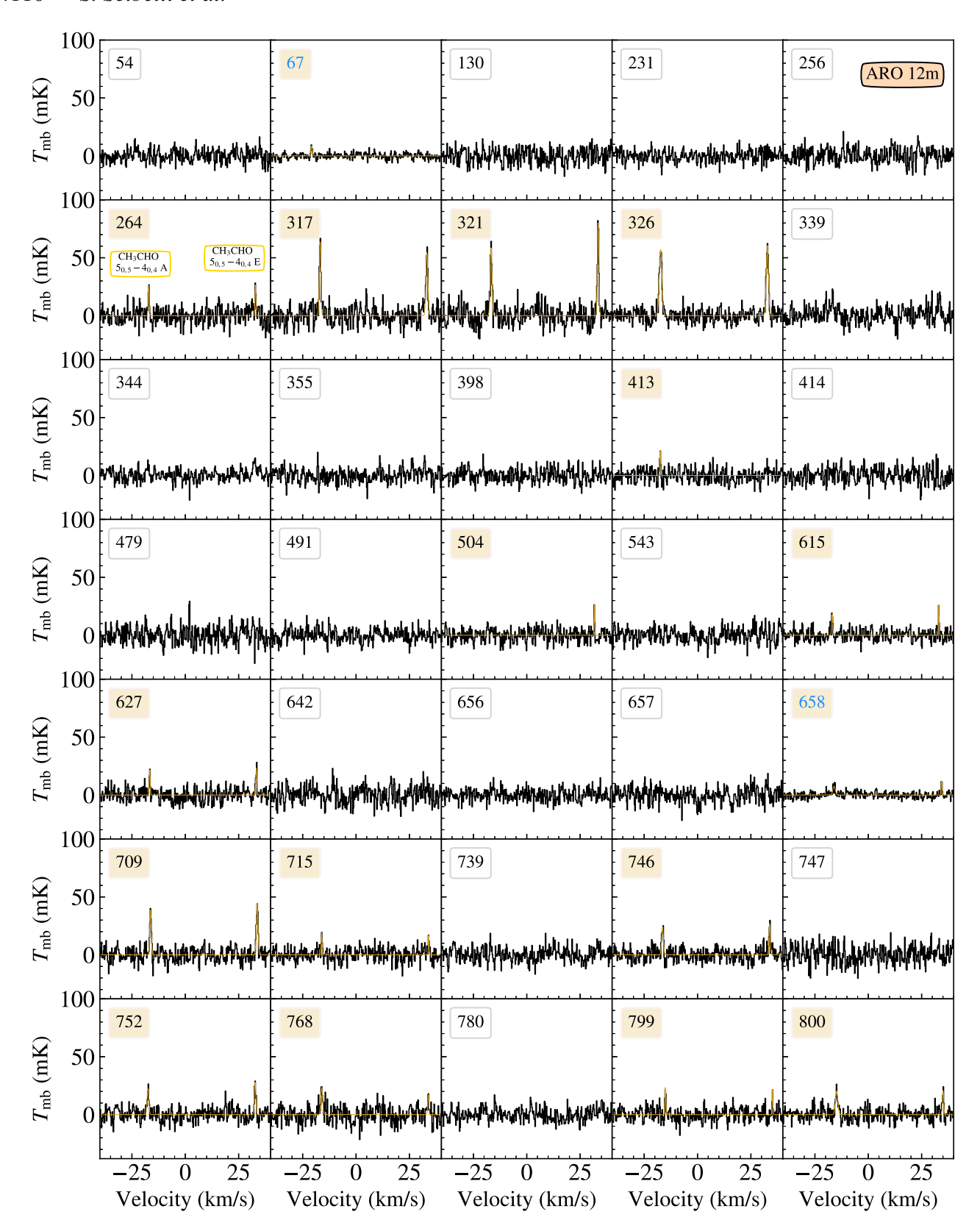


Figure 3. Acetaldehyde, CH₃CHO, spectrum (in black) in units of $T_{\rm mb}$ (K) versus velocity (km s⁻¹) from the ARO 12m for each of the 35 starless and pre-stellar cores targeted in this Perseus survey. Core numbers are labelled in the upper left of each panel. Gaussian fits are overplotted (in gold). There are two 5–4 transitions observable in the spectral window, labelled in the first column of the second row panel. Longer integration time on cores 67 and 658 (also labelled in blue), resulted in RMS values around $\sigma_{T_{\rm mb}} = 2.5$ mK. For the remaining cores, the average RMS value is $\sigma_{T_{\rm mb}} = 6$ mK.

Laboratory Millimeter and Submillimeter Spectral Line catalogue (JPL; Pickett et al. 1998). We note that while additional complex molecules lie within our data set, such as large carbon-chains and cyanopolyynes, these species will be the subject of subsequent papers. In general, the $\sigma_{T_{mh}}$ values range from $\sim 2-9$ mK.

4 RESULTS

The main result from this survey is that gas-phase COMs are detectable and prevalent in cold ($\sim 10\,\mathrm{K}$) starless and pre-stellar cores across the Perseus molecular cloud. In most of the cores the smaller COMs (<7-atom and 7-atom O-bearing) are detected, and in only a handful are higher complexity COMs (7-atom N-bearing and > 8-atom O-bearing) also seen. Below we detail the detection statistics and calculate column densities, for both the full ARO 12 m sample and the Yebes 40 m sub-sample.

4.1 Detection statistics: ARO 12 m

From our preliminary ARO 12 m survey, which had baseline RMS levels of $\sigma_{T_{\rm mb}} = 5-8$ mk, we found in 100 per cent (35/35) of the cores CH₃OH was detected, in 43 per cent (15/35) CH₃CHO was detected, and in 0 per cent of the cores (0/35) was CH₂CHCN detected. In general, the cores with the strongest detections (i.e. the brightest $T_{\rm mb}$ values) of CH₃OH had the strongest CH₃CHO detections (see Figs 2 and 3). A deeper search towards two of the cores (67 and 658) that both had no initial CH₃CHO detection was then carried out to achieve RMS values of $\sigma_{T_{\rm mb}} = 2-3$ mK. In both cores CH₃CHO was detected bringing the detection statistic up to 49 per cent. It is important to note that for each of these deeper integration's on core 67 and core 658, it took > 60 h and therefore additional integration on the 18 remaining sources with no CH₃CHO detections at the $\sigma_{T_{\rm mb}} = 6$ mK level was not possible.

We also report that across the sample, in 31 per cent (11/35) of the cores the weakest CH₃OH line ($2_{0,2} - 1_{0,1}$ E) was not detected above the 3σ limit. And, for core 504 only the $5_{0,5} - 4_{0,4}$ E state of CH₃CHO was detected above the 3σ limit, while for cores 67 and 413 we only report the $5_{0,5} - 4_{0,4}$ A state with $> 3\sigma$ confidence [note: similar to cores 11, and 20, 21 in Scibelli & Shirley (2020)].

At a distance of 135 pc (Schlafly et al. 2014) the Taurus Molecular Cloud survey detected CH₃OH in 100 per cent and CH₃CHO in 70 per cent of the 31-core sample (Scibelli & Shirley 2020). Both the Taurus and Perseus surveys looked at these same lines with the ARO 12 m at similar $\sigma_{T_{\rm mb}}$ levels \sim 7 mK, however, the distances to each molecular cloud region must be taken into account for accurate comparison as this affects the physical scales seen by the telescope. For example, assuming a fixed size of 7020 au (0.03 pc) for the cores in Taurus and Perseus the angular source size, $\theta_{\rm src}$, in Taurus will be 52 arcsec while in Perseus, whose distances range from 283 to 325 pc (Table 1), $\theta_{\rm src}$ can range from \sim 25 – 22 arcsec. To account for this, we consider the filling factor, f, which measures the coupling between the source integrated intensity emission, $I(\theta, \phi)$, and the telescope beam, $P_n(\theta)$. By assuming $I(\theta, \phi)$ on the sky can be approximated by a Gaussian with FWHM $\theta_{\rm src}$, then the filling factor is given by,

$$f = \frac{\int I(\theta, \phi) P_n(\theta) d\Omega}{I(\theta = 0) \int P_n(\theta) d\Omega} = \frac{\theta_{\text{src}}^2}{\theta_{\text{src}}^2 + \theta_{\text{beam}}^2}.$$
 (1)

Given that the beam size, $\theta_{\rm beam}$, of the ARO 12 m is 63 arcsec at the CH₃CHO frequencies, we calculate a range of f values and scale $\theta_{\rm src}$ from the distance of Taurus to the range of observed distances in Perseus (e.g. at the Taurus distance a 7020 au sized core has

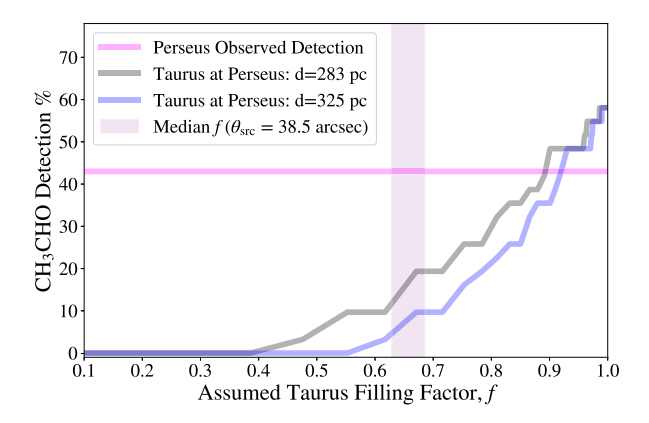


Figure 4. Expected detection percentages versus assumed filling factor, f, if the Taurus sample of CH₃CHO-detected cores from Scibelli & Shirley (2020) were put at Perseus distances. For reference, we also plot as a horizontal line (in magenta) the true observed detection percentage, 43 per cent, for the Perseus sample at the $\sigma_{T_{\rm mb}} = 5-8$ mk RMS limit. If the Taurus cores are similar in size as the Perseus cores, i.e. $\theta_{\rm src} = 38.5$ arcsec plotted at the range of distances as the vertical band (light pink), one would have only expected a $\sim 10-20$ per cent detection rate.

f=0.4 but in Perseus $f\sim0.1$). Given our new constraints, we re-calculate the RMS level and detection percentages, assuming at least a 3σ detection, from the Scibelli & Shirley (2020) Taurus survey. In Fig. 4 we show how the detection percentage drops with decreasing f and increasing distance. If the Taurus cores have similar physical source sizes as calculated for the Perseus cores (at 38.5 arcsec this is $\sim10\,900-12\,500$ au; see Section 4.4), the expected CH₃CHO detection rates at Perseus distances in Taurus are expected to be $\sim10-20$ per cent, which is $\sim2-4\times$ lower than what has been observed in the Perseus sample. Thus, considering CH₃OH and CH₃CHO are the precursors to higher complexity COMs, the starless and pre-stellar cores in the Perseus molecular cloud are just as prevalent in COMs, if not more so, than the Taurus molecular cloud.

4.2 Detection statistics: Yebes 40 m

The 15 cores with CH₃CHO detections (as well as CH₃OH detections) at the $\sigma_{T_{\rm mb}}=6\,{\rm mK}$ limit with the ARO 12 were observed with the Yebes 40 m. Within the 31.5 – 50 GHz range of the data, we searched for energetically favourable COM transitions (listed in Table 2) and claim a detection if both the Gaussian fitted peak was at least $3\times$ brighter than the noise, i.e. $>3\sigma$, and the Gaussian fitted integrated intensity, or area under the line, was $3\times$ brighter than the associated error. While not the focus of this paper, all line-of-sight velocities ($v_{\rm lsr}$) and line-widths (FWHM) are reported for each detected line in Table B2 in Appendix B. The $v_{\rm lsr}$ ranges from $\sim 6-10\,{\rm km\,s^{-1}}$ depending on the source and FWHM values typically range from $\sim 0.4-2\,{\rm km\,s^{-1}}$.

There were two additional transitions of the CH₃OH molecule and six additional transitions of the CH₃CHO molecule (see Table 2) that were observed in each core. In the case of core 264 the $1_{-0,1}-0_{-0,0}\,\mathrm{E}$ state transition of CH₃OH was not detected above a 3σ limit and for core 715 the $2_{1,2}-2_{1,1}\,\mathrm{E}$ transition of CH₃CHO was not detected above the 3σ limit (see in Appendix B Figs B1, B2, and B3).

In the search for new molecules, we find for the smaller (5-atom) COMs a detection rate of 9/15 (60 per cent) for t-HCOOH (Fig. 5) and 14/15 (93 per cent) for H₂CCO (Fig. 6). For the 6-atom N-bearing molecule CH₃CN in 12/15 (80 per cent) of the cores at

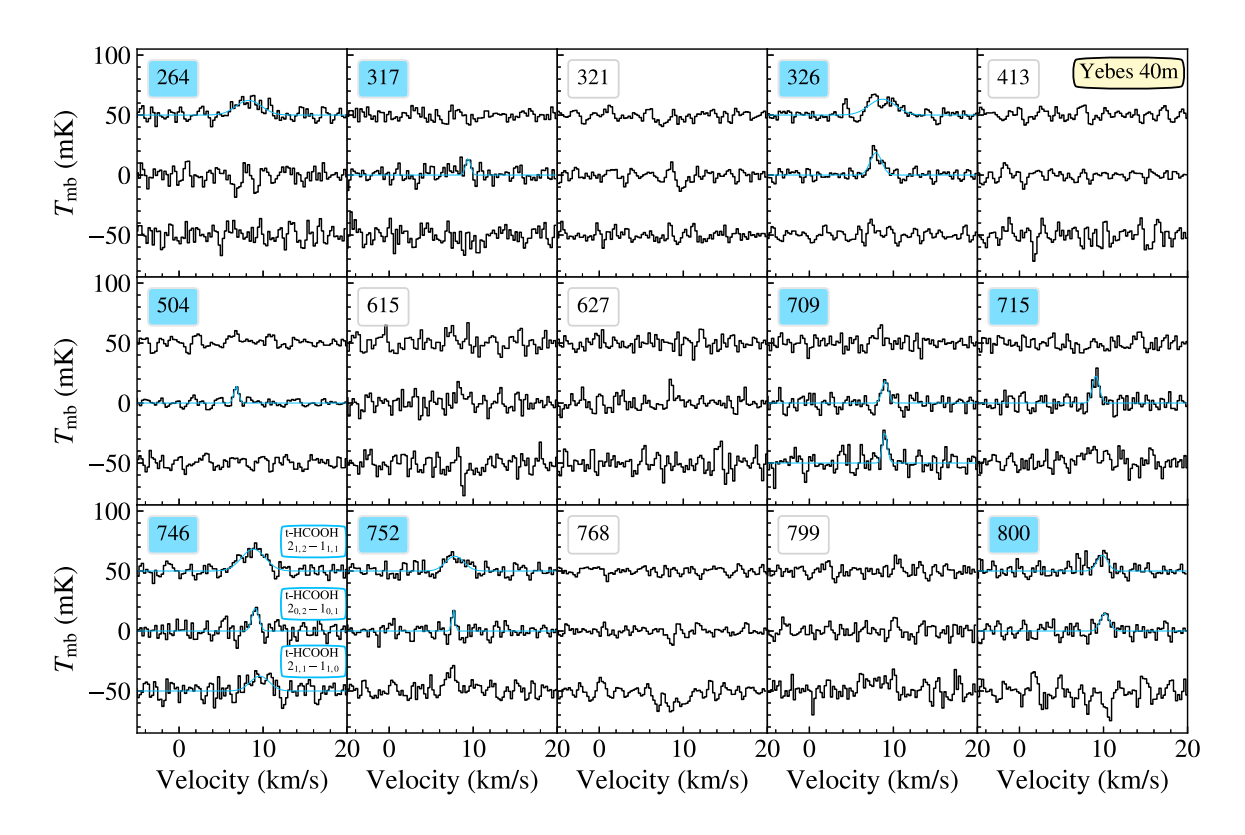


Figure 5. Formic acid, t-HCOOH, spectrum (in black) in units of $T_{\rm mb}$ (K) versus velocity (km s⁻¹) from the Yebes 40 m for the 15 core sub-sample. Gaussian fits are overplotted (in blue). There are three 2 – 1 transition observable and they are centred on the $v_{\rm lsr}$ of the core. Spectra are offset by intervals of 50 mK.

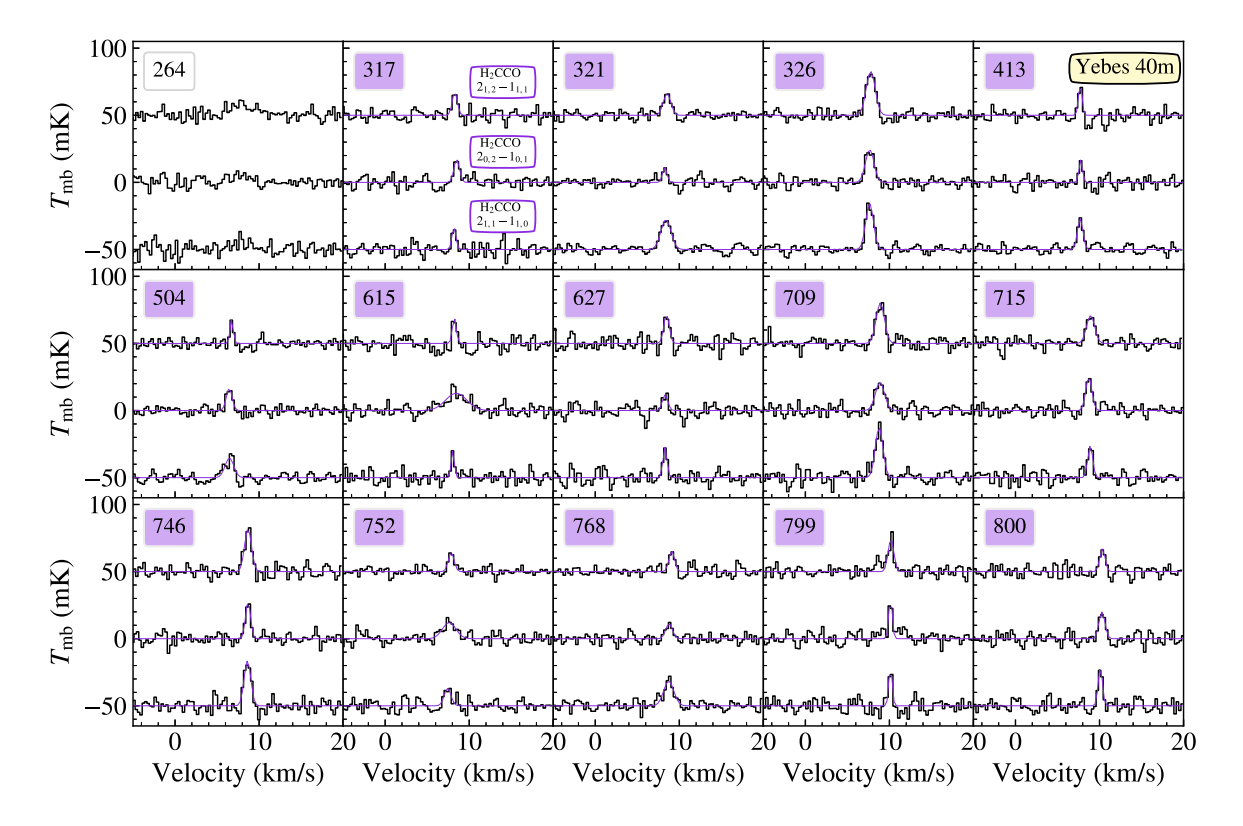


Figure 6. Ketene, H_2CCO , spectrum (in black) in units of T_{mb} (K) versus velocity (km s⁻¹) from the Yebes 40 m for the 15 core sub-sample. Gaussian fits are overplotted (in purple). There are three separate 2 - 1 transitions observable, and all transitions are centred on the v_{lsr} of the core. Spectra are offset by intervals of 50 mK.

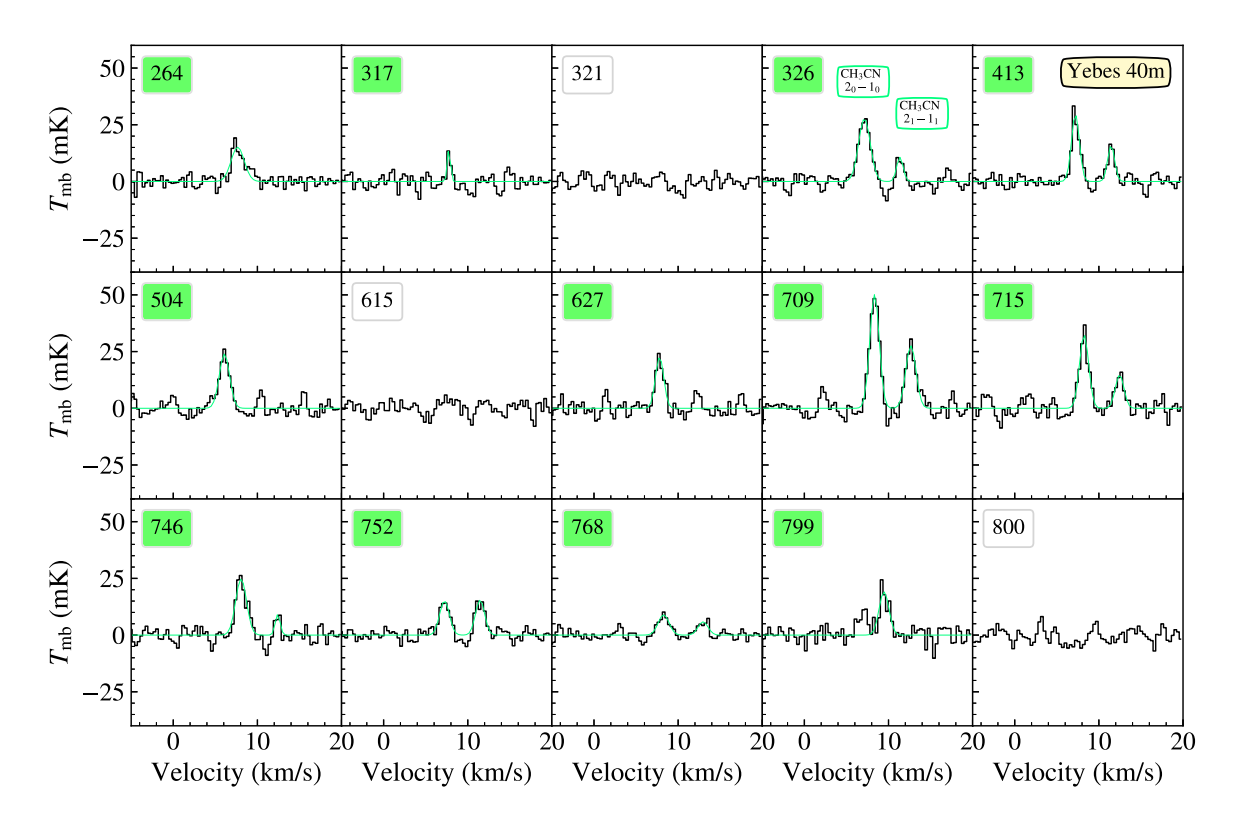


Figure 7. Methyl Cyanide, CH₃CN, spectrum (in black) in units of $T_{\rm mb}$ (K) versus velocity (km s⁻¹) from the Yebes 40 m for the 15 core sub-sample. Gaussian fits are overplotted (in light green). There are two 2 - 1 transitions that can be observable, and the $2_0 - 1_0$ state transitions is centred on the $v_{\rm lsr}$ of the core.

least the brightest $2_0 - 1_0$ transitions was detected and in 7/12 of these cores the nearby $2_1 - 1_1$ transitions was also detected (Fig. 7).

The 7-atom N-bearing molecule CH₂CHCN, while not seen in the ARO 12 m survey, was detected in < 34 per cent of the 15 core sub-sample with the Yebes 40 m data (Fig. 8). We report the most robust detection, with more than one transition detected above 3σ , for one core only, 413. For the remaining 4 cores (264, 709, and 746) with CH₂CHCN detected, only one transition is observed at > 3σ . Beyond the three CH₂CHCN transitions detected (listed in Table 2), other energetically favourable a-type transitions were searched for (listed in Table B1), and no significant detections were made.

Next, we searched for and detected the 8-atom molecule HCOOCH₃ in < 34 per cent of the cores. Multiple transitions are observed for cores 264, 321, 326, and 715, yet in core 768 only one transition was detected at > 3σ (Fig. 9). In core 326 the highest number of transitions were detected (4 total), followed by core 264 (3 total). Only one transition is detected for 768, the $4_{1,4} - 3_{1,3}$ E line, but it is also seen in cores 264 and 321.

Lastly, for the 9-atom molecule CH_3OCH_3 we find significant detections in < 27 per cent of the cores (Fig. 10). Confident detections are made for cores 264, 321, and 326 (20 per cent) as they show all three nearby $3_{1,2}-3_{0,2}$ AE+EA, EE, and AA state transitions, and for core 326 the additional three $4_{1,3}-4_{0,4}$ transitions. For core 627, only the brighter $3_{1,2}-3_{0,2}$ EE transition is seen above 3σ .

While each molecule searched for was detected in at least a handful of cores, in no single core are all of the COMs targeted detected. Core 326 has the most detections, with CH₃OH, CH₃CHO, t-HCOOH, H₂CCO, CH₃CN, HCOOCH₃, and CH₃OCH₃ all detected, and CH₂CHCN being the only non-detection. Interestingly, in core 264 the smaller 5-atom COM H₂CCO is not detected in our survey limit, yet it is the only core for which the species CH₂CHCN, HCOOCH₃,

and CH_3OCH_3 are all detected. Both of these cores are located in the active and shocked NGC1333 region (see Fig. 1), and below we discuss the COM detections in context of the location within the Perseus cloud.

4.3 Detection statistics: trends in spatial distribution

Overall, from this survey the detection statistics for COMs in starless and pre-stellar cores has at least doubled. The cores with COM detections reside in the two active Perseus clusters, NGC 1333 and IC 348, now thought to be of similar age (Luhman, Esplin & Loutrel 2016). NGC 1333 in particular is known to host many protostars and active outflows (Knee & Sandell 2000; Plunkett et al. 2013), which could help to get COMs off the grains in the cold starless and pre-stellar cores we've targeted in this survey. It is in the NGC 1333 region where the majority of the protostars from the PEACHES survey reside with detections of at least CH₃OH (Yang et al. 2021; see Fig. 1). In particular, cores 264, 317, 321, and 326 are all located within ~8 arcmin box that also contains 10 protostars; Per-emb 18, Per-emb 21, Per-emb 44, Per-emb 27, Per-emb 35 A & B, Per-emb 13, Per-emb 12 A & B, and SVS 13A2. It is in core 326 where we detect all of the O-bearing COMs larger than CH₃OH. Core 326 is not only the densest core ($n(H_2) = 2.87 \times 10^5 \text{ cm}^{-3}$; Table 1), but it is also ~ a few beams away from protostars Per-emb 44, Per-emb 12 A & B, and Per-emb 13 which have warm gas-phase detections of CH₃CN, CH₃OH, CH₃CHO, HCOOCH₃, and CH₃OCH₃ (Yang et al. 2021).

Towards the IC 348 cluster, which exhibits a lower abundance of objects at lower masses than NGC 1333 (Luhman et al. 2016), studies have been done to detect large complex molecules such as fullerenes, PAHs, and numerous hydrocarbon species (i.e. HCN,

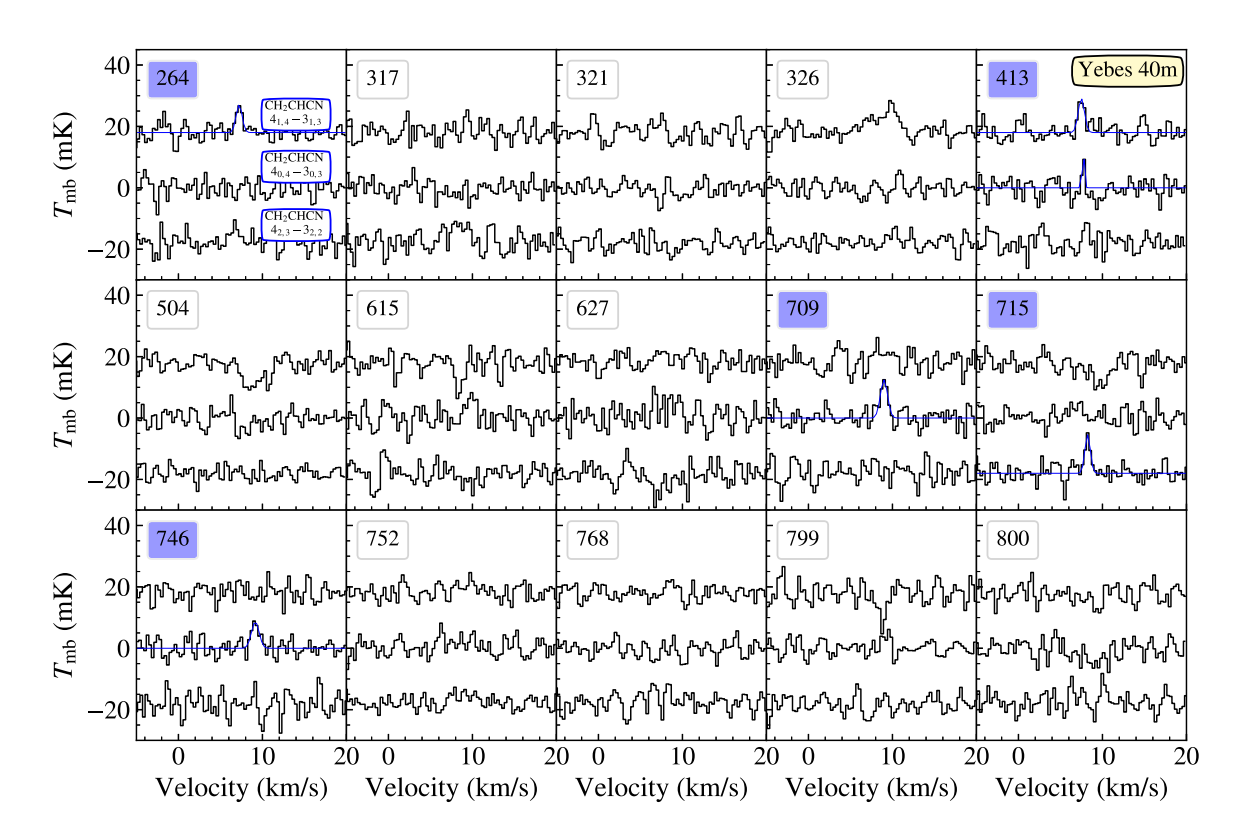


Figure 8. Vinyl cyanide, CH₂CHCN, spectrum (in black) in units of $T_{\rm mb}$ (K) versus velocity (km s⁻¹) from the Yebes 40 m for the 15 core sub-sample. Gaussian fits are overplotted (in blue). There are three separate 4 – 3 transitions that could be observable, and all transitions are centred on the $v_{\rm lsr}$ of the core. Spectra are offset by intervals of 18 mK for easier viewing.

C₂H₂, C₄H₂, HC₃N, HC₅N, C₂H₆, C₆H₂, C₆H₆) using mid-IR spectra from *Spitzer* (Iglesias-Groth 2019; Iglesias-Groth & Marin-Dobrincic 2023). Interestingly, only three nearby protostars in this region from the PEACHES sample had at least CH₃OH detected, i.e. Per-emb 11 A, C, and Per-emb 1 (Yang et al. 2021). In close proximity to these protostars (< 5 arcmin) are the starless and prestellar cores 709 and 715 from this survey each with CH₃CHO detections, additional bright CH₃CN lines (see Fig. 7), as well as detections of CH₂CHCN, t-HCOOH, H₂CCO, and (for core 715 only) HCOOCH₃.

As for the other regions in Perseus, the star formation activity and evolutionary state (i.e. presence or absence of protostars) also seem to correlate with the presence of COMs in the starless and pre-stellar stage, though we note that the number of cores sampled in the regions outside the two main clusters (NGC 1333 and IC 348) is lower (see Fig. 1 and Table 1). It is in the B5 region where a dominant embedded protostar, B5-IRS1, with three gravitationally bound dense-gas fragments resides (Pineda et al. 2015), and hosts the CH₃CHO-abundant cores 799 and 800 (see Fig. 1). Core 800, in fact, is spatially coincident with the 'B5-Cond1' gas fragment as described in Pineda et al. (2015). In contrast, in L1455 there is a low abundance of Class 0 protostars (Hatchell, Fuller & Richer 2007), and no starless or pre-stellar cores from our sample with CH₃CHO detections at our $\sigma_{T_{\rm mb}} = 6$ mK limit (Fig. 1). Only one protostar from the PEACHES sample had at least CH₃OH detected in the L1455 region. Per-emb 20, and for this source no higher complexity COMs were detected (i.e. no t-HCOOH, CH₃CN, CH₃CHO, HCOOCH₃, or CH₃OCH₃). Lastly, we note that compared to the cores within NGC 1333 and IC 348 (a total of 20), the cores in these other regions (a total of 15) on average have lower dust and kinetic temperatures

(e.g. median $T_{\rm k}$ differences of 12.1 and 10.5, respectively). Thus, regions within the Perseus molecular cloud with increased COM detections in the warm protostellar stage also exhibit an increased COM detection in the cold pre-stellar stage.

4.4 Column densities

Depending on the molecule, and how many available transitions were observed and detected for that molecule, four different methods were used to calculate column densities; the RADEX code method (van der Tak et al. 2007), the rotation diagram (RD) method, the constant excitation (or CTEX) method, and the local thermodynamical equilibrium (LTE) method. RADEX is the only non-LTE method that, while 1D, is able to calculate an excitation temperature, $T_{\rm ex}$, a column density, N, and an opacity, τ , for each transition separately. This method is limited, however, to the few molecules with which collisional rate coefficients have been calculated, which in our case are CH₃OH, CH₃CN, and HCOOCH₃.

For CH₃OH we are able to utilize the difference in beam sizes of the ARO 12 m and Yebes 40 m CH₃OH transitions (62 arcsec and 37 arcsec, respectively; see Table 2) in order to constrain the source size, $\theta_{\rm src}$, and account for the true filling factor, f, when calculating the column density for our 15 core sub-sample (see Appendix C for more detail). We find $\theta_{\rm src}$ ranges from 26.5 – 56.5 arcsec where the median $\theta_{\rm src}$ is 38.5 arcsec (5 arcsec median deviation; Fig. 11), which was then used as the 'typical' value when calculating $N({\rm CH_3OH})$ for the remaining cores with no Yebes 40 m data. These source sizes are utilized in the column density calculations for CH₃CHO, as this molecule is believed to trace CH₃OH spatially (Vasyunin et al. 2017;

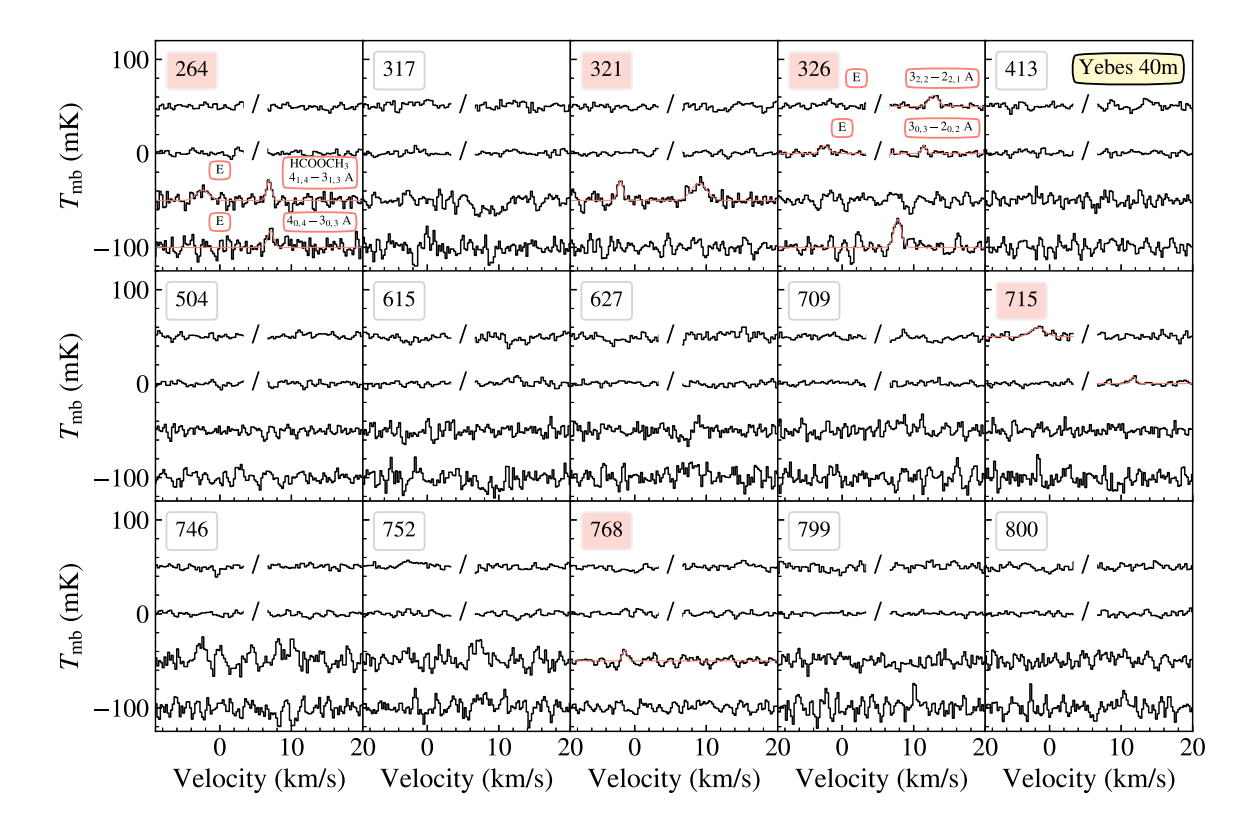


Figure 9. Methyl Formate, HCOOCH₃, spectrum (in black) in units of $T_{\rm mb}$ (K) versus velocity (km s⁻¹) from the Yebes 40 m for the 15 core sub-sample. Gaussian fits are overplotted (in orange). Spectra are offset by intervals of 50 mK. The top two rows show the 3-2 E & A states, respectively, which are not visible together within the plotted frequency range (denoted by the '/') and instead the E line is shifted by–10 km s⁻¹ and the A line by + 5 km s⁻¹ from the $v_{\rm lsr}$ of the core.

Scibelli et al. 2021), but for the remaining molecules the source size is unknown so f = 1 is assumed.

The total CH₃OH column densities (A + E states) calculated from RADEX, $N_{\rm sum}$, range from $0.87-50.27\times10^{13}$ cm⁻², the excitation temperatures range from $T_{\rm ex}\sim5-13$ K, and the optical depths are generally consistent with optically thin emission, yet for several cores the $2_{0.2}-1_{0.1}$ A transition gets close to $\tau\sim1$ (Table C1 in Appendix C). These $N_{\rm sum}$ values are roughly a factor $2-8\times$ higher than for the Taurus sample, which ranged from $0.42-3.4\times10^{13}$ cm⁻² (Scibelli & Shirley 2020), however no filling factor was applied to the Taurus sample and could contribute to this offset in $N_{\rm sum}$. If we assume the median emitted source size for the Perseus sample is similar to the Taurus sample and scale this to the appropriate distance, the N (CH₃OH) values in Scibelli & Shirley (2020) increase by factors of 1.6-1.8. Thus, the CH₃OH column densities in Perseus are in fact elevated compared to Taurus.

The RADEX derived column densities for CH₃CN range between $0.81-5.8\times10^{11}\,\mathrm{cm^{-2}}$ and the excitation temperatures range from $5.57-13.2\,\mathrm{K}$, with a median value of $7.39\,\mathrm{K}$, where the τ calculated is consistent with optically thin with $\tau_{\mathrm{max}}<0.009$. Towards the dust peak of core L1517B a CH₃CN column density value is found within this range, at $2.1\pm0.6\times10^{11}\,\mathrm{cm^2}$ (Megías et al. 2023). For HCOOCH₃, the average N (and standard deviation) value of the detected transitions is $2.97\pm2.18\times10^{12}\,\mathrm{cm^{-2}}$, where T_{ex} ranges from $10.5-16.5\,\mathrm{K}$ and for all cases $\tau_{\mathrm{max}}<0.003$ is also consistent with optically thin emission.

For the remaining molecules, the other three methods (RD, CTEX, or LTE) are used, which assume a fixed $T_{\rm ex}$ for all transitions. The upper state column density (assuming optically thin, $\tau_{\nu} \ll 1$,

emission) can then be calculated where,

$$N_{u} = \frac{I}{hA_{ul}f} \frac{u_{v}(T_{\text{ex}})}{[J_{v}(T_{\text{ex}}) - J_{v}(T_{\text{cmb}})]},$$
(2)

and h is the Planck constant, f is the (frequency dependent) filling factor (equation 1), I is the integrated intensity of the line, A_{ul} is the spontaneous emission coefficient (or 'Einstein A'), $T_{\rm cmb}$ is the background temperature of 2.73 K, and u_{ν} (Planck energy density) and J_{ν} (Planck function in temperature units) are defined as,

$$u_{\nu} \equiv \frac{8\pi h \nu^3}{c^3} \frac{1}{\exp(h\nu/kT - 1)},$$
 (3)

$$J_{\nu} \equiv \frac{h\nu}{k} \frac{1}{\exp\left(h\nu/kT - 1\right)}.\tag{4}$$

In these equations, c is the speed of light, k is the Boltzmann constant, and ν is our line frequency. For a total column density, N_{tot} ,

$$\frac{N_u}{g_u} = \frac{N_{\text{tot}}}{Q(T_{\text{ex}})} \exp\left(-E_u/kT_{\text{ex}}\right),\tag{5}$$

where g_u is the upper state degeneracy, E_u is the upper state energy, and $Q(T_{\rm ex})$ is the partition function dependent on the excitation temperature of the molecule.

In a standard RD method, the log normal of the left side of equation (5), $\ln(N_u/g_u)$, is plotted versus E_u so that the excitation temperature, $T_{\rm ex}$, is the inverse of the slope of the linear fit and the y-intercept is used to find $N_{\rm tot}$ (Goldsmith & Langer 1999). This method is used to calculate the column density for the A state of CH₃CHO (Fig. 12), with more than three transitions ranging from $E_u/k \sim 3-14$ K for cores with both ARO 12 m and Yebes 40 m observations. The $T_{\rm ex}$ calculated from our RD method range from 4.27-7.07 with

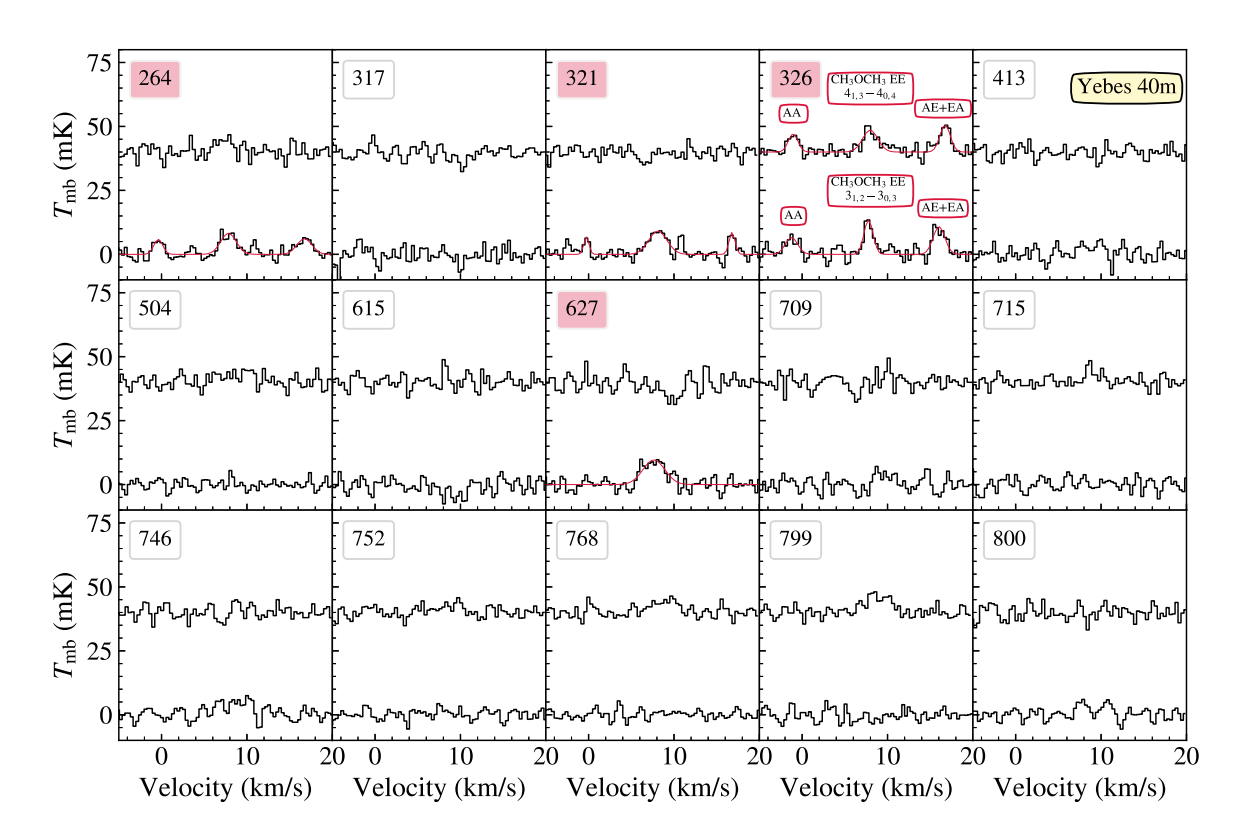


Figure 10. Dimethyl ether, CH₃OCH₃, spectrum (in black) in units of $T_{\rm mb}$ (K) versus velocity (km s⁻¹) from the Yebes 40 m for the 15 core sub-sample. Gaussian fits are overplotted (in red). The EE transitions are centred on the $v_{\rm lsr}$ of the core. The 4 – 4 lines are offset by 40 mK for easier viewing.

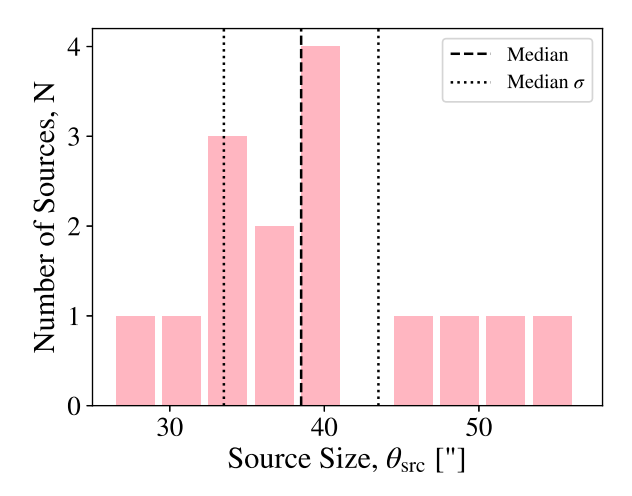


Figure 11. The distribution of source size, $\theta_{\rm src}$, for the Yebes 40 m sub-sample of cores constrained from RADEX calculations for CH₃OH transitions observed at two different beam sizes, $\theta_{\rm beam}$.

a median value of 5.55 K and median standard deviation of 0.9 K. This median value of 5.55 K is then used to calculate the N of CH₃CHO A for the remaining cores. The full sample ranges from 0.59 - 8.08 \times 10¹² cm⁻² with a median value (and median standard deviation) of 2.10 \pm 0.61 \times 10¹² cm⁻².

Calculated with the same set of equations, the CTEX method also uses at least two transitions with different E_u values to simultaneously constrain $T_{\rm ex}$ as well as the column density [see details in Appendix of Caselli et al. (2002) and equation (80) of

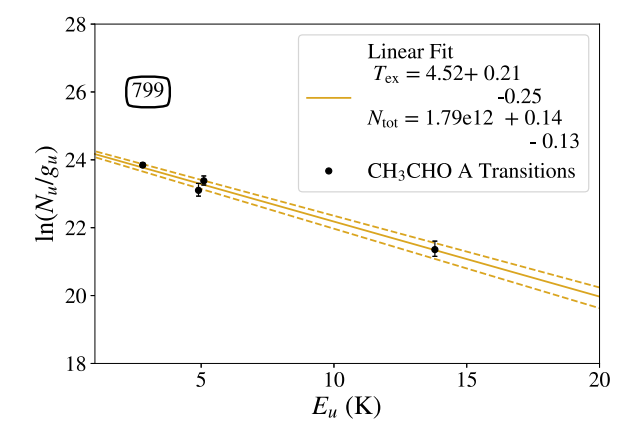


Figure 12. The rotation diagram method is used to constrain the column densities, N, and excitation temperatures, $T_{\rm ex}$, for each of the 15 cores with multiple A-state CH₃CHO transitions. Here we show the fit for core 799.

Mangum & Shirley (2015)], but instead finds the intersection of the plotted N versus $T_{\rm ex}$ curves (e.g. Ambrose, Shirley & Scibelli 2021; Scibelli et al. 2021; Galloway-Sprietsma et al. 2022). In our sample, for core 326 there are two bright CH₃OCH₃ EE transitions, $3_{1,2} - 3_{0,3}$ and $4_{1,3} - 4_{0,4}$, with a large enough E_u gap, at 7 K and 11 K, respectively, that the CTEX method can constrain N and $T_{\rm ex}$. We find for a $T_{\rm ex} = 11.4 \pm 5.1$ K the column density is constrained to $N({\rm CH_3OCH_3}) = 4.32 \pm 0.57 \times 10^{12}$ cm⁻² (see Fig. 13).

Lastly, for the LTE method, rather than calculating a single $T_{\rm ex}$, one needs to be assumed in order to calculate $N_{\rm tot}$. For the remaining molecules, H₂CCO, t-HCOOH, and CH₂CHCN, we use

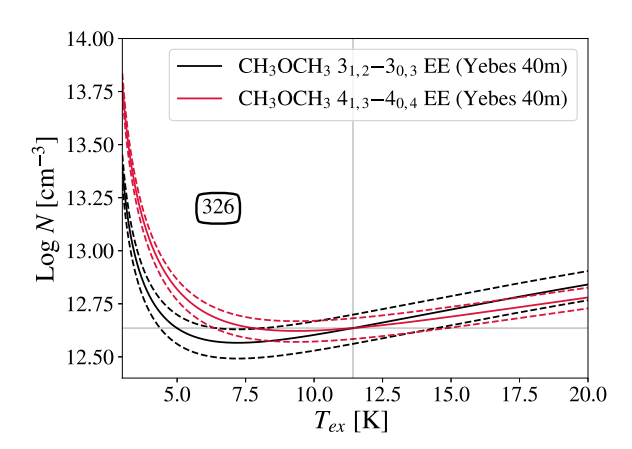


Figure 13. In the CTEX radiative transfer method column density, N, in log-scale is plotted against the excitation temperature $T_{\rm ex}$ for two transitions of CH₃OCH₃ EE, as overlapping sold curves (errors as dashed lines), that were detected towards core 326. The dashed lines show the spread in error from the intensity measurements and are used to calculate the spread in error for N and $T_{\rm ex}$. The horizontal and vertical lines show where the two transitions cross to find the best constraint.

this LTE method. We calculate for a $T_{\rm ex}$ of 10 K, $N({\rm o-H_2CCO})$ ranging from $1.8-7.6\times 10^{12}\,{\rm cm^{-2}}$ and $N({\rm p-H_2CCO})$ ranging from $0.8-4.4\times 10^{12}\,{\rm cm^{-2}}$. In the case of t-HCOOH assuming $T_{\rm ex}$ of $10\,{\rm K}$, the N values range from $1.5-15\times 10^{12}\,{\rm cm^{-2}}$. For the N-bearing species CH₂CHCN we assume the $T_{\rm ex}$ is comparable to those found in the RADEX calculations for CH₃CN to estimate N, calculating values ranging from $0.18-0.72\times 10^{12}\,{\rm cm^{-2}}$. More detail on the exact analysis methods on a molecule-by-molecule and core-by-core basis, along with all listed column density values, can be found in Appendix C.

5 DISCUSSION

The abundances of COMs in the starless and pre-stellar cores in Perseus provide key insights into formation histories at the earliest phases of low-mass star formation, where initial chemical conditions are set. Here we calculate and compare across our samples the COM abundances with respect to molecular hydrogen (H2), calculated from the Herschel column density values listed in column 8 of Table 1 and the COM column densities, N, from Section 4.4, including 3σ upper limits. In the case of the asymmetric rotors the N derived from a single state is doubled (e.g. A + E) to find N_{sum} , which assumes a 1:1 ratio (or 1:2:1 in the case of CH₃OCH₃) that may not always be the case. We do find the mean A:E ratio for CH₃OH across all cores (using the brightest 96 GHz transitions) is 1.1 and conclude doubling the A state column density is a reasonable approximation to make. For H₂CCO, a total N is found first by adding both para and ortho states (Table C3). In Fig. 14 we plot both N and abundance with respect to H₂ values across the full 35-core sample, for which we have measured constraints for CH₃OH, CH₃CHO, and CH₂CHCN.

In Fig. 15 a similar plot is shown for the Yebes 40 m sub-sample of 15 cores for which we have measured constraints for H_2CCO , t-HCOOH, CH_3CN , $HCOOCH_3$, and CH_3OCH_3 . Noticeable is the higher abundance of CH_3OH compared to all other molecules targeted (ranging from 1.12 to 12.9×10^{-9}), and the lower abundances of the N-bearing species CH_3CN and CH_2CHCN , which are well correlated (i.e. increased CH_3CN leads to CH_2CHCN) with values \sim a few $\times 10^{-11}$ (see also Table 3). Specifically, we find for the

cores with detections that the abundance of CH₂CHCN ranges from $1.10-5.03\times 10^{-11}$ and that the abundance of CH₃CN ranges from $0.38-4.34\times 10^{-11}$. For the remaining O-bearing COMs abundances range from $\sim 10^{-10}-10^{-9}$, i.e. detected molecular abundances $X(\text{CH}_3\text{CHO})$ from $0.99-6.27\times 10^{-10}$, X(t-HCOOH) from $0.71-7.34\times 10^{-10}$, $X(\text{H}_2\text{CCO})$ from $2.01-11.3\times 10^{-10}$, $X(\text{HCOOCH}_3)$ from $1.25-4.00\times 10^{-10}$, and $X(\text{CH}_3\text{OCH}_3)$ from $1.10-16.0\times 10^{-10}$ (Table 3). In the subsequent subsections, we perform detailed comparisons of these abundances and discuss implications for COM formation in cold cores.

5.1 Abundance correlations

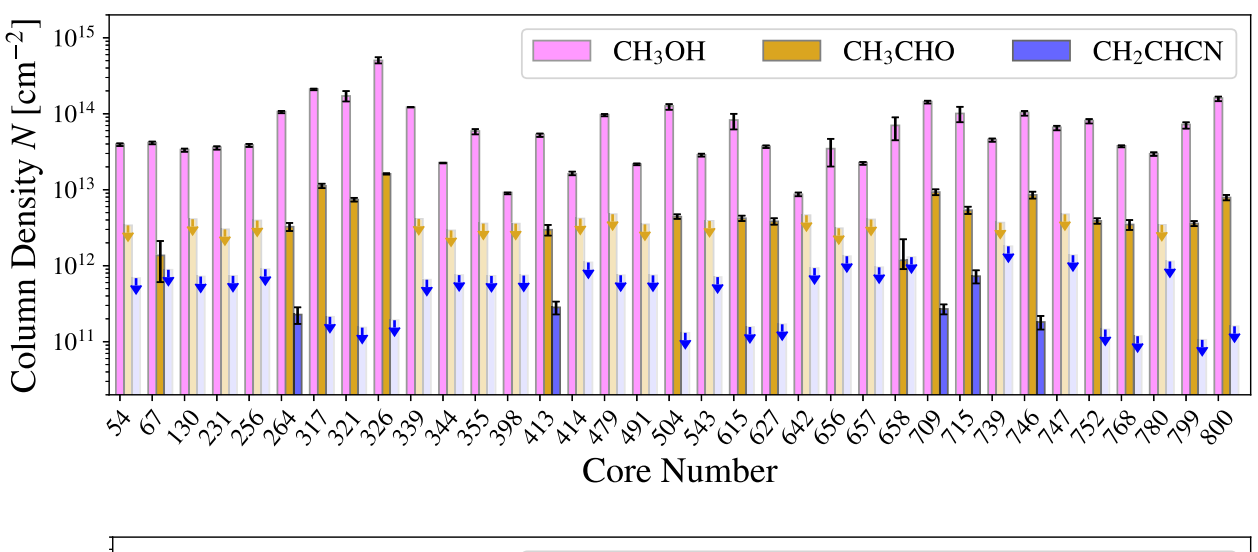
We first explore how the abundances of each of the eight species of COMs focused on in this survey correlate with each other (Fig. 16). To quantitatively compare the relationship, we calculate the Spearman rank correlation coefficient 'r' which measures the uniformity of the relationship between two data sets (part of the 'SCIPY.STATS' package: Virtanen et al. (2020)). A value of -1 or +1 imply an exact negative or positive monotonic relationship, respectively, and a value of 0 implies no correlation. Strong positive trends are typically expected for molecules that are chemically related or for molecules that depend on similar physical conditions, such as temperature.

First, we find a positive trend (r = 0.56, considering only the detections) when CH₃CHO is compared to CH₃OH. This positive trend is consistent with the correlation found for the sample of 31 cores in Taurus, where r = 0.54 (Scibelli & Shirley 2020). Additionally, the positive correlation we find for our full sample that considers the upper limits from the full Perseus sample (35 total cores) is compatible with this overall trend. These upper limits have limited constraints on CH₃CHO, thus deeper searches for CH₃CHO in these cores would likely cause the full trend to remain positively correlated.

Notably, there is not a significant positive correlation when the CH₃CN abundance is compared against CH₃OH (r = 0.10/0.23; for the full sample and detected sample, respectively). This is unlike what is seen during warm-phase chemistry from observations of CH₃CN and CH₃OH towards the neighbouring protostars in Perseus (Belloche et al. 2020; Yang et al. 2021). The PEACHES survey in particular find a tight correlation (r = 0.87) between CH₃CN and CH₃OH that spans more than two order of magnitude in column densities and suggest a possible chemical relation between these two species and a large chemical diversity among the protostars (Yang et al. 2021). Though, the CALYPSO survey cautioned that a strong correlation may not imply a chemical link (Belloche et al. 2020). Similar to the PEACHES sample, we do see a positive correlation with CH_3OCH_3 and $HCOOCH_3$ (r = 0.76/0.50) like they see for their sample of protostars. It should still be noted that the sample size of PEACHES is larger (factor of 3) when compared to our sub-sample of starless and pre-stellar cores in Perseus with CH₃CN, CH₃OCH₃, and HCOOCH₃ constraints.

Other species with correlated abundances (r values > 0.5 for both the full sample and detected sample; Fig. 16) include the N-bearing COMs CH₃CN and CH₂CHCN (r= 0.80/0.60), H₂CCO and CH₃CN (r= 0.64/0.69), as well as H₂CCO and CH₃CHO (r= 0.65/0.62). In Bergner et al. (2017) they also find positive correlations between CH₃CHO and CH₃OH (r= 0.9) and H₂CCO and CH₃CN (r= 0.99) from single-dish data for small samples of low-mass protostars (< 6), the majority of which are in Perseus.

Next, we compare COM abundances with respect to H_2 to the average H_2 volume density, $n(H_2)$, in units of cm⁻³ for our sample of



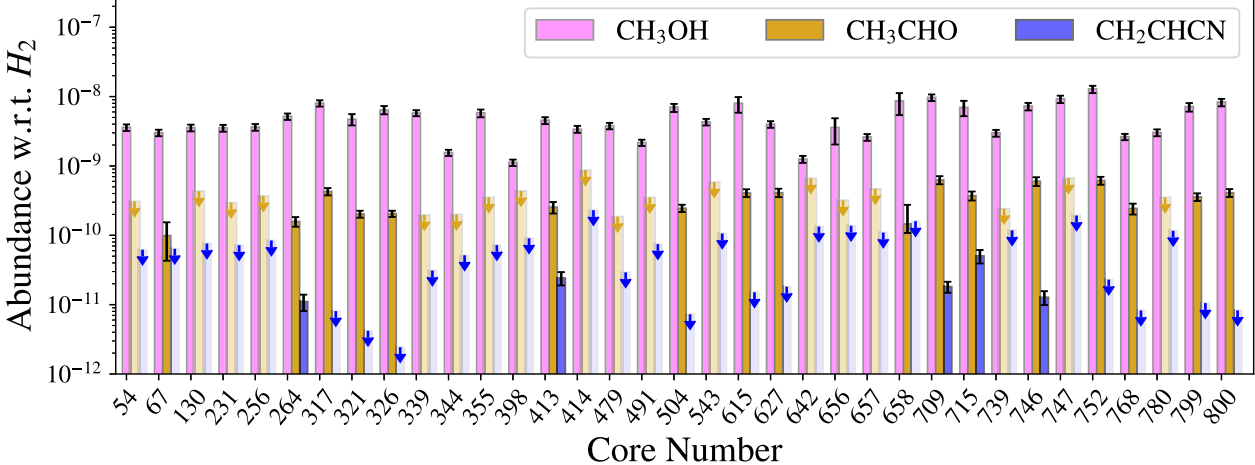


Figure 14. Comparison of COM column density values (top) and abundances (bottom) within the full 35 core ARO 12 m sample. Plotted from left to right for each core are values calculated for CH₃OH (magenta), CH₃CHO (gold), and CH₂CHCN (blue). Error bars are in black and upper limits are shown with downward arrows (and lighter shaded bars).

cores (Fig. 17). This $n(H_2)$ value comes from Table 1, column 9, and is the median value calculated from the *Herschel* maps, within the ARO 12 m 62 arcsec beam, where an error of 10 per cent is assumed. This is also the same beam size used to calculate the average H_2 volume density, $n(H_2)$, for the Taurus cores in Scibelli & Shirley (2020), though we stress that due to the difference in distances we are biased to lower $n(H_2)$ values on average for the Perseus sample.

There is significant scatter for CH₃OH, both in Perseus (r = 0.15) and for the sample of cores in Taurus cores (r = -0.13; Scibelli & Shirley 2020), suggesting that CH₃OH does not correlate with $n({\rm H}_2)$. As for CH₃CHO, a general negative correlation is found except when the densest core 326 is considered (r = -0.62/-0.29; for the full sample and detected sample, respectively) compared to no correlation found (r = 0.16) for the full sample of Taurus cores with CH₃CHO detections. Compared to Perseus, the majority of the Taurus cores lie within the same $4 \times 10^4 - 2 \times 10^5$ cm⁻³ range (see insert plot in top left panel of Fig. 17), though again we are biased to lower $n({\rm H}_2)$ values due to the further distance of Perseus. The abundances with respect to H₂, however, do differ with both CH₃OH and CH₃CHO abundances in Taurus averaging an order of magnitude

lower than those in Perseus, which could explain why similar trends in volume density are not seen. For the CH₃CHO abundances in Taurus specifically, the scatter is also due to the fact that a limited number (two or less) of molecular transitions were available to carry out the column density analysis, which also needed to assume a filling factor of one, f=1 [i.e. no source size was taken into account; see Scibelli & Shirley (2020)].

Looking at the other molecules, there does appear to be negative correlations for $n({\rm H_2})$ with the 5-atom species ${\rm H_2CCO}$ (r=-0.78/-0.75), t-HCOOH (r=-0.59/-0.57), the N-bearing species ${\rm CH_3CN}$ (r=-0.60/-0.60), ${\rm CH_2CHCN}$ (r=-0.68/-0.50), as well as ${\rm CH_3OCH_3}$ (r=-0.60/-1.0; note only four data points for the detected sample). As for HCOOCH₃, no significant correlation is found, but it trends in the negative direction as well (r=-0.47/-0.30; see Fig. 17).

The negative trend with respect to $n(H_2)$ confirms that COM abundances (excluding CH₃OH) decrease with increasing volume density towards the dust peak of the starless and pre-stellar cores in Perseus. It has been seen with spatially resolved maps of the very dense and highly evolved pre-stellar core L1544 that the smaller COMs H₂CCO and CH₃CN are peaking away from the dust peak of

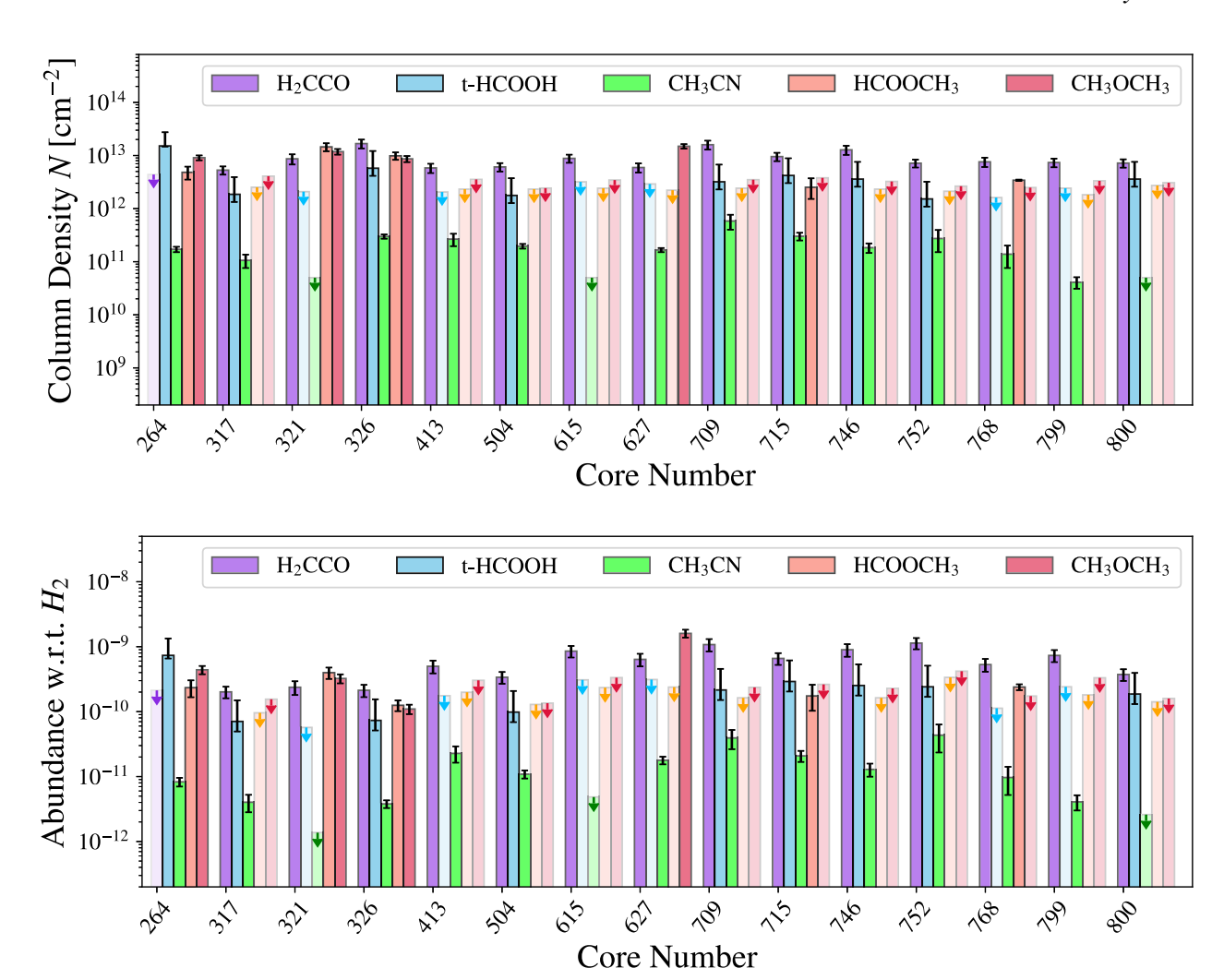


Figure 15. Comparison of COM abundances within the 15 core Yebes 40 m sub-sample. Plotted from left to right for each core are values calculated for H₂CCO (purple), t-HCOOH (blue), CH₃CN (lime), HCOOCH₃ (orange), and CH₃OCH₃ (red). Error bars are in black and upper limits are shown with downward arrows (and lighter shaded bars).

the core (Spezzano et al. 2017) and larger COMs have been found to be enhanced away of the dust peak towards the methanol peak (Jiménez-Serra et al. 2016). It is therefore also probable the COMs in our Perseus sample are also peaking away from the dust peak in the higher density cores. This effect is due to depletion effects where in the densest cores molecules will freeze-out onto the grains more efficiently and thus their COM abundances are expected to be lower. While CH₃OH is also known to be chemically differentiated spatially in evolved cores like L1544 (Bizzocchi et al. 2014) and 'typical' cores in Taurus' L1495 filament (Punanova et al. 2022), the abundance is likely high enough across larger spatial scales that we cannot differentiate the CH₃OH depletion towards the dust peak of the Perseus cores within our observed beam sizes. It could also be that unlike CH₃OH, known to form on grains (Charnley, Tielens & Millar 1992), the other COMs in the Perseus cores could be forming predominantly in the gas-phase (e.g. Balucani et al. 2015; Vazart et al. 2020; Giani et al. 2023) and are more likely to experience depletion at high densities (see Section 5.3 for more discussion on formation routes). Future work to better characterize the spatial distribution of COMs towards these Perseus cores is needed.

Outside of $n(H_2)$, we also explore how abundances with respect to H_2 correlate with kinetic temperature, T_k , and find no significant

correlations (r < 0.3). Additionally, 14 cores in our sample overlap with the magnetic field alignment catalogue reported in Pandhi et al. (2023), and therefore we explore possible correlations with COM abundance for the larger sample of cores with CH₃OH and CH₃CHO detections. We find no significant trend (r > -0.4) in CH₃OH abundance with velocity gradient or magnetic field alignment. For CH₃CHO, however, a negative correlation in the velocity gradient is found for the seven overlapping catalogue matched cores (r = -0.67), but no strong correlation is found for the magnetic field alignment (r = -0.30).

5.2 COM abundance across low-mass star formation

CH₃OH is a 'mother' molecule to COM formation that survives the disc formation process and is used to normalize other COM abundances in order to compare across the various stages of low-mass star formation, from cores to comets (e.g. Drozdovskaya et al. 2019; van Gelder et al. 2020; Scibelli et al. 2021; Yang et al. 2021). In Fig. 18, we plot the abundances of COMs with respect to CH₃OH for not only the sample of starless and prestellar cores in Perseus focused on in this study, but the abundance values for other cold

Table 3. COM abundances with respect to H₂ for starless and pre-stellar cores in Perseus.

Core # ¹ (Herschel)	$\begin{array}{c} \text{t-HCOOH} \\ \times 10^{-10} \end{array}$	H_2 CCO $\times 10^{-10}$	CH_3CN $\times 10^{-11}$	$CH_3OH \times 10^{-9}$	$CH_3CHO \times 10^{-10}$	$CH_2CHCN \times 10^{-11}$	$HCOOCH_3 \times 10^{-10}$	$CH_3OCH_3 \times 10^{-10}$
54	_	_	_	$3.59^{+0.41}_{-0.37}$	< 3.07	< 6.21	_	_
67	_	_	_	$3.01^{+0.34}_{-0.32}$	$0.99^{+0.56}_{-0.55}$	< 6.39	_	_
130	_	_	_	$3.56_{-0.38}^{+0.42}$	< 4.33	< 7.62	_	_
231	_	_	_	$3.54_{-0.37}^{+0.43}$	< 2.95	< 7.20	_	_
256	_	_	_	$3.63^{+0.41}_{-0.39}$	< 3.69	< 8.43	_	_
264	$7.34^{+0.76}_{-6.02}$	< 2.12	$0.83^{+0.13}_{-0.70}$	$5.17^{+0.57}_{-0.53}$	$1.58^{+0.25}_{-0.25}$	$1.10^{+0.29}_{-0.29}$	$2.34^{+0.67}_{-0.64}$	$4.40^{+0.64}_{-0.64}$
317	$0.71^{+0.21}_{-0.79}$	$2.01^{+0.41}_{-0.41}$	$0.40^{+0.12}_{-0.00}$	$8.02^{+0.85}_{-0.81}$	$4.28^{+0.52}_{-0.51}$	< 0.81	< 0.96	< 1.55
321	< 0.57	$2.37^{+0.57}_{-0.57}$	< 0.14	$4.69_{-0.89}^{+0.86}$	$2.03^{+0.23}_{-0.23}$	< 0.42	$3.98^{+0.79}_{-0.51}$	$3.24^{+0.51}_{-0.51}$
326	$0.73^{+0.22}_{-0.82}$	$2.13^{+0.46}_{-0.46}$	$0.38^{+0.05}_{-0.24}$	$6.38^{+0.84}_{-0.91}$	$2.05^{+0.21}_{-0.21}$	< 0.24	$1.25^{+0.23}_{-0.18}$	$1.10^{+0.18}_{-0.18}$
339	-0.82	-0.46	-0.24	$5.78^{+0.58}_{-0.58}$	< 1.96	< 3.11	-0.18	-0.18
344	_	_	_	$1.55^{+0.16}_{-0.16}$	< 1.99	< 5.15	_	_
355	_	_	_	$5.83^{+0.81}_{-0.68}$	< 3.53	< 7.22	_	_
398			_	$1.12^{+0.13}_{-0.11}$	< 4.36	< 9.05		_
413	< 1.76	$4.99^{+1.11}_{-1.11}$	$2.28^{+0.64}_{-0.00}$	$4.55^{+0.55}_{-0.48}$	$2.54^{+0.48}_{-0.48}$	$2.42^{+0.52}_{-0.52}$	< 1.98	< 3.03
414	< 1.70	4.99_1.11	2.20_0.00	$3.38^{+0.37}_{-0.41}$	< 8.70	< 23.0	< 1.56	< 5.05
479	_	_	_	$3.79^{+0.42}_{-0.39}$	< 1.86	< 2.92	_	_
491	_	_	_	$2.17^{+0.23}_{-0.22}$	< 3.50	< 7.46	_	_
504	0.08+0.29	- 2 20+0.70	$1.09^{+0.16}_{-0.00}$	$\frac{2.17}{-0.22}$		< 0.73	< 1.29	< 1.35
543	$0.98^{+0.29}_{-1.10}$	$3.38^{+0.70}_{-0.70}$	$1.09_{-0.00}$	$7.04^{+1.04}_{-0.81}$	$2.45^{+0.29}_{-0.31}$ < 5.83	< 10.6	< 1.29	< 1.55
	2.00	0.54+1.72	- 0.40	$4.31^{+0.48}_{-0.46}$			2.24	- 2.22
615	< 3.08	$8.54^{+1.72}_{-1.72}$	< 0.48	$8.00^{+2.14}_{-1.83}$	$4.07^{+0.52}_{-0.53}$	< 1.51	< 2.34	< 3.33
627	< 3.12	$6.37^{+1.40}_{-1.40}$	$1.78^{+0.24}_{-0.00}$	$3.99^{+0.44}_{-0.42}$	$4.11^{+0.57}_{-0.58}$	< 1.82	< 2.38	$16.02^{+2.23}_{-2.23}$
642	_	_	_	$1.25^{+0.14}_{-0.14}$	< 6.65	< 13.4	_	_
656	_	_	_	$3.57^{+1.53}_{-1.29}$	< 3.20	< 13.7	_	_
657	_	_	_	$2.61^{+0.31}_{-0.27}$	< 4.66	< 10.9	_	_
658	-	-	-	$8.65^{+3.25}_{-2.55}$	$1.45^{+0.37}_{-1.30}$	< 16.0	_	_
709	$2.15^{+0.64}_{-2.40}$	$10.76^{+2.33}_{-2.33}$	$3.93^{+1.29}_{-0.00}$	$9.72^{+1.11}_{-1.01}$	$6.27^{+0.84}_{-0.84}$	$1.81^{+0.33}_{-0.33}$	< 1.63	< 2.36
715	$2.91^{+0.87}_{-3.24}$	$6.59^{+1.36}_{-1.36}$	$2.08^{+0.40}_{-0.85}$	$6.97^{+1.76}_{-1.72}$	$3.72^{+0.55}_{-0.56}$	$5.03^{+1.11}_{-1.11}$	$1.74^{+0.71}_{-0.00}$	< 2.62
739	-	_	_	$3.00^{+0.36}_{-0.32}$	< 2.41	< 11.8	_	_
746	$2.53^{+0.76}_{-2.82}$	$8.97^{+1.97}_{-1.97}$	$1.29^{+0.29}_{-0.00}$	$7.29^{+0.98}_{-0.81}$	$6.00^{+0.87}_{-0.86}$	$1.27^{+0.29}_{-0.29}$	< 1.63	< 2.28
747	_	_	_	$9.28^{+1.22}_{-1.03}$	< 6.65	< 19.3	_	_
752	$2.41^{+0.72}_{-2.69}$	$11.35^{+2.24}_{-2.24}$	$4.34^{+1.99}_{-0.00}$	$12.9^{+1.7}_{-1.4}$	$6.16^{+0.80}_{-0.80}$	< 2.29	< 3.36	< 4.19
768	< 1.13	$5.30^{+1.18}_{-1.18}$	$0.97^{+0.45}_{-0.25}$	$2.63^{+0.29}_{-0.27}$	$2.43^{+0.44}_{-0.43}$	< 0.82	$2.39^{+0.25}_{-0.00}$	< 1.74
780	_	_	-	$3.03^{+0.35}_{-0.34}$	< 3.51	< 11.6	_	_
799	< 2.41	$7.33^{+1.54}_{-1.54}$	$0.41^{+0.11}_{-0.00}$	$7.18^{+1.11}_{-0.87}$	$3.57^{+0.45}_{-0.45}$	< 1.05	< 1.81	< 3.31
800	$1.87^{+0.56}_{-2.08}$	$3.73^{+0.76}_{-0.76}$	< 0.26	$8.34^{+1.12}_{-0.92}$	$4.10^{+0.53}_{-0.53}$	< 0.83	< 1.41	< 1.59

Note. COMs listed by increasing number of atoms. ¹ The cores observed with both the ARO 12 m and Yebes 40 m are bolded. For the italicized cores 67 and 658, the ARO 12 m RMS is lower, ~ 2 mK, than for the rest of the sample at ~ 6 mK. In the case of t-HCOOH and H₂CCO, errors encompass full range of *N* from the full range of assumed $T_{\rm ex}$ values, i.e. at 5 K, 10 K, and 20 K. Errors quoted as '0.00' are < 0.005.

cores as well as a selection of Class 0/I protostars, a Class II disc, and three comets.

5.2.1 Starless and pre-stellar cores

We first compare in the top panel of Fig. 18 the CH₃OH abundances of our sample of cores in Perseus to the cyanopolyyne peak (CP) of the dense cloud TMC-1 (Soma et al. 2015; Gratier et al. 2016; Soma et al. 2018; Agúndez et al. 2021), as well as the dust peak of a sample of other starless and pre-stellar cores with COM detections and/or upper limits, i.e. L1517B; Megías et al. (2023), L1512E; Nagy et al. (2019); Scibelli et al. (2021), the 22 cores in the L1495 filament; Scibelli & Shirley (2020), L1498; Jiménez-Serra et al.

(2021), L1544; Vastel et al. (2014); Jiménez-Serra et al. (2016, 2021), L183; Lattanzi et al. (2020), and L1689B; Bacmann et al. (2012).

We find for O-bearing species abundances are similar, i.e. within roughly one order of magnitude, as seen in Scibelli et al. (2021). However, more than one order of magnitude drop in abundance is seen for the N-bearing species CH₃CN and CH₂CHCN when comparing between cores with detections in Taurus compared to the Perseus cores. Though, the upper limit for the young Taurus core L1517B does show a similar drop in CH₂CHCN/CH₃OH abundances.

In Table 4 we list all median values, along with standard deviations, for COM abundances with respect to CH₃OH (as well as H₂

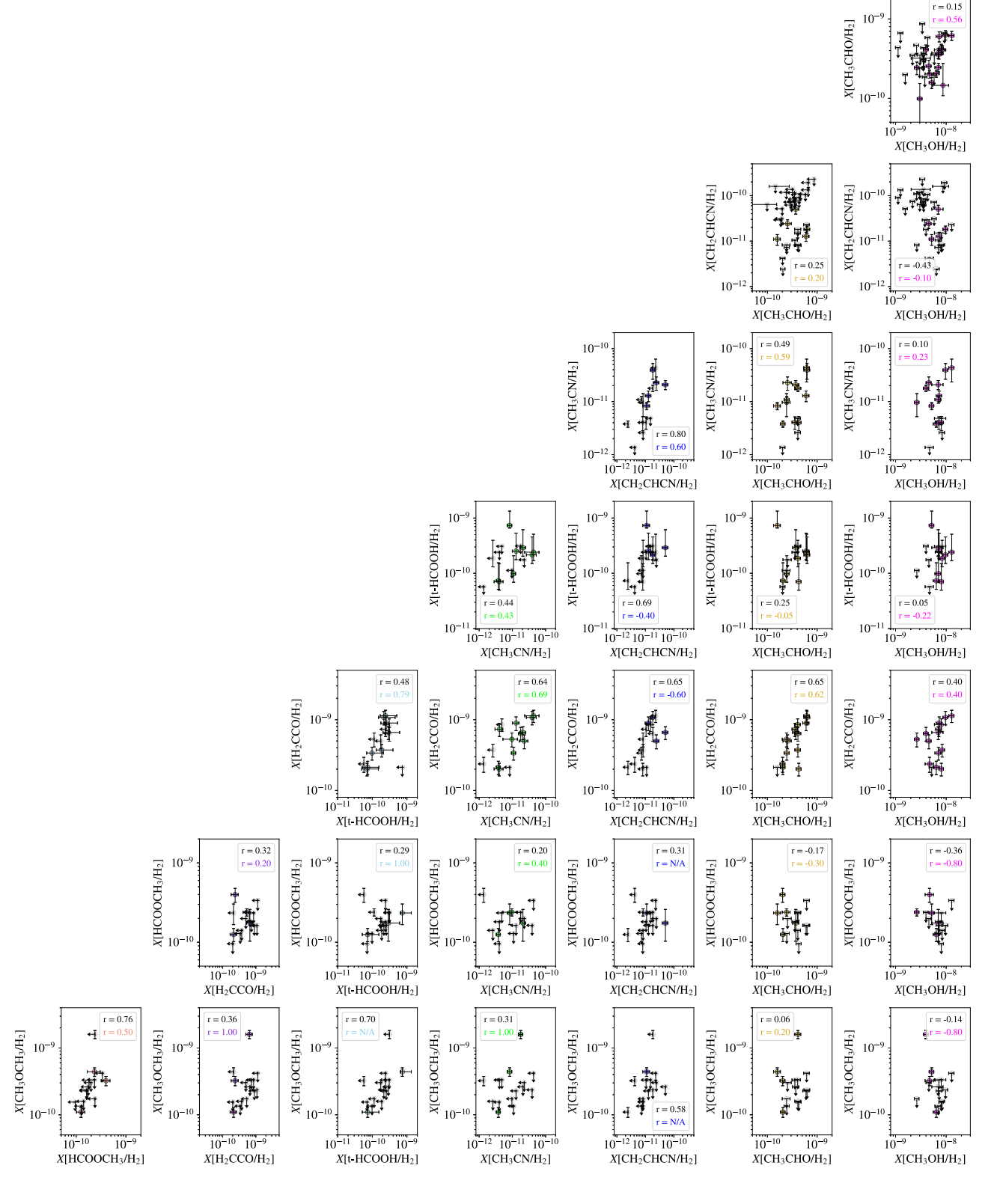


Figure 16. Correlation corner plot for the eight species of COMs in this study plotted as abundances with respect to H_2 . In the rightmost column are CH_3OH abundances (magenta points) with the following columns plotting abundances of CH_3CHO (gold points), CH_2CHCN (blue points), CH_3CN (green points), t-HCOOH (light blue points), H_2CCO (purple points), and $HCOOCH_3$ (orange points). In the case where either or both correlated molecules are not detected, upper limits are plotted with arrows (in grey). In each panel the Spearman rank correlation coefficient 'r' is reported for the full sample of cores, including upper limits, in the first line of the legend (black text), as well as the 'r' value for only the sample cores with detections of both molecules being compared in the last line of the legend (coloured text). Note: if there are < 3 points 'r' is reported as 'N/A'.

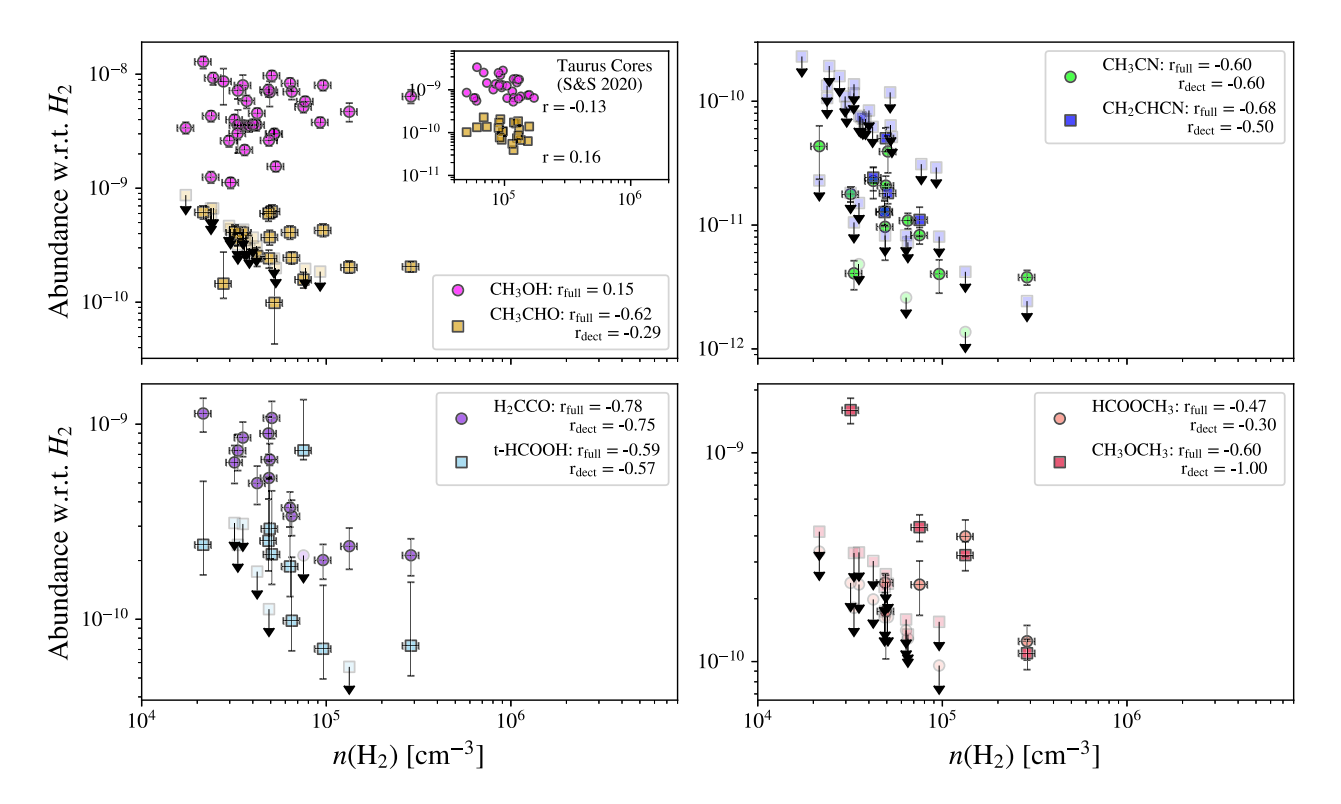


Figure 17. Comparison of COM abundances with respect to H_2 to the average H_2 volume density, $n(H_2)$ in units of cm⁻³ for each of the cores in our sample. The Spearman rank correlation coefficient, noted here as r, is included in the legend in each panel. In most cases a negative r value is found, suggesting the COM abundances drop with increasing volume density. Error bars, including a 10 per cent error in $n(H_2)$, are plotted in black. Upper limits are shown as slightly more translucent points with black downward facing arrows. We note 'r' is calculated both for the full sample of cores (including upper limits) as well as only the cores with detections. An insert plot in the top left panel compares the abundance and density range for the sample of Taurus cores presented in Scibelli & Shirley (2020), where error-bars have been removed for clarity.

and CH₃CN). Representative of the O-bearing and N-bearing species, respectively, the median CH₃CHO/CH₃OH and CH₃CN/CH₃OH ratios in the Perseus sample (plotted as gold and green dashed lines in Fig. 18) are offset by a factor of 25. If we compare this to the Taurus cores with detections of both CH₃CHO and CH₃CN, the offset in this methanol abundances ranges from factors of 1.3 to 6.7. This gap in the abundance of N-bearing COMs with respect to CH₃OH compared to O-bearing COMs in Perseus that is not seen in the sample of cores we have in the Taurus molecular cloud could suggest different O/N ratios towards these two clouds.

In order to test this, we first look at the median abundance ratio of our two N-bearing molecules, CH2CHCN/CH3CN, which is 1.06 \pm 0.27 for our Perseus sample of cores (Table 4). Compared to the Taurus cores with detections of both molecules, the ratio is slightly enhanced where CH₂CHCN/CH₃CN for TMC-1 is ~ 1.58, for L1521E \sim 2.1, and L1544 \sim 1.9. For those cores with upper limits, interestingly CH₂CHCN/CH₃CN in core L1498 is > 16 and in core L1517B < 0.22 (see Fig. 18). Still, the median value for all Taurus cores is enhanced at 1.94 ± 0.36 , which suggests a different O/N ratio is likely not the reason for the N-bearing and O-bearing COM abundance discrepancy, i.e. rather than a standardized inventory of enhanced 'N', the formation efficiency of CH2CHCN may instead be diminished in Perseus. And, we know from observations across the molecular filaments in Taurus and Perseus (that avoid protostars, H II regions and outflows) the ratio of the simpler O- to N- species HCO+/HCN and H¹³CO+/H¹³CN have been found to be within a factor of ~ 1 (Rodríguez-Baras et al. 2021).

It may also be that N-bearing COMs are probing the chemical evolution in starless and pre-stellar cores. As discussed by Megías et al. (2023), it is possible that N-bearing and O-bearing COMs form at different dynamical time-scales with N-bearing species forming first and bigger molecules forming later on, based on the detections in L1517B, L1498, and L1544. Though, this scenario breaks down for the chemically young core L1521E and chemically rich TMC-1, also believed to be young (see Fig. 18).

If we look at our sample of Perseus cores, we find for core 413, which has the most confident CH₂CHCN detection (i.e. two transitions at $> 3\sigma$), there are no HCOOCH₃ or CH₃OCH₃ detections. While core 264 is the only core where we detect all three molecules, CH₂CHCN, HCOOCH₃ and CH₃OCH₃ (Figs 8, 9, and 10). Using density as a simple evolutionary tracer, it may be that core 413, with an average H₂ abundance of $n(H_2) = 0.42 \times 10^5 \text{ cm}^{-3}$ is less evolved than core 264, with $n(H_2) = 0.75 \times 10^5 \text{ cm}^{-3}$ (Table 1). It should be noted that for the densest core 326, at $n(H_2) = 2.87 \times 10^5$ cm⁻³, there are strong detections of both HCOOCH3 and CH3OCH3, yet we do not see CH₂CHCN. In this case, environmental effects may play a bigger role in the chemistry, as it sits directly along the path of the CO outflows from nearby protostar SVS 13 (Plunkett et al. 2013). Interestingly, looking at Fig. 17, CH2CHCN is only detected in a narrower range of densities, from $n(H_2) = 0.42 - 0.75 \times 10^5 \text{ cm}^{-3}$, when compared to the full sample of cores observed. As for CH₃CN, this COM is seen over much wider range of densities and in cores both rich in the higher complexity O-bearing species (HCOOCH₃ and CH₃OCH₃) as well as CH₂CHCN.

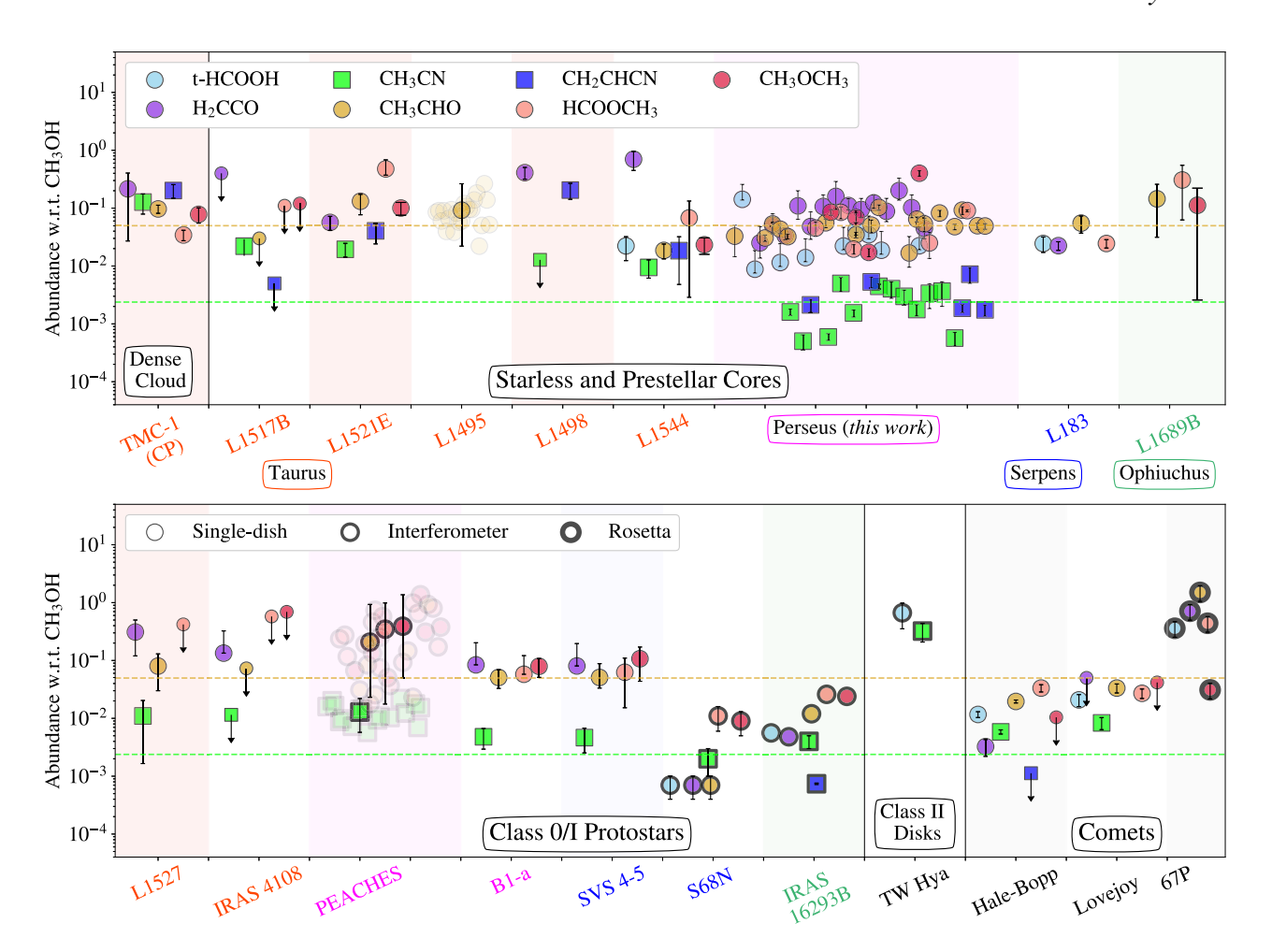


Figure 18. A comparison of CH₃OH abundances across the stages of low-mass star formation, including a large sample of starless and pre-stellar cores (upper panel), as well as for a selection of protostars, discs, and comets (lower panel). Vertical dashed lines represents the median CH₃CHO and CH₃CN values (Table 4), respectively (in gold and green), from the Perseus starless and pre-stellar core sample presented in this work. Values for the dense cloud TMC-1 are at the cyanopolyyne peak, or CP (Soma et al. 2015, 2018; Gratier et al. 2016; Agúndez et al. 2021). For the starless and pre-stellar cores, we compare only to dust peak measurements (L1517B; Megías et al. 2023, L1512E; Nagy et al. 2019; Scibelli et al. 2021, L1495; Scibelli & Shirley 2020, L1498; Jiménez-Serra et al. 2021, L1544; Vastel et al. 2014; Jiménez-Serra et al. 2016, 2021, L183; Lattanzi et al. 2020, and L1689B; Bacmann et al. 2012). Protostars are further distinguished by whether observations where made with a single-dish or interferometer by the thickness of the marker (L1527; Yoshida et al. 2019, PEACHES; Yang et al. 2021, IRAS 4108, B1-a, SVS 4–5; Graninger, Wilkins & Öberg 2016; Bergner et al. 2017, S68N; van Gelder et al. 2020; Nazari et al. 2021, and IRAS 16293B; Calcutt et al. 2018; Jørgensen et al. 2018). For the sources that are made up of a large samples of cores, i.e. 'L1495' and 'PEACHES', we plot the average values and the spread in the sample as error bars, where the sample is also shown by more translucent markers. The Class II disc, TW Hya, is plotted from interferometer measurements detailed in Walsh et al. (2016); Favre et al. (2018); Loomis et al. (2018). Lastly, we also include radio observations of the long-range comets, Hale-Bop and Lovejoy (Biver & Bockelée-Morvan 2019), as well as Jupiter-family comet, 67P/Churyumov–Gerasimenko or 67P, from measurements taken with the mass spectroscopy instrument aboard the *Rosetta* mission (Hänni et al. 2023).

Table 4. Median abundances for Perseus starless and pre-stellar cores.

Species	$X/H_2 \times 10^{-10}$	X/CH ₃ OH	X/CH ₃ CN
t-HCOOH	2.15(0.76)	0.022(0.011)	15.7(5.28)
H ₂ CCO	5.83(2.58)	0.098(0.036)	35.8(13.8)
CH ₃ CN	0.119(0.078)	0.002(0.001)	1
CH ₃ OH	43.1(16.74)	1	450(200)
CH ₃ CHO	3.56(1.14)	0.050(0.015)	22.8(7.73)
CH ₃ CHCN	0.181(0.060)	0.002(0.004)	1.06(0.27)
$HCOOCH_3$	2.34(0.59)	0.045(0.026)	26.4(4.16)
CH ₃ OCH ₃	3.82(1.65)	0.077(0.034)	53.1(24.2)
O-bearing	3.69(1.45)	0.050(0.025)	31.1(11.8)
N-bearing	0.150(0.031)	0.002(0.001)	1.06(0.27)

Note. Values reported are for the subset(s) of detected cores. The standard deviation of each median value is reported in parentheses.

So, while the exact evolutionary stage of a core may be difficult to probe by just looking at the presence of N-bearing COMs, what could be different in the Perseus and Taurus cores is the rate at which the cores are evolving, or rather the time-scale on which the core is collapsing. If the N-bearing COMs are forming first, as proposed in Megías et al. (2023), this process may be happening more quickly in Perseus and CH₃CN and CH₂CHCN may experience freeze-out (as discussed in Section 5.1) earlier and thus we see a drop in the gas-phase abundances compared to the O-bearing species that have formed later. There is contradictory evidence, however, for this proposed scenario, e.g. the prevalence of CH₃CN across a variety of cores at different densities in Perseus and the lack of correlation between the cores with detection of both CH₃CN and CH₂CHCN (see Fig. 18).

It is more likely there are compounding effects, both environmental and evolutionary, that influence COM abundances with respect to $\mathrm{CH_3OH}$ for starless and pre-stellar cores in the localized regions within both Taurus and Perseus. A more thorough analysis should be done to differentiate the evolutionary stages of each of the Perseus cores (e.g. such as measuring CO depletion factors or isotopologue fractions) and to characterize the local environment in order to further explore this difference in the N-bearing and O-bearing COM abundances with respect to methanol.

5.2.2 Protostars

Next, we look at the Class 0/I protostars in the bottom panel of Fig. 18 to find the O-bearing COMs are generally consistent within an order of magnitude, suggesting at least some of the chemical inventory in the cold core stage is being inherited to the protostellar stage. For the N-bearing COMs (specifically CH₃CN), lower abundances are found with respect to CH₃OH than the O-bearing COMs across not only the sample protostars, but also the sample of starless and prestellar cores (excluding TMC-1; Fig. 18). The singular CH₂CHCN data point also falls below the O-bearing COM abundances from ALMA observations of IRAS 16293B (Calcutt et al. 2018). An outlier, the S68N protostar does show t-HCOOH, H₂CCO, and CH₃CHO abundances falling below CH₃CN in Fig. 18, yet Nazari et al. (2021) find that when comparing to a larger variety of Nbearing COMs, they are roughly an order of magnitude lower in abundance than the O-bearing COMs, which is not only true for S68N but for several other protostars as well (i.e. compare fig. 7 in van Gelder et al. 2020 and fig. 7 in Nazari et al. 2021). The consistency in this general trend of N-bearing COMs being lower in abundance than O-bearing species in cold cores and protostars further suggests that there is a limited reprocessing of material as cores evolve.

Looking only in Perseus, we find that when compared to the cold cores in our sample (i.e. the median CH_3CN/CH_3OH line in Fig. 18) the abundance for the N-bearing species CH_3CN is $\sim 2\times$ higher in the bright Perseus B1-a source taken with single-dish data (Bergner et al. 2017) and $\sim 6\times$ higher when compared the abundances from the full PEACHES sample derived from ALMA observations (Yang et al. 2021). While Yang et al. (2021) speculated seeing a decrease of CH_3CN/CH_3OH from the pre-stellar to the protostellar phase in Perseus, here we see the opposite, potentially evidence that warmphase grain-surface pathways may release back into the gas-phase the CH_3CN and CH_2CHCN species and regulate the abundances seen in later stages in Perseus.

The lack of statistics of both O-bearing and N-bearing species in protostars in Taurus make it more difficult to draw robust conclusions about COM inheritance in comparison to Perseus. The CALYPSO survey, originally meant for studying the angular momentum problem in protostars, was not sensitive enough to detect COM emission towards the three protostars in their sample located in Taurus (IRAM04191, L1521F, and L1527; Belloche et al. 2020). Despite limited detections, it is evident that the Taurus protostars follow the same general trend as the protostars in Perseus (as well as for Serpens and Ophiuchus), i.e. N-bearing COMs are in lower abundances than O-bearing COMs, and thus it is unclear how the different clouds may affect COM abundances in this stage. We note that there has been a direct comparison ALMA study (matched to the same sensitivity and resolution as PEACHES) in the massive star forming region of Orion (named 'ORANGES'), which does find that a lower fraction, 29 per cent, of the 19 solar-mass Class 0/I protostars targeted show CH₃OH emission when compared to the PEACHES survey (Bouvier et al. 2022). More analysis of abundance ratios need to be done, however, in order to conclude if environmental factors indeed play a large role in the complex chemical evolution at the protostellar stage.

We also point out, as Yang et al. (2021) show (their fig. 17), that the abundances of both the N-bearing species CH₃CN and O-bearing species CH₃CHO, HCOOCH₃, and CH₃OCH₃ in the PEACHES sample are systematically higher than for other isolated protostars in different environments also observed with ALMA (as we show for S68N and IRAS 16293B in Fig. 18), though, again, in both single-dish and interferometric measurements O-bearing species are generally enhanced compared to N-bearing species. A proper study of the statistics and sampling biases in these literature values of protostars should be done in order to say more.

5.2.3 Protoplanetary discs

Constraining the COM inventory in the next stage of low-mass star formation, Class II discs, remains a challenge. In Fig. 18 we plot two abundances constraints from the T-Tauri disc TW HYa using column density values for CH₃OH (Walsh et al. 2016), t-HCOOH (Favre et al. 2018), and CH₃CN (Loomis et al. 2018). The t-HCOOH/CH₃OH and CH₃CN/CH₃OH ratio in TW HYa is $\sim 20\times$ and $\sim 160\times$ higher, respectively, than the median values found in our Perseus sample of starless and pre-stellar cores (Table 4). Still, the lower abundance of CH₃CN compared to t-HCOOH may suggest even at this later stage there is a limited reprocessing of the chemical inventory inherited from the pre-stellar phase.

Beyond TW HYa, the detection of higher complexity COMs in T-Tauri discs remains elusive. There are constraints for discs with higher mass stars at their centres, such as the Herbig discs IRS 48 and HD 100546, where CH₃OH, HCOOCH₃, and CH₃OCH₃ (in IRS 48 only) have been detected (Booth et al. 2024a, b). The abundances of this warm reservoir of gas interestingly show even higher abundances of HCOOCH₃ and CH₃OCH₃ when compared to CH₃OH, i.e. for IRS 48 peak values for HCOOCH₃/CH₃OH \sim 20 and CH₃OCH₃/CH₃OH \sim 6. Though, as the authors point out, these above unity ratios may be due to high optical depth of the CH₃OH emission in discs and future work studying isotopic species such as 13 CH₃OH is needed to say more about whether differences in CH₃OH abundances in protoplanetary discs is really due to a potential re-processing of CH₃OH.

5.2.4 Comets

Lastly, in Fig. 18 we plot abundances of COMs with respect to CH₃OH for the long-range comets Hale-Bopp and Lovejoy (Biver & Bockelée-Morvan 2019), which show good agreement with abundance values in starless cores and protostars. We also include measurements taken with the mass spectroscopy instrument aboard the Rosetta mission for the Jupiter-family comet 67P/Churyumov-Gerasimenko or 67P (Hänni et al. 2023). For 67P, the data from a mass spectroscopy analysis should be taken lightly as it can be difficult to disentangle individual isomers (i.e. for HCOOCH3 this includes methyl formate, acetic acid, and glycolaldehyde), and because in this study 67P was analysed during a 'very dusty' period close to the comet's perihelion when heavy organics are expected to be released. In fact, it is only in the recent analysis of 67P where CH₃CHO₃ has been claimed, as it was not seen in its previous analysis (Schuhmann et al. 2019). Irrespective of exact abundance values, the presence of these complex species throughout low-mass star formation, from cores to comets, warrants further investigation into their formation and possible inheritance across a larger range of environments.

5.3 Implications for COM formation

In order to get COMs into the gas-phase in starless and pre-stellar cores, current models rely on the inclusion of chemical reactive desorption (CRD) and gas-phase radiative associations at often high chemical desorption efficiencies, such as the model of the evolved pre-stellar core L1544 detailed in Vasyunin et al. (2017), based on the work in Vasyunin & Herbst (2013). The basis of this work has then been applied to other cores with varying degrees of success. For example, Scibelli et al. (2021) find that CRD plus gas-phase chemistry alone is not sufficient to explain observed COMs in the chemically young starless core L1521E. Yet, Jiménez-Serra et al. (2021) find it does relatively well for the chemically evolved but dynamically young starless core L1498. Additional methods to increase COM gas-phase abundances include the incorporation of non-diffusive grain-surface processes (Jin & Garrod 2020), Eley-Rideal processes (Ruaud et al. 2015), cosmic-ray radiation chemistry (Shingledecker & Herbst 2018; Shingledecker et al. 2018), cosmicray sputtering (Wakelam et al. 2021; Paulive, Carder & Herbst 2022), and turbulence induced desorption due to collisions (Kalvāns & Silsbee 2022). Below we give a general overview of predicted model abundances that are able to match (within order-of-magnitude agreement) our observations.

5.3.1 O-bearing COMs

The formation of CH₃OH is known to proceed efficiently through the hydrogenation of CO on icy grains (Charnley et al. 1992). Relevant to cold (\sim 10 K) cores, there is additional motivation for the reaction with radicals CH₃ and H₂CO that leads to the formation of CH₃OH and the radical HCO that can go on to aid in the formation of additional COMs (Santos et al. 2022). Within CRD models (e.g. in Scibelli et al. 2021), CH₃CHO is formed from the slow radiative association of CH3 + HCO and the neutral-neutral reaction of CH + CH₃OH (Johnson, Blitz & Seakins 2000). The models of Vasyunin et al. (2017) and Scibelli et al. (2021) do predict abundances (with respect to H₂) of CH₃CHO at $\sim 10^{-10}$, which is within orderof-magnitude agreement with the range of abundances for the Perseus cores (Table 4). For the 5-atom species H₂CCO and t-HCOOH, the CRD models of Jiménez-Serra et al. (2021) and Megías et al. (2023) are also able to produce abundances comparable to what we see in our Perseus cores, \sim a few $\times 10^{-10}$.

For the higher complexity species HCOOCH3 and CH3OCH3, explaining the presence of such high gas-phase abundances (a few \times 10⁻¹⁰) has not been as easy for the CRD models. For example, Scibelli et al. (2021) find no agreement between model ($\sim 10^{-12}$) and observed ($\sim 10^{-10}$) abundances of HCOOCH₃ and CH₃OCH₃ toward core L1521E. More recent analysis that includes the addition of cosmic ray sputtering, for example, can get abundances up to the levels we see in the Perseus cores (e.g. in Paulive et al. (2022) their model 8HSC10). Turbulence-induced desorption from the models of Kalvāns & Silsbee (2022) may also be able to increase the gas-phase abundances of HCOOCH3 and CH3OCH3 in particular (see their table 2 'max' model). It should also be noted that for the handful of cores in our Perseus survey with detections of HCOOCH3 and CH₃OCH₃ they mainly reside in the active and shocked region of NGC1333 (e.g. cores 264, 321, and 326) and thus there are likely compounded interactions towards some of our sources from thermal processes (e.g. shocks or outflow interactions) that may be able to

more efficiently get these radical species and COMs off the grains. As evident for cores 264 and 326, independent RADEX fits of HCOOCH₃ find enhanced T_k values of $\sim 20 \,\mathrm{K}$ (see Appendix D).

Given the wide range of physical and environmental conditions of these Perseus cores, more detailed modelling on a case-by-case basis would be needed to say more about exact COM formation mechanisms. Still, despite variations, the range of calculated Obearing COM abundances for these starless and pre-stellar cores in Perseus can in general be described by chemical models that include non-thermal desorption mechanisms.

5.3.2 N-bearing COMs

The presence and formation of N-bearing COMs in pre-stellar cores remains more of a mystery. CH₂CHCN is of particular interest because it is thought to be one of the strongest candidates for forming membranes of potential astrobiological importance. Stevenson et al. (2015) showed that through theoretical liquid-phase calculations, CH₂CHCN is one of the most favoured to form these thermodynamically stable membranes in liquid methane at the surface temperature of Titan. Recent observations of Titan with ALMA have been successful in detecting CH₂CHCN (Palmer et al. 2017), highlighting the molecules' significance in astrobiology.

Toward the starless core L1498, CH₂CHCN is detected towards the dust peak, while CH₃CN is only detected towards the methanol peak (Jiménez-Serra et al. 2021). Conversely, towards core L1517B they do not detect CH₂CHCN at either the dust or methanol peak, yet do in fact detect CH₃CN at only the dust peak (Megías et al. 2023). In both studies, they use a CRD model to attempt to reproduced abundance constraints and are unable to do so for CH₂CHCN, which in their models reach abundances with respect to H₂ $\sim 10^{-13}$ (note in Scibelli et al. (2021) they reproduce higher values $\sim 10^{-12}$). Even for CH₃CN, the CRD models have trouble reproducing values above $\sim 10^{-11}$, which would be consistent with our Perseus observations (see Table 4).

In the case of CH₂CHCN, the gas-phase production routes are known to be inefficient [e.g. KIDA data base; Wakelam et al. (2012)]. Despite this, we have shown that similar to the O-bearing COMs (excluding grain-produced CH₃OH), the abundances with respect to H₂ for the N-bearing COMs may also deplete with increasing volume density (Fig. 17), suggesting gas-phase formation may still be important. Giani et al. (2023) show for CH₃CN there are efficient routes in the gas-phase that can produce rather high abundances, $\sim 10^{-10}$, when modelled for the dark cloud TMC-1. Perhaps for CH₂CHCN other gas-phase formation routes are more efficient and/or the reactive desorption efficiency for this molecule is particularly high. The other desorption studies mentioned here unfortunately do not provide constraints for N-bearing COM abundances (Ruaud et al. 2015; Shingledecker & Herbst 2018; Shingledecker et al. 2018; Jin & Garrod 2020; Wakelam et al. 2021; Kalvāns & Silsbee 2022; Paulive et al. 2022). We therefore stress that additional experimental and theoretical work on efficient gas and grain chemical pathways and desorption mechanisms of N-bearing COMs are still needed to explain the abundances (a few $\times \sim 10^{-11}$) we find for CH₂CHCN and CH₃CN in the starless and pre-stellar cores in Perseus.

6 CONCLUSIONS

We find a prevalence of COMs in starless and pre-stellar cores in the Perseus molecular cloud from a combined ARO 12 m and Yebes 40 m molecular line survey, more than doubling the

COM abundance statistics for cold (\sim 10 K) cores. We detect CH₃OH (100 per cent: 35/35), CH₃CHO (49 per cent: 17/35), H₂CCO (93 per cent: 14/15), t-HCOOH (60 per cent: 9/15), CH₃CN (80 per cent: 12/15), CH₂CHCN (< 34 per cent), HCOOCH₃ (< 34 per cent) and CH₃OCH₃ (< 27 per cent) in multiple cores, but in no single core were all these molecules detected. Our main conclusions

- (i) We find CH₃OH and CH₃CHO are just as prevalent, if not more so, in our sample of 35 cores in the roughly $2\times$ farther Perseus molecular cloud when compared to the COM survey of 31 starless and pre-stellar cores in the nearby (135 pc) L1495/B218 filament of the Taurus molecular cloud (Scibelli & Shirley 2020). Moreover, CH₃CHO is likely widespread, as evident from detections of this molecule in the randomly selected cores 67 and 658 when higher sensitivity (\sim 2 mK) observations were carried out.
- (ii) Most starless and pre-stellar cores in our survey reside in the active Perseus clusters NGC 1333 and IC 348, which are the regions that show increased COM complexity. It is within these regions where not only are there detections of higher complexity COMs in the pre-stellar stage, there is also an increase in COM detections in the warm protostellar stage when compared to the spatial location of the PEACHES sample (Yang et al. 2021).
- (iii) By combining multiple CH₃OH transitions with varying beam sizes, we account for the true emitted source size during our column density calculations. The total CH₃OH column densities, $N(\text{CH}_3\text{OH})$, for the 35-core sample range from $0.87-50.27\times10^{13}~\text{cm}^{-2}$ with a median source size of 38.5 ± 4 arcsec.
- (iv) When normalized to molecular hydrogen, we find for the Obearing COMs abundances that range from $2.15-43.1\times 10^{-10}$. For the N-bearing COMs we find roughly an order of magnitude lower abundances, with a values ranging from $0.118-0.181\times 10^{-10}$.
- (v) From an abundance correlation analysis, we find no significant positive correlation (r = 0.10/0.23, for the detected and full sample, respectively) with the CH₃CN/CH₃OH abundances, which is unlike what is seen towards the nearby protostars in Perseus (Belloche et al. 2020; Yang et al. 2021). We do find significant (r > 0.5) correlation for the following pairs of molecular abundances: CH₃OCH₃/HCOOCH₃ (r = 0.76/0.50), CH₃CN/CH₂CHCN (r = 0.80/0.60), H₂CCO/CH₃CN (r = 0.64/0.69), and H₂CCO/CH₃CHO (r = 0.65/0.62).
- (vi) We find COM abundances (excluding CH_3OH) with respect to H_2 decrease with increasing average volume density, $n(H_2)$, which is most likely due to depletion effects, where in the densest cores, molecules will freeze-out onto the grains. Additional observations that can map the spatial distribution of COMs in starless and prestellar cores are needed to better trace potential freeze-out and compare to chemical models.

(vii) By normalizing abundances to the grain-produced species CH₃OH, we also compare COM abundances in our Perseus sample to a large sample of other starless and pre-stellar cores, as well as to a sample of Class 0/I protostars, a Class II T-Tauri disc, and a handful of comets. In general, the similarity in O-bearing COM abundances throughout each stage suggests at least some of the COMs in the pre-stellar stage are being inherited to the later stages. Perhaps most notable, compared to starless and pre-stellar cores in Taurus, we find for our Perseus sample the abundances of N-bearing COMs are ~20 times lower, whereas the O-bearing COMs are in agreement (~ within an order of magnitude). This discrepancy in N-bearing abundances within the Perseus starless and pre-stellar cores suggests that perhaps different environmental effects are at play and/or these cores are evolving at a different rate compared to those sampled in

Taurus. In the later stages, N-bearing species tend to also be lower in abundance with respect to methanol than O-bearing species, which further motivates that there is a limited amount of reprocessing of the complex chemical inventory throughout low-mass star formation.

(viii) Despite variation in environment and evolutionary stage (i.e. varying densities) of the cores, the molecular hydrogen abundances for the O-bearing species are consistent with chemical models that rely on non-thermal desorption mechanisms to get COMs into the gas-phase. However, echoing the work of Jiménez-Serra et al. (2021) and Scibelli et al. (2021), more experimental and theoretical work needs to be done in order to reproduce abundances of N-bearing COMs in the starless and pre-stellar core phase. A more detailed analysis for these individual cores in Perseus, taking into account their physical and environmental conditions, will be needed to say more about the dominate reaction and formation pathways for the COMs studied.

Overall, our synergistic observations of molecular line emission in both the 3 and 7 mm (Q-band) regime has proven to be a powerful mechanism for studying the complex chemistry of cold ($10\,\mathrm{K}$) molecular gas in starless and pre-stellar cores, which represent one of the earliest stages in low-mass star formation that precedes the formation of Sun-like stars and potentially Earth-like planets.

ACKNOWLEDGEMENTS

We thank Yao-Lun Yang for providing comparison data from the PEACHES survey that improved this paper. Additionally, we thank our anonymous reviewer for their constructive comments. We are thankful that we have the opportunity to conduct astronomical research on Iolkam Du'ag (Kitt Peak) in Arizona and we recognize and acknowledge the very significant cultural role and reverence that these sites have to the Tohono O'odham Nation. We sincerely thank the operators of the Arizona Radio Observatory (Michael Begam, Kevin Bays, Clayton Kyle, and Robert Thompson) for their assistance with the observations. The 12 m Telescope is operated by the Arizona Radio Observatory (ARO), Steward Observatory, University of Arizona, with funding from the State of Arizona, NSF MRI Grant AST-1531366 (PI Ziurys), NSF MSIP grant SV5-85009/AST- 1440254 (PI Marrone), NSF CAREER grant AST-1653228 (PI Marrone), and a PIRE grant OISE-1743747 (PI Psaltis).

We also acknowledge observations carried out with the Yebes 40 m telescope (22A022 and 23A025). Paula Tarrío and Alba Vidal García carried out the observations and the first inspection of the data quality. The 40 m radio telescope at Yebes Observatory is operated by the Spanish Geographic Institute (IGN; Ministerio de Transportes, Movilidad y Agenda Urbana). Yebes Observatory thanks the European Union's Horizon 2020 research and innovation programme for funding support to ORP project under grant agreement No 101004719.

Support for SS and YS was provided by National Science Foundation Astronomy and Astrophysics Grant (AAG) AST-2205474 as well as the Universities Space Research Association (USRA) Stratospheric Observatory of Infrared Astronomy (SOFIA) grant 9–0155. SS acknowledges the National Radio Astronomy Observatory is a facility of the National Science Foundation operated under cooperative agreement by Associated Universities, Inc. AM has received support from grant number PRE2019-091471 funded by the MICIU/AEI/10.13039/501100011033 and by 'ERDF/EU'. IJS and AM acknowledge financial support from grants No. PID2019-105552RB-C41 and PID2022-136814NB-I00 funded by MICIU/AEI/ 10.13039/501100011033 and by 'ERDF/EU'.

DATA AVAILABILITY

The CLASS/PYTHON reduction pipeline is available on github: https://github.com/andresmegias/gildas-class-python/. The reduced spectra ($T_{\rm mb}$ scale) presented in this paper is available on the Harvard Dataverse at the following link: https://doi.org/10.7910/DVN/H4YZ4U.

REFERENCES

Agúndez M., Marcelino N., Tercero B., Cabezas C., de Vicente P., Cernicharo J., 2021, A&A, 649, L4

Agúndez M., Marcelino N., Tercero B., Cernicharo J., 2023, A&A, 677,

Ambrose H. E., Shirley Y. L., Scibelli S., 2021, MNRAS, 501, 347

Bacmann A., Taquet V., Faure A., Kahane C., Ceccarelli C., 2012, A&A, 541, L12

Ball J. A., Gottlieb C. A., Lilley A. E., Radford H. E., 1970, ApJ, 162, L203

Balucani N., Ceccarelli C., Taquet V., 2015, MNRAS, 449, L16

Bauder A., 1979, J. Phys. Chem. Ref. Data, 8, 583

Belloche A. et al., 2020, A&A, 635, A198

Bellet J., Samson C., Steenbeckliers G., Wertheimer R., 1971, J. Mol. Struct., 9, 49

Bergin E. A., Tafalla M., 2007, ARA&A, 45, 339

Bergner J. B., Öberg K. I., Garrod R. T., Graninger D. M., 2017, ApJ, 841, 120

Biver N., Bockelée-Morvan D., 2019, ACS Earth Space Chem., 3, 1550

Bizzocchi L., Caselli P., Spezzano S., Leonardo E., 2014, A&A, 569, A27

Booth A. S., Walsh C., Terwisscha van Scheltinga J., van Dishoeck E. F., Ilee J. D., Hogerheijde M. R., Kama M., Nomura H., 2021, Nat. Astron., 5, 684

Booth A. S. et al., 2024a, AJ, 167, 164

Booth A. S. et al., 2024b, AJ, 167, 165

Bouvier M., Ceccarelli C., López-Sepulcre A., Sakai N., Yamamoto S., Yang Y.-L., 2022, ApJ, 929, 10

Brown R. D., Crofts J. G., Gardner F. F., Godfrey P. D., Robinson B. J., Whiteoak J. B., 1975, ApJ, 197, L29

Brown R. D., Godfrey P. D., McNaughton D., Pierlot A. P., Taylor W. H., 1990, J. Mol. Spectrosc., 140, 340

Calcutt H. et al., 2018, A&A, 616, A90

Caselli P., Walmsley C. M., Tafalla M., Dore L., Myers P. C., 1999, ApJ, 523, L165

Caselli P., Walmsley C. M., Zucconi A., Tafalla M., Dore L., Myers P. C., 2002, ApJ, 565, 344

Caselli P. et al., 2019, ApJ, 874, 89

Caselli P. et al., 2022, ApJ, 929, 13

Cazzoli G., Kisiel Z., 1988, J. Mol. Spectrosc., 130, 303

Ceccarelli C. et al., 2022, preprint (arXiv:2206.13270)

Cernicharo J., Marcelino N., Roueff E., Gerin M., Jiménez-Escobar A., Muñoz Caro G. M., 2012, ApJ, 759, L43

Cernicharo J., Agúndez M., Kaiser R. I., Cabezas C., Tercero B., Marcelino N., Pardo J. R., de Vicente P., 2021, A&A, 652, L9

Charnley S. B., Tielens A. G. G. M., Millar T. J., 1992, ApJ, 399, L71

Chen H. H.-H. et al., 2019a, ApJ, 877, 93

Chen H. H.-H. et al., 2019b, ApJ, 886, 119

Chen M. C.-Y. et al., 2020, ApJ, 891, 84

Crapsi A., Caselli P., Walmsley M. C., Tafalla M., 2007, A&A, 470, 221

Drozdovskaya M. N., van Dishoeck E. F., Rubin M., Jørgensen J. K., Altwegg K., 2019, MNRAS, 490, 50

Durig J. R., Li Y. S., Groner P., 1976, J. Mol. Spectrosc., 62, 159

Endres C. P., Drouin B. J., Pearson J. C., Müller H. S. P., Lewen F., Schlemmer S., Giesen T. F., 2009, A&A, 504, 635

Endres C. P., Schlemmer S., Schilke P., Stutzki J., Müller H. S. P., 2016, J. Mol. Spectrosc., 327, 95

Enoch M. L., Evans N. J. II, Sargent A. I., Glenn J., Rosolowsky E., Myers P., 2008, ApJ, 684, 1240 Faure A., Remijan A. J., Szalewicz K., Wiesenfeld L., 2014, ApJ, 783, 72

Favre C. et al., 2018, ApJ, 862, L2

Friesen R. K. et al., 2017, ApJ, 843, 63

Gaia Collaboration, 2016, A&A, 595, A1

Gaia Collaboration, 2018, A&A, 616, A1
Galloway-Sprietsma M., Shirley Y. L., Di Francesco J., Keown J., Scibelli S.,
Sipilä O., Smullen R., 2022, MNRAS, 515, 5219

Gardner F. F., Winnewisser G., 1975, ApJ, 195, L127

Garrod R. T., Jin M., Matis K. A., Jones D., Willis E. R., Herbst E., 2022, ApJS, 259, 1

Giani L., Ceccarelli C., Mancini L., Bianchi E., Pirani F., Rosi M., Balucani N., 2023, MNRAS, 526, 4535

Gildas Team, 2013, Astrophysics Source Code Library, record ascl:1305.010 Goldsmith P. F., Langer W. D., 1999, ApJ, 517, 209

Graninger D. M., Wilkins O. H., Öberg K. I., 2016, ApJ, 819, 140

Gratier P., Majumdar L., Ohishi M., Roueff E., Loison J. C., Hickson K. M., Wakelam V., 2016, ApJS, 225, 25

Green S., 1986, ApJ, 309, 331

Hänni N. et al., 2023, A&A, 678, A22

Hatchell J., Fuller G. A., Richer J. S., 2007, A&A, 472, 187

Herbst E., van Dishoeck E. F., 2009, ARA&A, 47, 427

Hollis J. M., Lovas F. J., Jewell P. R., 2000, ApJ, 540, L107

Hunter J. D., 2007, Comput. Sci. Eng., 9, 90

Iglesias-Groth S., 2019, MNRAS, 489, 1509

Iglesias-Groth S., Marin-Dobrincic M., 2023, MNRAS, 521, 2248

Ilyushin V., Kryvda A., Alekseev E., 2009, J. Mol. Spectrosc., 255, 32

Imai M. et al., 2016, ApJ, 830, L37

Jiménez-Serra I. et al., 2016, ApJ, 830, L6

Jiménez-Serra I. et al., 2020, Astrobiology, 20, 1048

Jiménez-Serra I., Vasyunin A. I., Spezzano S., Caselli P., Cosentino G., Viti S., 2021, ApJ, 917, 44

Jin M., Garrod R. T., 2020, APJS, 249, 26

Johnson D. G., Blitz M. A., Seakins P. W., 2000, Phys. Chem. Chem. Phys., 2, 2549

Jørgensen J. K. et al., 2018, A&A, 620, A170

Jørgensen J. K., Belloche A., Garrod R. T., 2020, ARA&A, 58, 727

Kaifu N. et al., 2004, PASJ, 56, 69

Kalvāns J., Silsbee K., 2022, MNRAS, 515, 785

Karakawa Y., Oka K., Odashima H., Takagi K., Tsunekawa S., 2001, J. Mol. Spectrosc., 210, 196

Keto E., Caselli P., 2010, MNRAS, 402, 1625

Kleiner I., Lovas F. J., Godefroid M., 1996, J. Phys. Chem. Ref. Data, 25, 1113

Knee L. B. G., Sandell G., 2000, A&A, 361, 671

Kolesniková L., Tercero B., Cernicharo J., Alonso J. L., Daly A. M., Gordon B. P., Shipman S. T., 2014, ApJ, 784, L7

Kukolich S. G., 1982, J. Chem. Phys., 76, 97

Lai J. C. Y. et al., 2017, AJ, 154, 206

Lattanzi V., Bizzocchi L., Vasyunin A. I., Harju J., Giuliano B. M., Vastel C., Caselli P., 2020, A&A, 633, A118

Lin Y., Spezzano S., Pineda J. E., Harju J., Schmiedeke A., Jiao S., Liu H. B., Caselli P., 2023, A&A, 680, A43

Loomis R. A., Cleeves L. I., Öberg K. I., Aikawa Y., Bergner J., Furuya K., Guzman V. V., Walsh C., 2018, ApJ, 859, 131

López-Sepulcre A. et al., 2017, A&A, 606, A121

Lovas F. J., Lutz H., Dreizler H., 1979, J. Phys. Chem. Ref. Data, 8, 1051

Luhman K. L., Esplin T. L., Loutrel N. P., 2016, ApJ, 827, 52

Mangum J. G., 1993, PASP, 105, 117

Mangum J. G., Shirley Y. L., 2015, PASP, 127, 266

Matthews H. E., Friberg P., Irvine W. M., 1985, ApJ, 290, 609

McGuire B. A., Burkhardt A. M., Kalenskii S., Shingledecker C. N., Remijan A. J., Herbst E., McCarthy M. C., 2018, Science, 359, 202

McGuire B. A. et al., 2021, Science, 371, 1265

Megías A., Jiménez-Serra I., Martín-Pintado J., Vasyunin A. I., Spezzano S., Caselli P., Cosentino G., Viti S., 2023, MNRAS, 519, 1601

Minissale M., Dulieu F., Cazaux S., Hocuk S., 2016, A&A, 585, A24

Morgan L. K., Moore T. J. T., Eden D. J., Hatchell J., Urquhart J. S., 2014, MNRAS, 440, 1730

- Müller H. S. P., Thorwirth S., Roth D. A., Winnewisser G., 2001, A&A, 370,
- Müller H. S. P., Schlöder F., Stutzki J., Winnewisser G., 2005, J. Mol. Struct., 742, 215
- Nagy Z., Spezzano S., Caselli P., Vasyunin A., Tafalla M., Bizzocchi L., Prudenzano D., Redaelli E., 2019, A&A, 630, A136
- Nazari P. et al., 2021, A&A, 650, A150
- Öberg K. I., Bergin E. A., 2021, Phys. Rep., 893, 1
- Öberg K. I., Bottinelli S., Jørgensen J. K., van Dishoeck E. F., 2010, ApJ, 716, 825
- Öberg K. I., van der Marel N., Kristensen L. E., van Dishoeck E. F., 2011, ApJ, 740, 14
- Offner S. S. R. et al., 2022, MNRAS, 517, 885
- Ogata K., Odashima H., Takagi K., Tsunekawa S., 2004, J. Mol. Spectrosc., 225, 14
- Ohishi M., Kawaguchi K., Kaifu N., Irvine W. M., Minh Y. C., Yamamoto S., Saito S., 1991, in Haschick A. D., Ho P. T. P., eds, ASP Conf. Ser. Vol. 16, Atoms, Ions and Molecules: New Results in Spectral Line Astrophysics. Astron. Soc. Pac., San Francisco, p. 387
- Ortiz-León G. N. et al., 2018, ApJ, 865, 73
- Palmer M. Y., Cordiner M. A., Nixon C. A., Charnley S. B., Teanby N. A., Kisiel Z., Irwin P. G. J., Mumma M. J., 2017, Sci. Adv., 3, e1700022
- Pandhi A. et al., 2023, MNRAS, 525, 364
- Pattle K., Fissel L., Tahani M., Liu T., Ntormousi E., 2023, in Inutsuka S., Aikawa Y., Muto T., Tomida K., Tamura M., eds, ASP Conf. Ser. Vol. 534, Protostars and Planets VII. Astron. Soc. Pac., San Francisco, p. 193
- Paulive A., Carder J. T., Herbst E., 2022, MNRAS, 516, 4097
- Pety J., 2005, in Casoli F., Contini T., Hameury J. M., Pagani L., eds, SF2A-2005: Semaine de l'Astrophysique Francaise. EdP-Sciences, Strasbourg, France, p. 721
- Pezzuto S. et al., 2012, A&A, 547, A54
- Pezzuto S. et al., 2021, A&A, 645, A55
- Pickett H. M., Poynter R. L., Cohen E. A., Delitsky M. L., Pearson J. C., Müller H. S. P., 1998, J. Quant. Spec. Radiat. Transfer, 60, 883
- Pineda J. E. et al., 2015, Nature, 518, 213
- Pineda J. E. et al., 2022, AJ, 163, 294
- Plunkett A. L., Arce H. G., Corder S. A., Mardones D., Sargent A. I., Schnee S. L., 2013, ApJ, 774, 22
- Punanova A., Vasyunin A., Caselli P., Howard A., Spezzano S., Shirley Y., Scibelli S., Harju J., 2022, ApJ, 927, 213
- Rabli D., Flower D. R., 2010, MNRAS, 406, 95
- Requena-Torres M. A., Martín-Pintado J., Martín S., Morris M. R., 2008, ApJ, 672, 352
- Rivilla V. M. et al., 2022, ApJ, 929, L11
- Rodríguez-Baras M. et al., 2021, A&A, 648, A120
- Rosolowsky E. W., Pineda J. E., Foster J. B., Borkin M. A., Kauffmann J., Caselli P., Myers P. C., Goodman A. A., 2008, ApJS, 175, 509
- Ruaud M., Loison J. C., Hickson K. M., Gratier P., Hersant F., Wakelam V., 2015, MNRAS, 447, 4004
- Rubin M. et al., 2019, AGU Fall Meeting Abstracts, P43C
- Sadavoy S. I. et al., 2012, A&A, 540, A10
- Sadavoy S. I. et al., 2014, ApJ, 787, L18
- Sakai Y., Kobayashi K., Hirota T., 2015, ApJ, 803, 97
- Santos J. C., Chuang K.-J., Lamberts T., Fedoseev G., Ioppolo S., Linnartz H., 2022, ApJ, 931, L33
- Schlafly E. F. et al., 2014, ApJ, 786, 29
- Schuhmann M. et al., 2019, ACS Earth Space Chem., 3, 1854
- Scibelli S., Shirley Y., 2020, ApJ, 891, 73
- Scibelli S., Shirley Y., Vasyunin A., Launhardt R., 2021, MNRAS, 504, 5754 Scibelli S., Shirley Y., Schmiedeke A., Svoboda B., Singh A., Lilly J., Caselli
- P., 2023, MNRAS, 521, 4579 Seo Y. M. et al., 2015, ApJ, 805, 185
- Shingledecker C. N., Herbst E., 2018, Phys. Chem. Chem. Phys., 20, 5359
- Shingledecker C. N., Tennis J., Le Gal R., Herbst E., 2018, ApJ, 861, 20
- Snyder L. E., Buhl D., Schwartz P. R., Clark F. O., Johnson D. R., Lovas F. J., Giguere P. T., 1974, ApJ, 191, L79
- Soma T., Sakai N., Watanabe Y., Yamamoto S., 2015, ApJ, 802, 74
- Soma T., Sakai N., Watanabe Y., Yamamoto S., 2018, ApJ, 854, 116

- Spezzano S., Caselli P., Bizzocchi L., Giuliano B. M., Lattanzi V., 2017, A&A, 606, A82
- Stevenson J. M., Fouad W. A., Shalloway D., Usher D., Lunine J., Chapman W. G., Clancy P., 2015, Icarus, 256, 1
- Stolze M., Sutter D. H., 1985, Z. Naturforsch. A, 40, 998
- Tafalla M., Myers P. C., Caselli P., Walmsley C. M., Comito C., 2002, ApJ, 569, 815
- Taquet V., López-Sepulcre A., Ceccarelli C., Neri R., Kahane C., Charnley S. B., 2015, ApJ, 804, 81
- Tercero F. et al., 2021, A&A, 645, A37
- Thelen A. E. et al., 2020, ApJ, 903, L22
- Vastel C., Ceccarelli C., Lefloch B., Bachiller R., 2014, ApJ, 795, L2
- van Gelder M. L. et al., 2020, A&A, 639, A87
- van der Tak F. F. S., Black J. H., Schöier F. L., Jansen D. J., van Dishoeck E. F., 2007, A&A, 468, 627
- van der Tak F. F. S., Lique F., Faure A., Black J. H., van Dishoeck E. F., 2020, Atoms, 8, 15
- Vasyunin A. I., Herbst E., 2013, ApJ, 769, 34
- Vasyunin A. I., Caselli P., Dulieu F., Jiménez-Serra I., 2017, ApJ, 842, 33
- Vazart F., Ceccarelli C., Balucani N., Bianchi E., Skouteris D., 2020, MNRAS, 499, 5547
- Virtanen P. et al., 2020, Nat. Meth., 17, 261
- Wakelam V. et al., 2012, ApJS, 199, 21
- Wakelam V., Dartois E., Chabot M., Spezzano S., Navarro-Almaida D., Loison J. C., Fuente A., 2021, A&A, 652, A63
- Walsh C. et al., 2016, ApJ, 823, L10
- Wilson R. W., Jefferts K. B., Penzias A. A., 1970, ApJ, 161, L43
- Winnewisser M. et al., 2002, J. Mol. Spectrosc., 216, 259
- Xu L.-H. et al., 2008, J. Mol. Spectrosc., 251, 305
- Yang Y.-L. et al., 2021, ApJ, 910, 20
- Yoshida K., Sakai N., Nishimura Y., Tokudome T., Watanabe Y., Sakai T., Takano S., Yamamoto S., 2019, PASJ, 71, S18
- Zeng S. et al., 2018, MNRAS, 478, 2962
- Zucker C., Speagle J. S., Schlafly E. F., Green G. M., Finkbeiner D. P., Goodman A. A., Alves J., 2019, ApJ, 879, 125

APPENDIX A: SUPPLEMENTAL MATERIAL FROM ARO 12 M OBSERVATIONS

Additional details regarding the ARO 12 m observational setup (Section 3.1) are described here. First, while observations were underway we monitored two standard sources over the roughly two year span of observations. Science scans were taken at the peak dust continuum position of nearby starless cores CB244 (23:25:27.1, +74:18:25.3, J2000.0) and Seo09 (04:18:07, +28:05:13, J2000.0; Seo et al. 2015) to monitor any changes in flux. In Fig. A1 the amplitudes (Ta* in units of Kelvin) of the brightest CH₃OH $2_{0,2} - 1_{0,1}$ A transition are plotted versus time, spanning from 2021 to the last observation date in 2023. The data collected for each session was baselined and hanning smoothed by 2 channels before the amplitude was measured with a Gaussian fit. Fig. A1 shows that the change in flux for each standard source did not vary by more than 10 per cent.

To convert to the main beam temperature scale, where $T_{\rm mb}=T_A^*/\eta$ (Mangum 1993), different η values were calculated for each observing season. During the fall of 2021 we used $\eta_{\rm ARO1}=84.25\pm0.73$ per cent and $\eta_{\rm ARO2}=85.40\pm0.48$ per cent by taking the median measurements from Jupiter, Uranus, and Venus. During the Spring of 2022 we used $\eta_{\rm ARO1}=86.60\pm1.36$ per cent and $\eta_{\rm ARO2}=87.96\pm1.53$ per cent by taking the median measurements from Jupiter, Mars, and Uranus. And, in the Spring of 2023 we used $\eta_{\rm ARO1}=80.02\pm0.50$ per cent and $\eta_{\rm ARO2}=89.09\pm0.59$ per cent by taking the median measurements from Mars and Venus.

As for our spectrometer setup with the AROWS backend, we tuned simultaneously to four lines: the $2_{0.2} - 1_{0.1}$ E transition of CH₃OH at 96.74455 GHz, the centre of the two $5_{0.4} - 4_{0.4}$ transition of

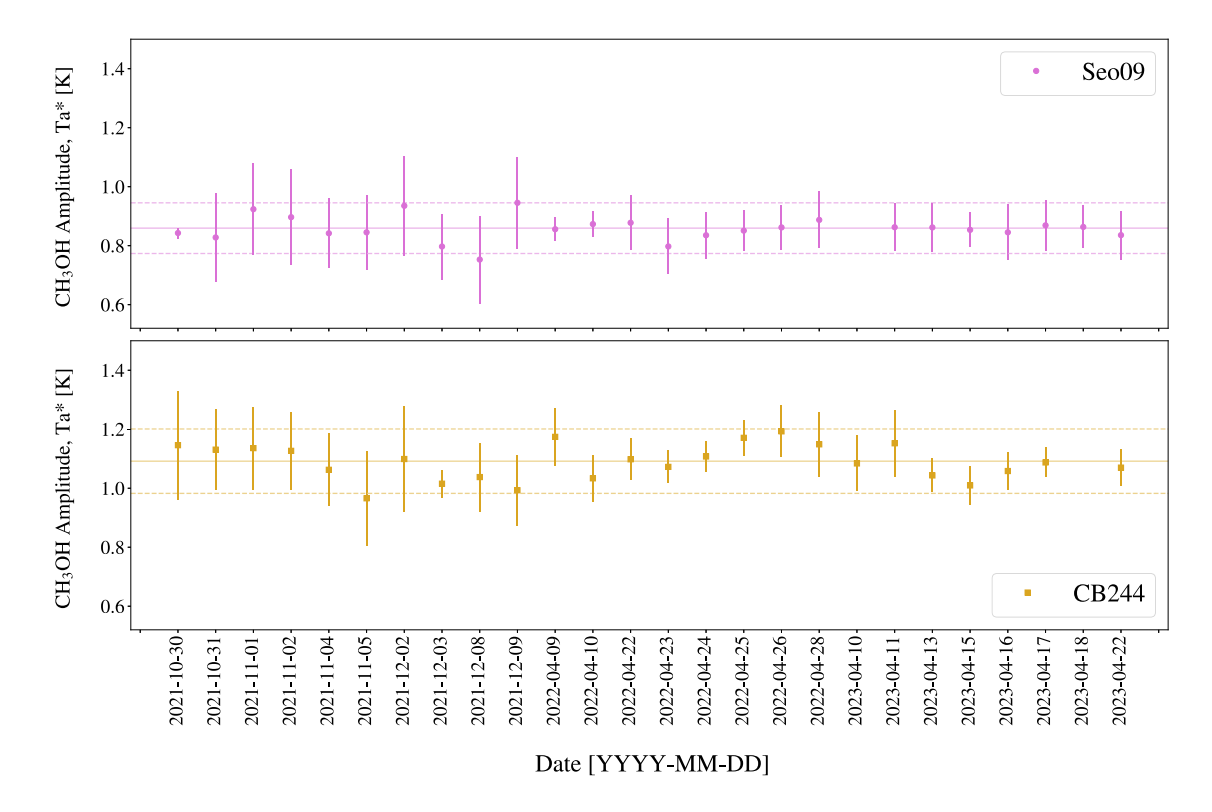


Figure A1. Standard sources Seo09 and CB244 were monitored during ARO 12m observations from 2021 to 2023. We plot the Gaussian fitted amplitude for the brightest CH₃OH $2_{0.2} - 1_{0.1}$ A transition (errorbars $3\sigma_{rms}$) versus the date observed. The amplitudes do not vary by more than ± 10 per cent from the mean (dashed horizontal lines).

CH₃CHO at 95.9554 GHz, the $10_{1.9} - 9_{1.8}$ transition of CH₂CHCN at 96.982446 GHz, and the $10_{0.10} - 9_{0.9}$ transition of CH₂CHCN at 94.276641 GHz (see Table 2). The FWHM beam sizes are therefore between ~ 62 and 64 arcsec. This setup was achieved with the AROWS multiwindow mode where each line was placed in four separate spectral windows within 4 GHz either in the lower side band (LSB), as was done during 2022 Spring observations, or in the upper side band (USB), as was done during fall 2021 and 2023 Spring observations. Note that the 2022 Spring observations were done in this different sideband configuration in order to get rid of standing waves present in the USB at the time.

The non-detected vinyl cyanide, CH_2CHCN , lines are plotted in Fig. A2. Both the $10_{0,10}-9_{0,9}$ and $10_{1,9}-9_{1,8}$ lines at 94.27 and 96.98 GHz, respectively, are shown with the 94.27 GHz line shifted up by $100\,\text{mK}$ for easier viewing. For core 54, the vertical polarization was corrupted in the two CH_2CHCN windows, likely due to a standing wave interference, and therefore the noise level is higher.

In Table A1 we list the Gaussian fit line parameters, as well as the RMS values, calculated using the CLASS software and found for all of the ARO 12 m spectral data towards each of the 35 cores. Line velocities have been re-shifted to the corresponding rest frequencies.

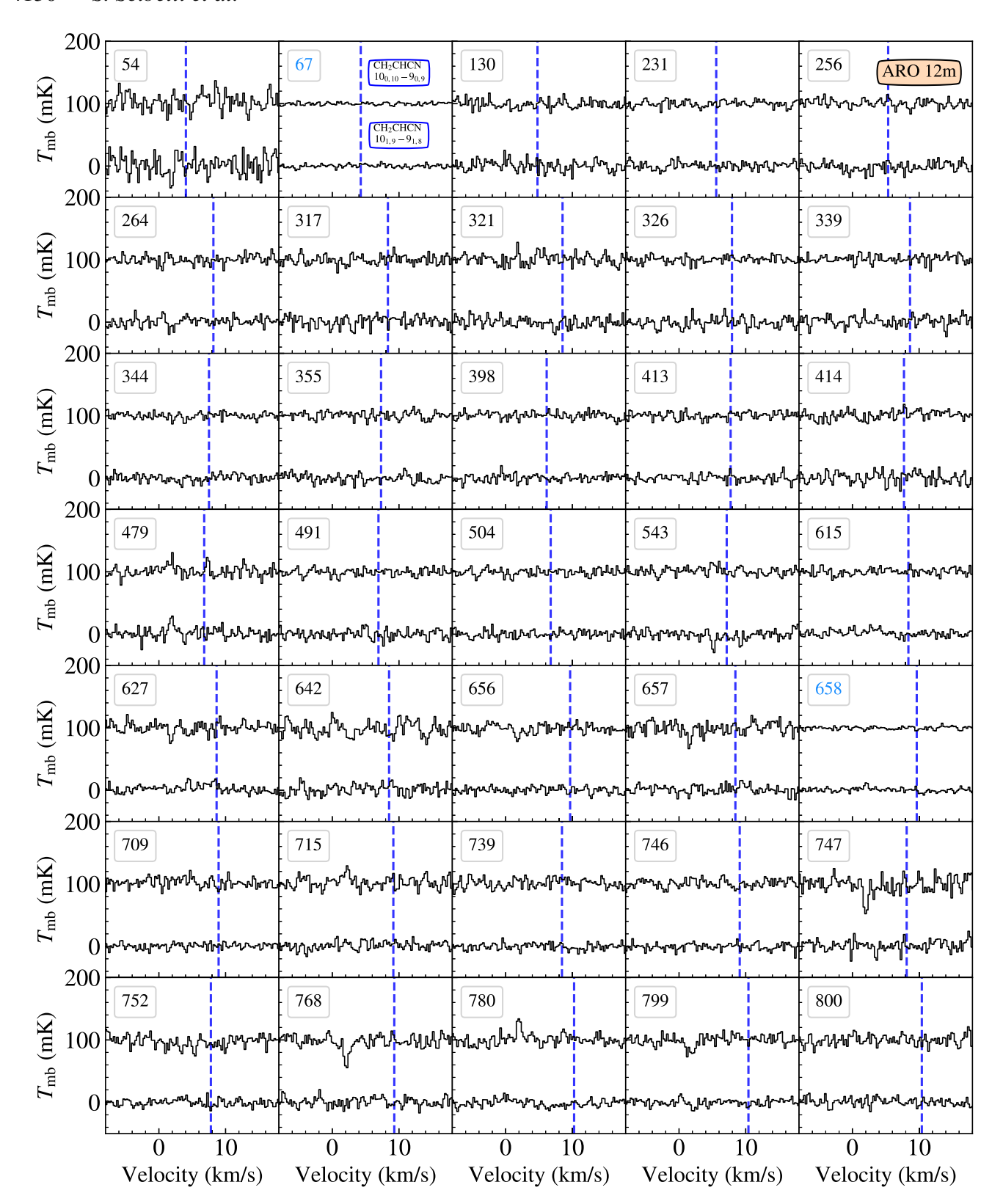


Figure A2. Non-detections of vinyl cyanide, CH₂CHCN, the 94 and 96 GHz line spectrum (in black) in units of $T_{\rm mb}$ (K) versus velocity (km s⁻¹) from the ARO 12 m for each of the 35 starless and pre-stellar cores targeted in this Perseus survey. Core numbers are labelled in the upper left of each panel. Longer integration time on cores 67 and 658 (also labelled in blue), resulted in RMS values around $\sigma_{T_{\rm mb}} = 2 - 3$ mK. For the remaining cores, the average RMS value is $\sigma_{T_{\rm mb}} = 6 - 7$ mK. The $10_{0,10} - 9_{0,9}$ line at 94GHz is shifted by 100 mK for easier viewing. A vertical dashed line (blue) is overlaid on each panel to show the v_{lsr} found from the brightest ARO 12m methanol line.

Table A1. ARO 12m line parameters.

Core	Line	Area (K-km s ⁻¹)	Vel	FWHM (km s ⁻¹)	$T_{ m mb}$ (K)	RMS (K)
54	CH ₃ OH 2 _{0,2} – 1 _{0,1} E	0.026(0.003)	5.009(0.026)	0.397(0.049)	0.061	0.0067
	$CH_3OH 2_{0,2} - 1_{0,1} A$	0.233(0.004)	4.049(0.006)	0.724(0.016)	0.302	0.0067
	$CH_3OH 2_{-1,2} - 1_{-1,1} E$	0.168(0.004)	4.048(0.009)	0.727(0.024)	0.217	0.0067
	$CH_3CHO\ 5_{0,5} - 4_{0,4}\ A$	-	-	-	-	0.0053
	$CH_3CHO\ 5_{0,5} - 4_{0,4}\ E$	_	_	_	_	0.0053
	$CH_2CHCN\ 10_{0,10} - 9_{0,9}$	-	-	-	-	0.0131
	$CH_2CHCN\ 10_{1,9} - 9_{1,8}$	-	-	-	-	0.0150
67*	$CH_3OH 2_{0,2} - 1_{0,1} E$	0.0095(0.002)	4.381(0.034)	0.463(0.096)	0.0193	0.0029
	$CH_3OH\ 2_{0,2} - 1_{0,1}\ A$	0.24701(0.002)	4.508(0.003)	0.747(0.006)	0.3106	0.0029
	$CH_3OH 2_{-1,2} - 1_{-1,1} E$	0.18519(0.002)	4.496(0.004)	0.734(0.009)	0.2370	0.0029
	$CH_3CHO\ 5_{0,5} - 4_{0,4}\ A$	0.0064(0.001)	4.398(0.082)	0.730(0.152)	0.0083	0.0023
	$CH_3CHO\ 5_{0,5} - 4_{0,4} E$	_	_	_	_	0.0023
	$CH_2CHCN 10_{0,10} - 9_{0,9}$	_	_	_	_	0.0023
130	$CH_2CHCN 10_{1,9} - 9_{1,8}$	_	_	_	_	0.0027 0.0079
130	CH ₃ OH $2_{0,2} - 1_{0,1}$ E CH ₃ OH $2_{0,2} - 1_{0,1}$ A	0.181(0.004)	4.772(0.006)	0.531(0.014)	0.319	0.0079
	CH ₃ OH $2_{0,2} - 1_{0,1}$ A CH ₃ OH $2_{-1,2} - 1_{-1,1}$ E	0.142(0.004)	4.772(0.000)	0.555(0.014)	0.241	0.0079
	CH ₃ CHO $5_{0,5} - 4_{0,4}$ A	0.142(0.004)	4.738(0.008)	0.555(0.02)	0.241	0.0079
	CH ₃ CHO $5_{0.5} - 4_{0.4}$ E	_	_	_	_	0.0064
	$CH_2CHCN 10_{0,10} - 9_{0,9}$	_	_	_	_	0.0064
	$CH_2CHCN 10_{1,9} - 9_{1,8}$	_	_	_	_	0.0077
231	CH ₃ OH $2_{0,2} - 1_{0,1}$ E	_	_	_	_	0.0064
	$CH_3OH 2_{0,2} - 1_{0,1} A$	0.204(0.003)	5.578(0.004)	0.458(0.009)	0.418	0.0064
	$CH_3OH \ 2_{-1,2} - 1_{-1,1} \ E$	0.146(0.003)	5.571(0.005)	0.429(0.009)	0.32	0.0064
	CH ₃ CHO $5_{0,5} - 4_{0,4}$ A	-	-	-	_	0.0047
	CH ₃ CHO $5_{0.5} - 4_{0.4}$ E	_	_	_	_	0.0047
	$CH_2CHCN 10_{0,10} - 9_{0,9}$	_	_	_	_	0.0052
	$CH_2CHCN\ 10_{1,9} - 9_{1,8}$	_	_	_	_	0.0061
256	$CH_3OH 2_{0,2} - 1_{0,1} E$	_	_	_	0.389 0.296 - -	0.0076
	$CH_3OH\ 2_{0,2} - 1_{0,1}\ A$	0.208(0.004)	5.361(0.005)	0.502(0.012)		0.0076
	$CH_3OH\ 2_{-1,2} - 1_{-1,1} E$	0.163(0.004)	5.352(0.007)	0.518(0.016)		0.0076
	$CH_3CHO\ 5_{0,5} - 4_{0,4}\ A$	_	-	_		0.0062
	$CH_3CHO\ 5_{0,5} - 4_{0,4}\ E$	_	-	_	-	0.0062
	$CH_2CHCN\ 10_{0,10} - 9_{0,9}$	-	-	-	-	0.0053
	$CH_2CHCN\ 10_{1,9} - 9_{1,8}$	-	-	-	-	0.0071
264	$CH_3OH\ 2_{0,2} - 1_{0,1} E$	0.0765(0.007)	7.969(0.053)	1.193(0.113)		0.0085
	$CH_3OH\ 2_{0,2} - 1_{0,1}\ A$	0.623(0.007)	8.162(0.004)	0.947(0.012)		0.0085
	$CH_3OH 2_{-1,2} - 1_{-1,1} E$	0.423(0.006)	8.139(0.006)	0.853(0.015)		0.0085
	$CH_3CHO\ 5_{(0,5)} - 4_{(0,4)}\ A$	0.015(0.004)	8.120(0.06)	0.507(0.163)		0.0066
	$CH_3CHO\ 5_{(0,5)} - 4_{(0,4)}\ E$	0.0144(0.003)	7.979(0.053)	0.462(0.144)	0.296 - - - 0.0627 0.617 0.466 0.0277 0.0292	0.0066
	$CH_2CHCN 10_{0,10} - 9_{0,9}$	_	-	_	-	0.0065
17	$CH_2CHCN \ 10_{1,9} - 9_{1,8}$	0.1(((0.007)	9.292(0.002)	0.771(0.020)	- 0.202	0.0068
317	$CH_3OH 2_{0,2} - 1_{0,1} E$	0.166(0.007)	8.383(0.002)	0.771(0.039)	0.202	0.0098 0.0098
	CH ₃ OH $2_{0,2} - 1_{0,1}$ A CH ₃ OH $2_{-1,2} - 1_{-1,1}$ E	1.07(0.008) 0.797(0.008)	8.343(0.003) 8.340(0.002)	0.885(0.008) 0.887(0.01)	1.14 0.845	0.0098
	CH ₃ CHO $5_{0.5} - 4_{0.4}$ A	0.0599(0.005)	8.388(0.034)	0.835(0.086)	0.0674	0.0098
	CH ₃ CHO $5_{0.5} - 4_{0.4}$ A CH ₃ CHO $5_{0.5} - 4_{0.4}$ E	0.0617(0.006)	8.301(0.048)	1.04(0.124)	0.0557	0.0073
	$CH_3CHO 3_{0,3} = 4_{0,4} E$ $CH_2CHCN 10_{0.10} = 9_{0.9}$	0.0017(0.000)	0.301(0.040)	1.04(0.124)	-	0.0073
	$CH_2CHCN 10_{1,9} - 9_{1,8}$	_	_	_	_	0.0073
321	CH ₃ OH $2_{0.2} - 1_{0.1}$ E	0.198(0.055)	8.523(0.242)	0.819(0.242)	0.227	0.0080
	CH ₃ OH $2_{0,2} - 1_{0,1}$ A	1.55(0.055)	8.530(0.242)	1.01(0.242)	1.44	0.0080
	CH ₃ OH $2_{-1,2} - 1_{-1,1}$ E	1.11(0.055)	8.519(0.242)	0.966(0.242)	1.08	0.0080
	CH ₃ CHO $5_{0.5} - 4_{0.4}$ A	0.0599(0.005)	8.505(0.034)	0.835(0.086)	0.0674	0.0073
	CH ₃ CHO $5_{0,5} - 4_{0,4}$ E	0.0617(0.006)	8.528(0.048)	1.04(0.124)	0.0557	0.0073
	$CH_2CHCN\ 10_{0,10} - 9_{0,9}$			_ ′	_	0.0080
	$CH_2CHCN\ 10_{1,9} - 9_{1,8}$	_	_	_	_	0.0077
326	CH ₃ OH $2_{0,2} - 1_{0,1}$ E	0.399(0.096)	7.885(0.242)	1.4(0.242)	0.267	0.0104
	$CH_3OH 2_{0,2} - 1_{0,1} A$	3.05(0.096)	7.941(0.242)	1.37(0.242)	2.1	0.0104
	$CH_3OH 2_{-1,2} - 1_{-1,1} E$	2.32(0.096)	7.932(0.242)	1.36(0.242)	1.6	0.0104
	$CH_3CHO\ 5_{0,5} - 4_{0,4}\ A$	0.0885(0.005)	7.917(0.037)	1.45(0.09)	0.0574	0.0052
	CH ₃ CHO $5_{0,5} - 4_{0,4}$ E	0.0805(0.003)	7.826(0.033)	1.24(0.06)	0.061	0.0052
	$CH_2CHCN\ 10_{0,10} - 9_{0,9}$		_	_	_	0.0055
	$CH_2CHCN\ 10_{1.9} - 9_{1.8}$	_			_	0.0076

Table A1 - continued

Core	Line	Area (K-km s ⁻¹)	Vel (km s ⁻¹)	FWHM (km s ⁻¹)	$T_{ m mb}$ (K)	RMS (K)
339	CH ₃ OH 2 _{0.2} – 1 _{0.1} E	0.109(0.008)	8.568(0.037)	1.08(0.091)	0.095	0.009
	$CH_3OH\ 2_{0,2} - 1_{0,1}\ A$	0.759(0.007)	8.638(0.005)	1.04(0.011)	0.683	0.009
	$CH_3OH 2_{-1,2} - 1_{-1,1} E$	0.549(0.007)	8.621(0.007)	1.05(0.017)	0.491	0.009
	$CH_3CHO\ 5_{0,5} - 4_{0,4}\ A$	-	-	-	-	0.006
	$CH_3CHO\ 5_{0,5} - 4_{0,4}\ E$	-	-	-	_	0.006
	$CH_2CHCN\ 10_{0,10} - 9_{0,9}$	-	-	-	-	0.006
	$CH_2CHCN\ 10_{1,9} - 9_{1,8}$	-	_	_	_	0.007
44	$CH_3OH\ 2_{0,2} - 1_{0,1} E$	0.0146(0.003)	7.543(0.059)	0.526(0.113)	0.0262	0.006
	$CH_3OH\ 2_{0,2} - 1_{0,1}\ A$	0.157(0.004)	7.510(0.012)	0.822(0.025)	0.179	0.006
	$CH_3OH 2_{-1,2} - 1_{-1,1} E$	0.109(0.004)	7.459(0.015)	0.793(0.033)	0.129	0.006
	CH ₃ CHO $5_{0,5} - 4_{0,4}$ A	-	-	-	_	0.004
	CH ₃ CHO $5_{0,5} - 4_{0,4}$ E CH ₂ CHCN $10_{0,10} - 9_{0,9}$	_	_	_	_	0.004 0.004
	$CH_2CHCN 10_{0,10} - 9_{0,9}$ $CH_2CHCN 10_{1,9} - 9_{1,8}$	_	_	_	_	0.004
55	CH ₂ CHCN $10_{1,9} - 9_{1,8}$ CH ₃ OH $2_{0,2} - 1_{0,1}$ E	0.0285(0.003)	7.314(0.006)	0.402(0.062)	0.0666	0.003
33	$CH_3OH 2_{0,2} - I_{0,1} E$ $CH_3OH 2_{0,2} - I_{0,1} A$	0.286(0.001)	7.314(0.003)	0.485(0.005)	0.553	0.006
	CH ₃ OH $2_{-1.2} - 1_{-1.1}$ E	0.207(0.003)	7.305(0.003)	0.478(0.009)	0.407	0.006
	CH ₃ CHO $5_{0,5} - 4_{0,4}$ A	-	-	-	-	0.005
	CH ₃ CHO $5_{0.5} - 4_{0.4}$ E	_	_	_	_	0.005
	CH ₂ CHCN $10_{0,10} - 9_{0,9}$	_	_	_	_	0.005
	$CH_2CHCN 10_{1.9} - 9_{1.8}$	_	_	_	_	0.006
98	$CH_3OH 2_{0,2} - 1_{0,1} E$	_	_	_	_	0.006
	$CH_3OH \ 2_{0,2} - 1_{0,1} \ A$	0.0557(0.003)	6.150(0.014)	0.496(0.037)	0.106	0.006
	$CH_3OH \ 2_{-1,2} - 1_{-1,1} E$	0.0351(0.003)	6.143(0.02)	0.461(0.051)	0.0715	0.006
	$CH_3CHO\ 5_{0,5} - 4_{0,4}\ A$	_	_	_	_	0.005
	CH ₃ CHO $5_{0,5} - 4_{0,4}$ E	_	_	_	_	0.005
	$CH_2CHCN\ 10_{0,10} - 9_{0,9}$	-	-	-	_	0.005
	$CH_2CHCN\ 10_{1,9} - 9_{1,8}$	-	-	-	_	0.005
3	$CH_3OH 2_{0,2} - 1_{0,1} E$	0.0179(0.003)	7.767(0.037)	0.439(0.081)	0.0383	0.006
	$CH_3OH\ 2_{0,2} - 1_{0,1}\ A$	0.300(0.004)	7.738(0.004)	0.661(0.01)	0.426	0.006
	$CH_3OH 2_{-1,2} - 1_{-1,1} E$	0.225(0.004)	7.708(0.001)	0.669(0.015)	0.426 0.316 0.022	0.006
	$CH_3CHO\ 5_{0,5} - 4_{0,4}\ A$	0.012(0.003)	7.722(0.062)	0.511(0.128)	0.022	0.005
	$CH_3CHO\ 5_{0,5} - 4_{0,4} E$	-	_	_	_	0.005
	$CH_2CHCN 10_{0,10} - 9_{0,9}$	-	-	-	-	0.005
	$CH_2CHCN 10_{1,9} - 9_{1,8}$	-	-	-	_	0.005
14	$CH_3OH\ 2_{0,2} - 1_{0,1} E$	0.0755(0.004)	7.721(0.01)	0.422(0.022)	- 0.164	0.007
	CH ₃ OH $2_{0,2} - 1_{0,1}$ A CH ₃ OH $2_{-1,2} - 1_{-1,1}$ E	0.0755(0.004)	7.731(0.01)	0.433(0.023)	0.164	0.007
	,,-	0.0463(0.003)	7.723(0.01)	0.321(0.061)	0.136	0.007 0.006
	CH ₃ CHO $5_{0,5} - 4_{0,4}$ A CH ₃ CHO $5_{0,5} - 4_{0,4}$ E	-	-	-	_	0.006
	CH ₂ CHCN $10_{0,10} - 9_{0,9}$	_	_	_	_	0.006
	$CH_2CHCN 10_{0,10} - 9_{0,9}$ $CH_2CHCN 10_{1,9} - 9_{1,8}$	_	_	_	_	0.007
79	CH ₃ OH $2_{0.2} - 1_{0.1}$ E	_	_	_	_	0.010
	CH ₃ OH $2_{0,2} - 1_{0,1}$ A	0.522(0.007)	6.792(0.005)	0.753(0.012)	0.651	0.010
	CH ₃ OH $2_{-1,2} - 1_{-1,1}$ E	0.391(0.007)	6.785(0.007)	0.743(0.016)	0.494	0.010
	$CH_3CHO 5_{0.5} - 4_{0.4} A$	_	_	_	_	0.007
	CH ₃ CHO $5_{0.5} - 4_{0.4}$ E	_	_	_	_	0.007
	$CH_2CHCN\ 10_{0,10} - 9_{0,9}$	_	_	_	_	0.008
	$CH_2CHCN\ 10_{1,9} - 9_{1,8}$	_	_	_	_	0.008
91	$CH_3OH 2_{0,2} - 1_{0,1} E$	_	_	_	_	0.007
	$CH_3OH\ 2_{0,2} - 1_{0,1}\ A$	0.131(0.005)	6.926(0.011)	0.646(0.028)	0.191	0.007
	$CH_3OH \ 2_{-1,2} - 1_{-1,1} \ E$	0.0953(0.005)	6.931(0.016)	0.667(0.043)	0.134	0.007
	$CH_3CHO\ 5_{0,5} - 4_{0,4}\ A$	_	_	_	_	0.003
	CH ₃ CHO $5_{0,5} - 4_{0,4}$ E	-	-	-	_	0.00
	$CH_2CHCN 10_{0,10} - 9_{0,9}$	-	-	-	-	0.005
	$CH_2CHCN\ 10_{1,9} - 9_{1,8}$	_	_	_	_	0.000
14	$CH_3OH 2_{0,2} - 1_{0,1} E$	0.0332(0.005)	6.778(0.03)	0.459(0.075)	0.068	0.000
	$CH_3OH 2_{0,2} - 1_{0,1} A$	0.446(0.006)	6.756(0.003)	0.591(0.009)	0.709	0.000
	$CH_3OH 2_{-1,2} - 1_{-1,1} E$	0.333(0.006)	6.748(0.005)	0.598(0.013)	0.524	0.006
	$CH_3CHO 5_{0,5} - 4_{0,4} A$	0.00005(0.000)	- (762(0.051)	- 0.220(0.004)	- 0.0201	0.005
	CH ₃ CHO $5_{0,5} - 4_{0,4}$ E	0.00985(0.002)	6.763(0.051)	0.329(0.094)	0.0281	0.005
	$CH_2CHCN 10_{0,10} - 9_{0,9}$	-	-	-	_	0.005
	$CH_2CHCN\ 10_{1,9} - 9_{1,8}$	_	_	_	_	0.005

Table A1 - continued

Core	Line	Area (K-km s ⁻¹)	Vel $(km s^{-1})$	FWHM (km s ⁻¹)	$T_{ m mb}$ (K)	RMS (K)
	CH OHA 1 F	(,	((
543	CH ₃ OH $2_{0,2} - 1_{0,1}$ E CH ₃ OH $2_{0,2} - 1_{0,1}$ A	0.156(0.004)	7.149(0.007)	0.513(0.017)	0.287	0.0076 0.0076
	$CH_3OH 2_{-1,2} - 1_{-1,1} E$	0.130(0.004)	7.149(0.007)	0.515(0.017)	0.21	0.0076
	CH ₃ CHO $5_{0,5} - 4_{0,4}$ A	0.115(0.004)	7.132(0.005)	0.300(0.022)	-	0.0070
	CH ₃ CHO $5_{0.5} - 4_{0.4}$ E	_	_	_	_	0.0061
	$CH_2CHCN 10_{0.10} - 9_{0.9}$	_	_	_	_	0.0062
	$CH_2CHCN\ 10_{1.9} - 9_{1.8}$	_	_	_	_	0.0063
615	$CH_3OH 2_{0,2} - 1_{0,1} E$	0.0244(0.018)	8.352(0.242)	0.554(0.242)	0.0414	0.0052
	$CH_3OH 2_{0,2} - 1_{0,1} A$	0.352(0.018)	8.394(0.242)	0.539(0.242)	0.613	0.0052
	$CH_3OH 2_{-1,2} - 1_{-1,1} E$	0.267(0.018)	8.379(0.242)	0.569(0.242)	0.44	0.0052
	$CH_3CHO\ 5_{0,5} - 4_{0,4}\ A$	0.0124(0.003)	8.308(0.063)	0.602(0.176)	0.0194	0.0045
	$CH_3CHO\ 5_{0,5}-4_{0,4}\ E$	0.0106(0.002)	8.110(0.041)	0.379(0.066)	0.0263	0.0045
	$CH_2CHCN\ 10_{0,10} - 9_{0,9}$	-	-	-	_	0.0052
	$CH_2CHCN\ 10_{1,9} - 9_{1,8}$	_	_	_	_	0.0049
627	$CH_3OH 2_{0,2} - 1_{0,1} E$	0.0269(0.007)	8.654(0.052)	0.49(0.171)	0.0516	0.0056
	$CH_3OH\ 2_{0,2} - 1_{0,1}\ A$	0.23(0.005)	8.653(0.005)	0.421(0.011)	0.513	0.0056
	$CH_3OH 2_{-1,2} - 1_{-1,1} E$	0.162(0.005)	8.645(0.006)	0.393(0.012)	0.387	0.0056
	$CH_3CHO\ 5_{0,5} - 4_{0,4}\ A$	0.0124(0.003)	8.551(0.057)	0.494(0.126)	0.0236	0.0054
	$CH_3CHO\ 5_{0,5} - 4_{0,4} E$	0.0172(0.003)	8.372(0.077)	0.686(0.162)	0.0235	0.0054
	$CH_2CHCN 10_{0,10} - 9_{0,9}$	_	_	_	_	0.0075
640	$CH_2CHCN 10_{1,9} - 9_{1,8}$	_	_	_	_	0.0044
642	$CH_3OH 2_{0,2} - 1_{0,1} E$	0.0521(0.002)	9 519(0 012)	0.41(0.026)	0.110	0.0069
	CH ₃ OH $2_{0,2} - 1_{0,1}$ A CH ₃ OH $2_{-1,2} - 1_{-1,1}$ E	0.0521(0.003) 0.0406(0.003)	8.518(0.012) 8.488(0.018)	0.41(0.036) 0.432(0.041)	0.119	0.0069
	CH ₃ CHO $5_{0,5} - 4_{0,4}$ A	0.0400(0.003)	0.400(0.010)	0.432(0.041)	0.0883	0.0069 0.0072
	CH ₃ CHO $5_{0.5} - 4_{0.4}$ E				0.0072	
	$CH_2CHCN 10_{0.10} - 9_{0.9}$	_	_	_	_	0.0072
	$CH_2CHCN 10_{1,9} - 9_{1,8}$	_	_	_	_	0.0078
556	CH ₃ OH $2_{0.2} - 1_{0.1}$ E	0.012(0.011)	9.661(0.242)	0.3(0.242)	0.0377 0.409 0.32	0.0054
	$CH_3OH\ 2_{0,2} - 1_{0,1}\ A$	0.168(0.011)	9.669(0.242)	0.386(0.242)		0.0054
	$CH_3OH 2_{-1,2} - 1_{-1,1} E$	0.124(0.011)	9.664(0.242)	0.364(0.242)		0.0054
	CH ₃ CHO $5_{0.5} - 4_{0.4}$ A			_ ′		0.0049
	$CH_3CHO\ 5_{0,5} - 4_{0,4}\ E$	_	_	_	_	0.0049
	$CH_2CHCN\ 10_{0,10} - 9_{0,9}$	_	_	_	_	0.0068
	$CH_2CHCN\ 10_{1,9} - 9_{1,8}$	-	-	-	-	0.0048
657	$CH_3OH\ 2_{0,2} - 1_{0,1} E$	_	-	-	_	0.0073
	$CH_3OH\ 2_{0,2} - 1_{0,1}\ A$	0.127(0.004)	8.451(0.007)	0.497(0.019)	0.239	0.0073
	$CH_3OH \ 2_{-1,2} - 1_{-1,1} \ E$	0.0903(0.004)	8.462(0.011)	0.5(0.029)	0.17	0.0073
	$CH_3CHO\ 5_{0,5} - 4_{0,4}\ A$	_	_	-	_	0.0064
	$CH_3CHO\ 5_{0,5} - 4_{0,4}\ E$	_	_	-	_	0.0064
	$CH_2CHCN\ 10_{0,10} - 9_{0,9}$	_	_	_	_	0.0097
	$CH_2CHCN\ 10_{1,9} - 9_{1,8}$	-	-	_	_	0.0065
658*	$CH_3OH\ 2_{0,2} - 1_{0,1} E$	0.0257(0.016)	9.656(0.242)	0.441(0.242)	0.0547	0.0038
	$CH_3OH\ 2_{0,2} - 1_{0,1}\ A$	0.2792(0.016)	9.712(0.242)	0.407(0.242)	0.6451	0.0038
	$CH_3OH 2_{-1,2} - 1_{-1,1} E$	0.2049(0.016)	9.704(0.242)	0.399(0.242)	0.4821	0.0038
	CH ₃ CHO 5 _{0,5} - 4 _{0,4} A CH ₃ CHO 5 _{0,5} - 4 _{0,4} E	0.0056(0.001) 0.0074(0.001)	9.533(0.036) 9.494(0.041)	0.389(0.151) 0.463(0.102)	0.0134 0.0149	0.0025 0.0025
	CH ₃ CHO $3_{0,5} - 4_{0,4}$ E CH ₂ CHCN $10_{0,10} - 9_{0,9}$	0.0074(0.001)	9.494(0.041)	0.403(0.102)	0.0149	0.0023
	CH ₂ CHCN $10_{0,10} - 9_{0,9}$ CH ₂ CHCN $10_{1,9} - 9_{1,8}$	_	_	_	_	0.0028
709	CH ₃ OH $2_{0.2} - 1_{0.1}$ E	0.0913(0.004)	8.903(0.013)	0.694(0.031)	0.124	0.0028
, 0)	$CH_3OH 2_{0,2} - 1_{0,1} A$	0.661(0.004)	8.954(0.002)	0.841(0.006)	0.739	0.0059
	CH ₃ OH $2_{-1,2} - 1_{-1,1}$ E	0.464(0.004)	8.938(0.003)	0.827(0.008)	0.527	0.0059
	CH ₃ CHO $5_{0,5} - 4_{0,4}$ A	0.0353(0.004)	8.919(0.044)	0.826(0.098)	0.0401	0.0080
	CH ₃ CHO $5_{0,5} - 4_{0,4}$ E	0.0433(0.004)	8.771(0.041)	0.89(0.086)	0.0457	0.0080
	$CH_2CHCN 10_{0,10} - 9_{0,9}$			_ ′	_	0.0069
	$CH_2CHCN\ 10_{1,9} - 9_{1,8}$	_	_	_	_	0.0048
715	$CH_3OH 2_{0,2} - 1_{0,1} E$	0.0265(0.015)	9.068(0.242)	0.713(0.242)	0.0349	0.0059
	$CH_3OH\ 2_{0,2}-1_{0,1}\ A$	0.328(0.015)	9.158(0.242)	0.655(0.242)	0.47	0.0059
	$CH_3OH \ 2_{-1,2} - 1_{-1,1} \ E$	0.24(0.015)	9.146(0.242)	0.672(0.242)	0.335	0.0064
	$CH_3CHO\ 5_{0,5} - 4_{0,4}\ A$	0.0106(0.003)	9.152(0.075)	0.521(0.172)	0.0191	0.0054
	$CH_3CHO\ 5_{0,5} - 4_{0,4}\ E$	0.00776(0.003)	9.159(0.056)	0.366(0.253)	0.0199	0.0054
	$CH_2CHCN\ 10_{0,10} - 9_{0,9}$	-	-	_	_	0.0069
	$CH_2CHCN\ 10_{1.9} - 9_{1.8}$					0.0048

Table A1 - continued

Core	Line	Area	Vel	FWHM	$T_{ m mb}$	RMS
		$(K-km s^{-1})$	$(km s^{-1})$	(km s^{-1})	(K)	(K)
39	$CH_3OH 2_{0,2} - 1_{0,1} E$	_	_	_	_	0.0066
	$CH_3OH \ 2_{0.2} - 1_{0.1} \ A$	0.25(0.004)	8.443(0.005)	0.621(0.013)	0.379	0.0066
	$CH_3OH 2_{-1,2} - 1_{-1,1} E$	0.18(0.004)	8.439(0.008)	0.622(0.019)	0.271	0.0066
	$CH_3CHO 5_{0.5} - 4_{0.4} A$	_	<u>-</u>	_	_	0.0058
	CH ₃ CHO $5_{0.5} - 4_{0.4}$ E	_	_	_	_	0.0058
	$CH_2CHCN 10_{0.10} - 9_{0.9}$	_	_	_	_	0.0070
	$CH_2CHCN 10_{1.9} - 9_{1.8}$	_	_	_	_	0.0051
46	$CH_3OH 2_{0,2} - 1_{0,1} E$	0.0249(0.003)	9.117(0.035)	0.552(0.092)	0.0424	0.0058
	$CH_3OH 2_{0.2} - 1_{0.1} A$	0.447(0.004)	9.100(0.003)	0.65(0.006)	0.646	0.0058
	$CH_3OH 2_{-1,2} - 1_{-1,1} E$	0.332(0.004)	9.091(0.003)	0.647(0.008)	0.483	0.0058
	$CH_3CHO 5_{0.5} - 4_{0.4} A$	0.0252(0.003)	8.812(0.072)	0.966(0.128)	0.0245	0.0051
	CH ₃ CHO $5_{0.5} - 4_{0.4}$ E	0.0207(0.004)	8.894(0.053)	0.699(0.162)	0.0278	0.0051
	$CH_2CHCN 10_{0.10} - 9_{0.9}$	_	_	_	_	0.0074
	$CH_2CHCN\ 10_{1,9} - 9_{1,8}$	_	_	_	_	0.0054
47	$CH_3OH 2_{0,2} - 1_{0,1} E$	0.0423(0.004)	8.177(0.032)	0.528(0.078)	0.0752	0.0083
	$CH_3OH 2_{0.2} - 1_{0.1} A$	0.346(0.005)	8.137(0.004)	0.527(0.008)	0.618	0.0083
	$CH_3OH 2_{-1,2} - 1_{-1,1} E$	0.241(0.005)	8.125(0.005)	0.523(0.012)	0.432	0.0083
	CH ₃ CHO $5_{0.5} - 4_{0.4}$ A	_ ′	_ ′		_	0.0074
	CH ₃ CHO $5_{0.5} - 4_{0.4}$ E	_	_	_	_	0.0074
	$CH_2CHCN 10_{0.10} - 9_{0.9}$	_	_	_	_	0.0131
	$CH_2CHCN\ 10_{1,9} - 9_{1,8}$	_	_	_	_	0.0078
52	$CH_3OH 2_{0,2} - 1_{0,1} E$	0.0589(0.003)	7.793(0.016)	0.536(0.036)	0.103	0.0064
	$CH_3OH 2_{0.2} - 1_{0.1} A$	0.558(0.004)	7.793(0.002)	0.677(0.006)	0.774	0.0064
	$CH_3OH \ 2_{-1,2} - 1_{-1,1} E$	0.408(0.004)	7.786(0.003)	0.669(0.008)	0.573	0.0064
	CH ₃ CHO $5_{0.5} - 4_{0.4}$ A	0.0229(0.004)	7.778(0.086)	0.92(0.23)	0.0234	0.0054
	CH ₃ CHO $5_{0,5} - 4_{0,4}$ E	0.023(0.003)	7.825(0.060)	0.771(0.129)	0.0281	0.0054
	$CH_2CHCN\ 10_{0,10} - 9_{0,9}$				_	0.0091
	$CH_2CHCN\ 10_{1.9} - 9_{1.8}$	_	_	_	_	0.0049
68	$CH_3OH 2_{0,2} - 1_{0,1} E$	0.0179(0.004)	9.327(0.037)	0.424(0.11)	0.0397	0.0064
	$CH_3OH 2_{0.2} - 1_{0.1} A$	0.308(0.004)	9.296(0.004)	0.684(0.012)	0.424	0.0064
	$CH_3OH 2_{-1,2} - 1_{-1,1} E$	0.226(0.004)	9.279(0.007)	0.706(0.017)	0.3	0.0064
	$CH_3CHO\ 5_{0,5} - 4_{0,4}\ A$	0.025(0.005)	9.132(0.100)	1(0.277)	0.0235	0.0073
	$CH_3CHO\ 5_{0.5} - 4_{0.4}\ E$	0.0117(0.005)	8.947(0.091)	0.559(0.373)	0.0196	0.0073
	$CH_2CHCN\ 10_{0.10} - 9_{0.9}$	_	_	_	_	0.0100
	$CH_2CHCN\ 10_{1,9} - 9_{1,8}$	_	_	_	_	0.0069
'80	$CH_3OH 2_{0,2} - 1_{0,1} E$	0.0207(0.003)	10.31(0.042)	0.513(0.098)	0.038	0.0051
	$CH_3OH\ 2_{0,2} - 1_{0,1}\ A$	0.167(0.003)	10.26(0.003)	0.49(0.009)	0.319	0.0051
	$CH_3OH 2_{-1,2} - 1_{-1,1} E$	0.118(0.003)	10.26(0.005)	0.478(0.013)	0.233	0.0051
	$CH_3CHO\ 5_{0,5} - 4_{0,4}\ A$	-	-	-	_	0.0054
	$CH_3CHO\ 5_{0,5} - 4_{0,4}\ E$	_	_	_	_	0.0054
	$CH_2CHCN\ 10_{0,10} - 9_{0,9}$	-	-	-	_	0.0076
	$CH_2CHCN\ 10_{1,9} - 9_{1,8}$	-	-	-	_	0.0052
99	$CH_3OH\ 2_{0,2} - 1_{0,1} E$	0.0236(0.003)	10.38(0.022)	0.394(0.065)	0.0562	0.0061
	$CH_3OH\ 2_{0,2} - 1_{0,1}\ A$	0.351(0.003)	10.40(0.002)	0.416(0.005)	0.792	0.0061
	$CH_3OH 2_{-1,2} - 1_{-1,1} E$	0.257(0.003)	10.40(0.002)	0.398(0.005)	0.605	0.0061
	$CH_3CHO\ 5_{0,5} - 4_{0,4}\ A$	0.0136(0.003)	10.14(0.056)	0.535(0.103)	0.0239	0.0053
	$CH_3CHO\ 5_{0,5} - 4_{0,4}\ E$	0.00919(0.002)	10.23(0.055)	0.382(0.112)	0.0226	0.0053
	$CH_2CHCN\ 10_{0,10} - 9_{0,9}$	_	_	-	_	0.0077
	$CH_2CHCN\ 10_{1,9} - 9_{1,8}$	-	-	-	_	0.0053
00	$CH_3OH\ 2_{0,2} - 1_{0,1} E$	0.0382(0.003)	10.51(0.026)	0.531(0.052)	0.0676	0.0056
	$CH_3OH\ 2_{0,2} - 1_{0,1}\ A$	0.493(0.003)	10.45(0.002)	0.612(0.005)	0.758	0.0056
	$CH_3OH \ 2_{-1,2} - 1_{-1,1} \ E$	0.37(0.003)	10.44(0.003)	0.62(0.007)	0.56	0.0056
	$CH_3CHO\ 5_{0,5} - 4_{0,4}\ A$	0.028(0.005)	10.37(0.104)	1.3(0.29)	0.0203	0.0050
	CH ₃ CHO $5_{0,5} - 4_{0,4}$ E	0.0164(0.003)	10.14(0.083)	0.7(0.174)	0.022	0.0050
	$CH_2CHCN\ 10_{0,10} - 9_{0,9}$	_	_	_	_	0.0083
	$CH_2CHCN\ 10_{1.9} - 9_{1.8}$	_	_	_	_	0.0060

Note. Errors reported in parentheses next to the number.

APPENDIX B: SUPPLEMENTAL MATERIAL FROM YEBES 40 M OBSERVATIONS

As mentioned in Section 3.2, the *Q*-band receiver on the Yebes 40m spans 18.5 GHz, from 31.5–50 GHz, and the beam size therefore ranges from 36–56 arcsec. The resolution of 38.0kHz (0.38 km s⁻¹ 0.23 km s⁻¹ across the band) was sufficient to sample the COM lines that have linewidths > 0.4 km s⁻¹. The pointing corrections were obtained using these specific sources: TXCAM; 05:00:50.39, +56:10:52.5, J2000.0, IKTAU; 03:53:28.87, +11:24:21.7, J2000.0, or V11110PH; 18:37:19.26, +10:25:42.2, J2000.0.

Publicly available PYTHON-based scripts (see Data Availability) developed by Megías et al. (2023) were used to reduce the data. With this combination of PYTHON scripts we loaded in for each source all the data files, searched for lines above a set noise (RMS) level, used those to perform initial baselines, Doppler corrected for the line-of-sight velocity across the band, and then combined all the spectral windows for each polarization into single CLASS data file. In total there were 16 spectral windows to combine (eight windows and two polarizations) and in some cases multiple data files to combine if a source was observed over multiple days. During this process the main beam efficiency, η_{mb} , measured by Yebes to be 0.66(0.65) at 32.4 GHz, 0.62(0.62) at 34.5 GHz, 0.62(0.60) at 36.9 GHz, 0.59(0.58) at 39.2 GHz, 0.58(0.56) at 41.4 GHz, 0.56(0.54) at 43.7 GHz, 0.54(0.51) at 46.0 GHz and 0.51(0.49) at 48.4 GHz for the horizontal (vertical) polarizations, were used to scale our observations to the main beam temperature, $T_{\rm mb}$. In this initial reduction we set a high intensity threshold (or RMS cutoff) of 200 mK because the baseline ripples are high due to the frequency switching technique and if a lower threshold was set, this could lead to 'ripple-peaks' mistaken as lines

Additional CLASS scripts for each source were run to select specific COM transitions of interest by frequency (Tables 2 and B1), which were then re-baselined and fit with a Gaussian (if a line was detected at $> 3\sigma_{T_{\rm mb}}$). A polynomial baseline of degree 10 needed to be used, due to the large baseline ripples produced from the frequency switching technique not completely erased from the initial pipeline procedure and as done in other studies (e.g. Agúndez et al. 2023).

We note that we selected only those transitions that would be 'energetically favourable' for cold starless cores, i.e. these transitions have upper energies or $E_u < 25 \, \mathrm{K}$ and Einstein A_{ul} values $> 1.0 \times 10^{-7} \, \mathrm{s^{-1}}$ (and for CH₃CHO, CH₂CHCN, and HCOOCH₃ only a-type transitions). For CH₂CHCN, HCOOCH₃, and CH₃OCH₃ there are several additional lines within the bandpass that fit this criteria. Yet, these COMs were not detected in any of our sources and therefore we do not include them in Table 2 for clarity. Instead, in Table B1 we list additional non-detected transitions of CH₂CHCN, HCOOCH₃, and CH₃OCH₃ that we consider energetically favourable, i.e. transitions have upper energies, $E_u < 25 \, \mathrm{K}$ and Einstein A_{ul} values $> 1.0 \, \mathrm{E} - 07 \, \mathrm{s^{-1}}$. For CH₂CHCN and HCOOCH₃ we also only consider a-type states for these asymmetric top molecules.

In Table B2 we list the Gaussian fit line parameters, as well as RMS values, calculated using the CLASS software for the Yebes 40 m spectral data towards the 15-core sub-sample. For the higher complexity COMs CH₂CHCN, HCOOCH₃, and CH₃OCH₃ only the detected transitions are listed and in bold. Line velocities have been re-shifted to the corresponding rest frequencies. The spectra of the additional CH₃OH and CH₃CHO lines are also presented here in Figs B1, B2, and B3.

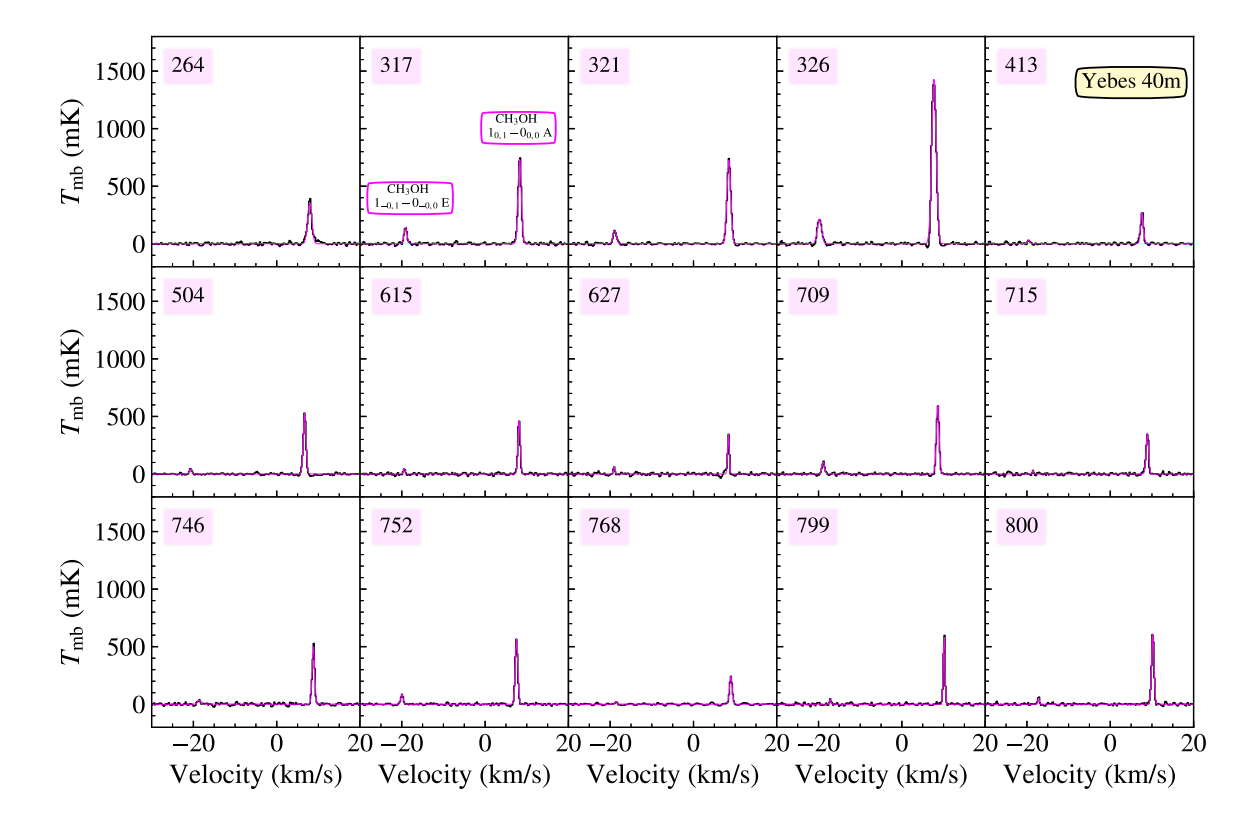


Figure B1. Methanol, CH₃OH, spectrum (in black) in units of $T_{\rm mb}$ (K) versus velocity (km s⁻¹) from the Yebes 40m for the 15 core sub-sample. Gaussian fits are overplotted (in magenta). There are two 1 – 0 transitions observable, and the A state transitions is centred on the $v_{\rm lsr}$ of the core.

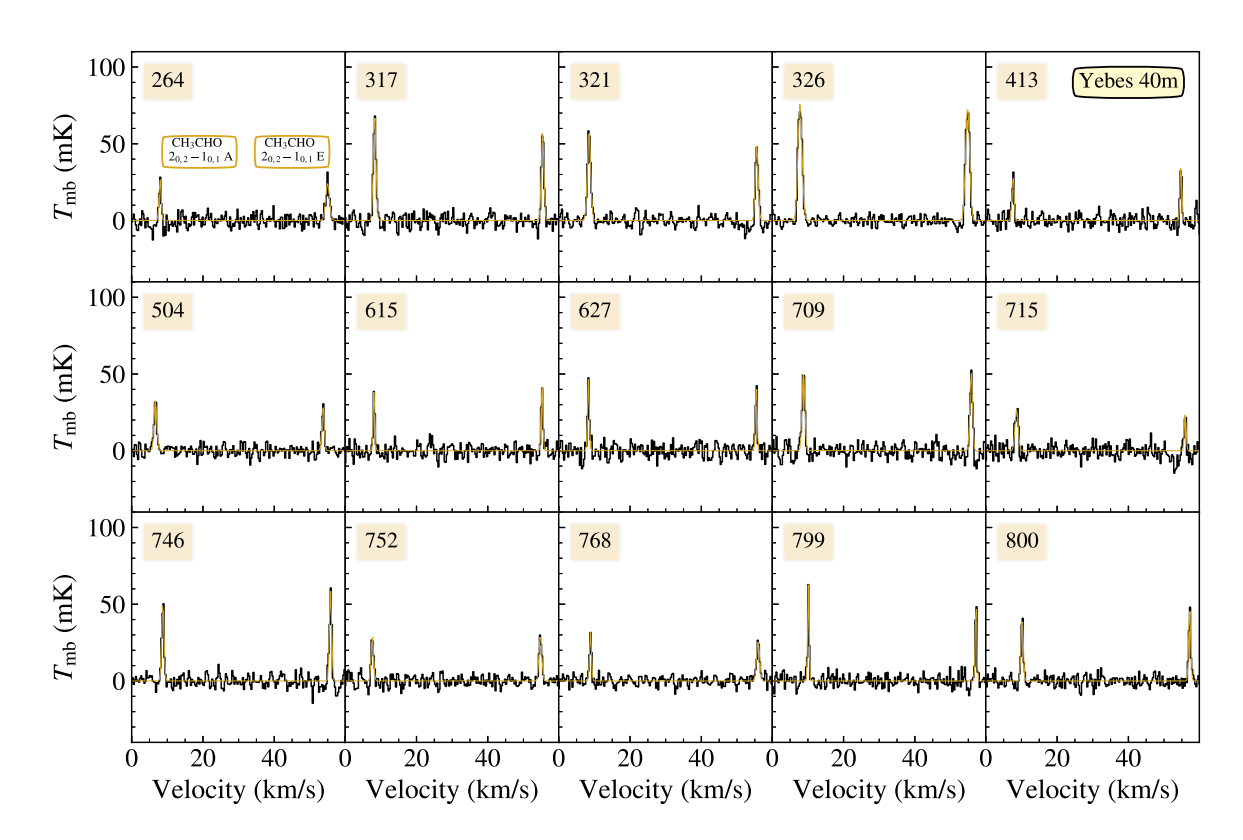


Figure B2. Acetaldehyde, CH₃CHO, spectrum (in black) in units of $T_{\rm mb}$ (K) versus velocity (km s⁻¹) from the Yebes 40m for the 15 core sub-sample. Gaussian fits are overplotted (in gold). There are two 2-1 transitions observable, and the A state transitions is centered on the v_{lsr} of the core.

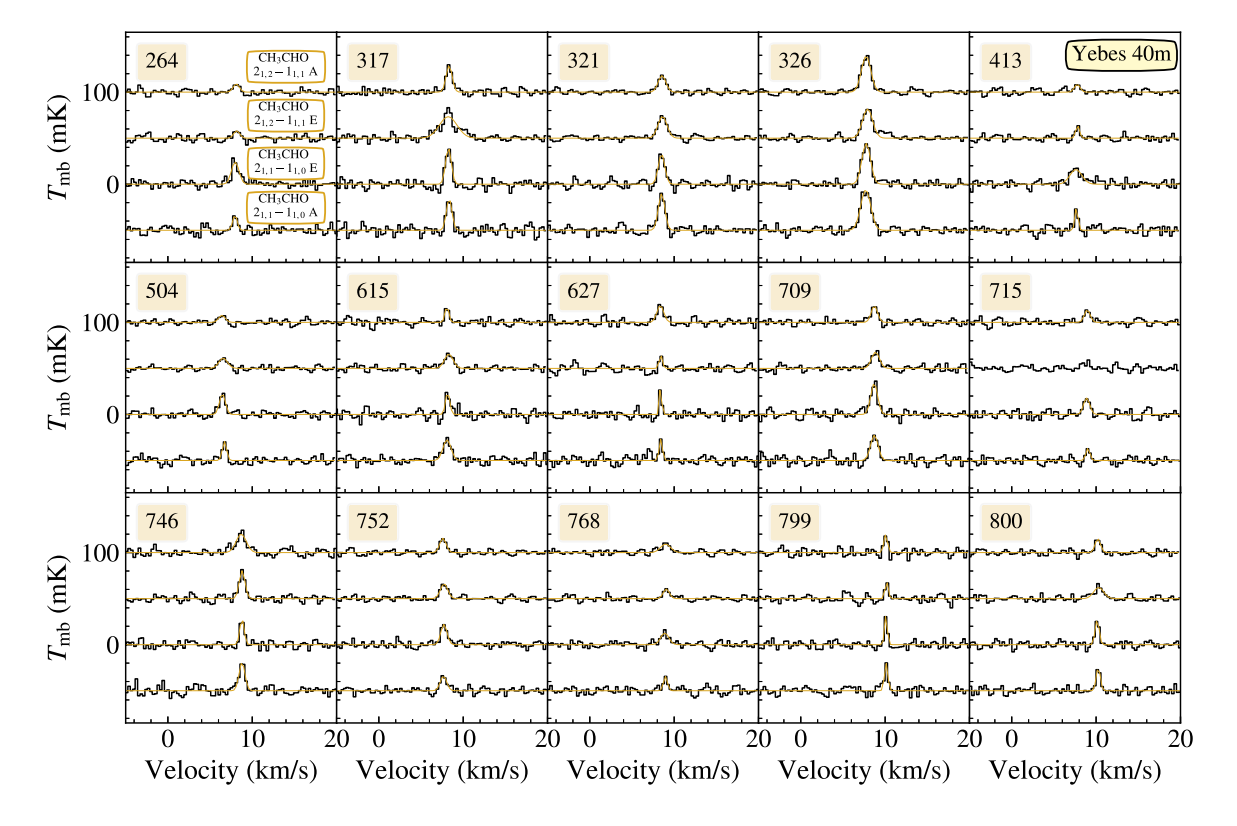


Figure B3. Additional acetaldehyde, CH₃CHO, spectrum (in black) in units of $T_{\rm mb}$ (K) versus velocity (km s⁻¹) from the Yebes 40 m for the 15 core sub-sample. Gaussian fits are overplotted (in gold). There are four separate 2-1 transitions observable, and all transitions are centered on the $v_{\rm lsr}$ of the core. Spectra are offset by intervals of 50 mK for easier viewing.

Table B1. Non-detected energetically favourable COM transitions in Yebes 40 m band.

Molecule	Transition	Rest frequency, ν (GHz)	E _u /k (K)	g_u	A_{ul} (s ⁻¹)	θ_b^1 arcsec	Average $\sigma_{T_{\rm mb}}^{2}$ (mK)
CH ₂ CHCN	$4_{3,2} - 3_{3,1}$	37.952627	24.0	27	1.8E-06	47.7	2.52(0.44)
	$4_{3,1} - 3_{3,0}$	37.952726	24.0	27	1.8E-06	47.7	2.52(0.40)
	$4_{2,2} - 3_{2,1}$	37.974365	13.2	27	3.1E-06	47.6	2.77(0.40)
	$4_{1,3} - 3_{1,2}$	38.847735	6.8	27	4.1E-06	46.6	2.76(0.42)
	$5_{1,5} - 4_{1,4}$	46.266933	8.8	33	7.3e-06	39.1	5.38(1.07)
	$5_{0,5} - 4_{0,4}$	47.354648	6.8	33	8.2E-06	38.2	6.01(1.04)
	$5_{2,3} - 4_{2,2}$	47.489229	15.4	33	6.9E-06	38.1	6.07(1.27)
	$5_{1,4} - 4_{1,3}$	48.552562	9.1	33	8.5E-06	37.3	7.79(2.10)
$HCOOCH_3$	$3_{1,3} - 2_{1,2} E$	34.156884	3.9	14	4.6E-07	53.0	2.57(0.34)
	$3_{1,3} - 2_{1,2} A$	34.158119	3.9	14	4.6E-07	53.0	2.47(0.39)
	$3_{2,2} - 2_{2,1} E$	36.678607	6.2	14	3.3E-07	49.3	2.41(0.35)
	$3_{2,2} - 2_{2,1} A$	36.657467	6.1	14	3.6E-07	49.3	2.57(0.36)
	$3_{2,1} - 2_{2,0} E$	37.182123	6.2	14	3.4E-07	48.6	2.72(0.40)
	$3_{2,1} - 2_{2,0} A$	37.209617	6.2	14	3.7E-07	48.6	2.69(0.35)
	$3_{1,2} - 2_{1,1} A$	38.980809	4.4	14	6.9E-07	46.4	3.23(0.56)
	$4_{2,3} - 3_{2,2} E$	48.768304	8.5	18	1.2E-06	37.1	7.57(0.91)
	$4_{2,3} - 3_{2,2} A$	48.767016	8.5	18	1.2E-06	37.1	7.85(1.12)
	$4_{3,2} - 3_{3,1} E$	49.151617	11.9	18	7.1E-07	36.8	8.11(1.49)
	$4_{3,1} - 3_{3,0} E$	49.155295	11.9	18	7.1E-07	36.8	7.63(0.98)
	$4_{3,2} - 3_{3,1} A$	49.134631	11.9	18	7.1E-07	36.8	8.13(0.93)
	$4_{3,1} - 3_{3,0}A$	49.180102	11.9	18	7.2E-07	36.8	7.79(0.81)
CH_3OCH_3	$5_{1,4} - 5_{0,5}$ EE	39.047303	15.4	176	5.0E-07	46.3	2.96(0.29)
	$6_{1,5} - 6_{0,6}$ EE	43.447572	21.0	208	6.5E-07	41.6	4.15(0.72)
	$1_{1,1} - 0_{0,0}$ EE	47.674967	2.2	48	1.7E-07	37.9	7.16(1.28)
	$1_{1,0} - 0_{0,0}$ EE	48.844676	2.3	48	1.9E-07	37.0	7.55(1.08)
	$4_{0,4} - 3_{1,3}$ EE	49.461855	9.0	144	4.5E-07	36.6	8.85(2.26)

Note. Values for HCOOCH₃ from JPL catalogue⁶ (Pickett et al. 1998) and for the remaining transitions from CDMS data base⁷ (Müller et al. 2001; Müller et al. 2005; Endres et al. 2016). ¹The beam size corresponding to the selected molecular transition. ¹ The average noise level for the Yebes 40 m 15 core sub-sample, where the standard deviation is listed in parentheses. Note that only the EE states for CH₃OCH₃ are listed.

⁶https://spec.jpl.nasa.gov/

⁷https://cdms.astro.uni-koeln.de

Table B2. Yebes 40 m line parameters.

Core	Line	Area (K-km s ⁻¹)	Vel (km s-1)	FWHM (km s ⁻¹)	$T_{ m mb}$ (K)	RMS (K)
264	t-HCOOH 2 _{1.2} – 1 _{1.1}	0.0462(0.005)	8.292(0.212)	3.55(0.423)	0.01223	0.0038
	t-HCOOH $2_{0,2} - 1_{0,1}$	_	_	_	_	0.0047
	t-HCOOH $2_{1,1} - 1_{1,0}$	_	_	_	_	0.0067
	$H_2CCO\ 2_{1,2}-1_{1,1}$	_	_	_	_	0.0031
	$H_2CCO\ 2_{0,2}-1_{0,1}$	-	_	-	_	0.0033
	$H_2CCO\ 2_{1,1}-1_{1,0}$	-	_	_	_	0.0040
	$CH_3OH\ 1_{0,1} - 0_{0,0}\ A$	0.448(0.008)	7.901(0.009)	1.15(0.026)	0.3650	0.0082
	$CH_3OH 1_{-0,1} - 0_{-0,0} E$	-	_	-	_	0.0082
	$CH_3CN\ 2_1 - 1_1$	-	_	-	_	0.0021
	$CH_3CN 2_0 - 1_0$	0.0295(0.003)	7.656(0.085)	1.83(0.234)	0.01513	0.0021
	$CH_3CHO\ 2_{1,2} - 1_{1,1}\ A$	0.0082(0.002)	8.106(0.104)	0.865(0.2)	0.008904	0.0025
	$CH_3CHO\ 2_{1,2} - 1_{1,1}\ E$	0.00709(0.002)	8.157(0.12)	0.823(0.241)	0.008089	0.0027
	$CH_3CHO\ 2_{0,2} - 1_{0,1}\ E$	0.0332(0.004)	7.927(0.065)	1.3(0.166)	0.02398	0.0041
	$CH_3CHO\ 2_{0,2}-1_{0,1}\ A$	0.0198(0.002)	7.952(0.042)	0.686(0.099)	0.02718	0.0041
	$CH_3CHO\ 2_{1,1} - 1_{1,0}\ E$	0.0271(0.003)	7.979(0.05)	1.06(0.172)	0.02406	0.0028
	$CH_3CHO\ 2_{1,1}-1_{1,0}\ A$	0.0111(0.002)	7.948(0.061)	0.629(0.145)	0.01654	0.0038
	$CH_2CHCN4_{1,4} - 3_{1,3}$	0.00812(0.002)	7.221(0.091)	0.846(0.210)	0.00902	0.0024
	$HCOOCH_34_{0,4} - 3_{0,3} A$	0.0192(0.005)	7.086(0.122)	0.999(0.301)	0.01810	0.0064
	$HCOOCH_34_{1,4} - 3_{1,3} E$	0.02391(0.005)	8.099(0.249)	2.083(0.520)	0.01787	0.0049
	$HCOOCH_34_{1,4} - 3_{1,3} A$	0.01797(0.003)	6.868(0.070)	0.758(0.147)	0.02276	0.0049
	$CH_3OCH_33_{1,2} - 3_{0,3} AE + EA$	0.00760(0.002)	8.337(0.160)	1.223(0.250)	0.00584	0.0016
	$CH_3OCH_33_{1,2} - 3_{0,3} EE$	0.01879(0.002)	7.837(0.135)	2.149(0.302)	0.00821	0.0016
	$CH_3OCH_33_{1,2} - 3_{0,3} AA$	0.01340(0.002)	8.042(0.178)	2.072(0.427)	0.00607	0.0016
317	t-HCOOH $2_{1,2} - 1_{1,1}$	-	_	_	_	0.0036
	t-HCOOH $2_{0,2} - 1_{0,1}$	0.0103(0.003)	9.399(0.109)	0.687(0.239)	0.01403	0.0044
	t-HCOOH $2_{1,1} - 1_{1,0}$	-	-	-	-	0.0062
	$H_2CCO\ 2_{1,2} - 1_{1,1}$	0.0129(0.002)	8.283(0.064)	0.717(0.148)	0.01689	0.0032
	$H_2CCO\ 2_{0,2} - 1_{0,1}$	0.0139(0.002)	8.513(0.065)	0.765(0.155)	0.01706	0.0031
	$H_2CCO\ 2_{1,1} - 1_{1,0}$	0.0096(0.002)	8.189(0.065)	0.565(0.13)	0.0161	0.0038
	$CH_3OH\ 1_{0,1} - 0_{0,0}\ A$	0.732(0.006)	8.286(0.001)	0.899(0.008)	0.7645	0.0077
	$CH_3OH 1_{-0,1} - 0_{-0,0} E$	0.126(0.006)	8.614(0.017)	0.815(0.041)	0.1446	0.0077
	$CH_3CN 2_1 - 1_1$	-	-	-	-	0.0028
	$CH_3CN\ 2_0 - 1_0$	0.00696(0.002)	7.762(0.062)	0.441(0.236)	0.01482	0.0028
	$CH_3CHO\ 2_{1,2} - 1_{1,1}\ A$	0.0259(0.002)	8.328(0.035)	0.836(0.09)	0.02905	0.0028
	$CH_3CHO\ 2_{1,2} - 1_{1,1} E$	0.0611(0.004)	8.222(0.067)	2.46(0.22)	0.02332	0.0025
	$CH_3CHO\ 2_{0,2} - 1_{0,1}\ E$	0.0529(0.003)	8.312(0.022)	0.846(0.048)	0.05873	0.0035
	$CH_3CHO\ 2_{0,2}-1_{0,1}\ A$	0.065(0.003)	8.267(0.021)	0.895(0.047)	0.06822	0.0035
	$CH_3CHO\ 2_{1,1} - 1_{1,0}\ E$	0.0333(0.003)	8.251(0.031)	0.798(0.062)	0.03925	0.0034
	$CH_3CHO\ 2_{1,1} - 1_{1,0}\ A$	0.0284(0.003)	8.334(0.041)	0.78(0.08)	0.03427	0.0042
321	t-HCOOH $2_{1,2} - 1_{1,1}$	-	_	_	_	0.0033
	t-HCOOH $2_{0,2} - 1_{0,1}$	-	_	_	_	0.0038
	t-HCOOH $2_{1,1} - 1_{1,0}$	-	_	-	_	0.0037
	$H_2CCO\ 2_{1,2}-1_{1,1}$	0.0182(0.002)	8.54(0.063)	1.07(0.141)	0.01602	0.0026
	$H_2CCO\ 2_{0,2} - 1_{0,1}$	0.0073(0.002)	8.268(0.068)	0.61(0.148)	0.01138	0.0026
	$H_2CCO\ 2_{1,1}-1_{1,0}$	0.0334(0.002)	8.407(0.048)	1.42(0.102)	0.02215	0.0024
	$CH_3OH\ 1_{0,1} - 0_{0,0}\ A$	0.839(0.005)	8.520(0.003)	1.08(0.007)	0.7299	0.0066
	$CH_3OH \ 1_{-0,1} - 0_{-0,0} E$	0.114(0.005)	8.574(0.018)	0.945(0.046)	0.1134	0.0066
	$CH_3CN 2_1 - 1_1$	-	-	-	_	0.0026
	$CH_3CN 2_0 - 1_0$	_	-	_	_	0.0026
	$CH_3CHO\ 2_{1,2}-1_{1,1}\ A$	0.0205(0.002)	8.556(0.045)	1.07(0.107)	0.01795	0.0020
	$CH_3CHO\ 2_{1,2}-1_{1,1}\ E$	0.0318(0.002)	8.61(0.039)	1.26(0.1)	0.02362	0.0021
	$CH_3CHO\ 2_{0,2} - 1_{0,1} E$	0.0487(0.003)	8.528(0.025)	0.943(0.059)	0.04846	0.0035
	$CH_3CHO\ 2_{0,2} - 1_{0,1}\ A$	0.0699(0.003)	8.494(0.023)	1.11(0.056)	0.05911	0.0035
	CH ₃ CHO $2_{1,1} - 1_{1,0}$ E	0.0314(0.003)	8.502(0.04)	0.901(0.088)	0.03276	0.0033
	$CH_3CHO\ 2_{1,1} - 1_{1,0}\ A$	0.0385(0.003)	8.507(0.03)	0.909(0.068)	0.0398	0.0032
	$HCOOCH_34_{1,4} - 3_{1,3} E$	0.0209(0.004)	8.457(0.073)	0.883(0.175)	0.02231	0.0049
	$HCOOCH_34_{1,4} - 3_{1,3} A$	0.0485(0.006)	8.992(0.154)	2.528(0.355)	0.01804	0.0049
	$CH_3OCH_33_{1,2} - 3_{0,3} AE + EA$	0.0049(0.001)	8.463(0.111)	0.689(0.213)	0.00680	0.0014
	$CH_3OCH_33_{1,2} - 3_{0,3} EE$	0.0244(0.003)	8.107(0.155)	2.530(0.450)	0.00907	0.0014
226	$CH_3OCH_33_{1,2} - 3_{0,3} AA$	0.0073(0.002)	8.106(0.098)	0.814(0.177)	0.00853	0.0014
326	t-HCOOH $2_{1,2} - 1_{1,1}$	0.0519(0.005)	8.682(0.188)	3.69(0.379)	0.0132	0.0035
	t-HCOOH $2_{0,2} - 1_{0,1}$	0.0319(0.004)	7.925(0.093)	1.59(0.228)	0.0188	0.0035
	t-HCOOH $2_{1,1} - 1_{1,0}$	-	-	-	-	0.0041

Table B2 - continued

Core	Line	Area (K-km s ⁻¹)	$(km s^{-1})$	FWHM (km s ⁻¹)	$T_{ m mb}$ (K)	RMS (K)
	H ₂ CCO 2 _{1.2} – 1 _{1.1}	0.044(0.002)	7.77(0.035)	1.26(0.071)	0.03268	0.002
	$H_2CCO\ 2_{0.2} - 1_{0.1}$	0.0311(0.002)	7.657(0.047)	1.2(0.095)	0.02435	0.002
	$H_2CCO 2_{1,1} - 1_{1,0}$	0.0399(0.002)	7.641(0.027)	1.09(0.058)	0.03427	0.002
	$CH_3OH 1_{0.1} - 0_{0.0} A$	1.92(0.006)	7.673(0.002)	1.23(0.005)	1.463	0.007
	$CH_3OH 1_{-0.1} - 0_{-0.0} E$	0.277(0.006)	7.683(0.014)	1.19(0.03)	0.2181	0.007
	$CH_3CN 2_1 - 1_1$	0.0103(0.002)	5.577(0.101)	0.904(0.177)	0.01067	0.003
	$CH_3CN 2_0 - 1_0$	0.0487(0.003)	7.136(0.05)	1.65(0.114)	0.02767	0.003
	$CH_3CHO\ 2_{1,2} - 1_{1,1}\ A$	0.0547(0.002)	7.745(0.023)	1.31(0.055)	0.03922	0.002
	$CH_3CHO\ 2_{1,2} - 1_{1,1} E$	0.0474(0.002)	7.918(0.034)	1.41(0.086)	0.0317	0.001
	$CH_3CHO\ 2_{0.2} - 1_{0.1}\ E$	0.104(0.002)	7.744(0.015)	1.31(0.032)	0.07435	0.002
	CH ₃ CHO $2_{0,2} - 1_{0,1}$ A	0.109(0.002)	7.8(0.015)	1.34(0.032)	0.07626	0.002
	CH ₃ CHO $2_{1.1} - 1_{1.0}$ E	0.057(0.002)	7.756(0.025)	1.21(0.056)	0.04426	0.002
	CH ₃ CHO $2_{1,1} - 1_{1,0}$ A	0.0655(0.003)	7.696(0.028)	1.41(0.062)	0.04376	0.002
	$HCOOCH_33_{2,2} - 2_{2,1} A$	0.0091(0.003)	8.181(0.188)	1.483(0.939)	0.0057	0.002
	$HCOOCH_33_{0,3} - 2_{0,2} E$	0.0063(0.001)	7.749(0.076)	0.668(0.137)	0.0088	0.002
	$HCOOCH_33_{0,3} - 2_{0,2} A$	0.0120(0.002)	7.584(0.119)	1.391(0.219)	0.0081	0.002
	$HCOOCH_34_{0.4} - 3_{0.3} A$	0.0398(0.005)	7.753(0.078)	1.241(0.176)	0.0302	0.006
	$CH_3OCH_33_{1,2} - 3_{0,3} AE + EA$	0.01189(0.002)	7.472(0.179)	1.717(0.348)	0.00650	0.002
	$CH_3OCH_33_{1,2} - 3_{0,3} EE$	0.01785(0.002)	7.769(0.074)	1.254(0.195)	0.01338	0.002
	$CH_3OCH_3S_{1,2} - S_{0,3}AA$	0.01878(0.002)	7.338(0.110)	1.631(0.210)	0.01081	0.002
	$CH_3OCH_34_{1,3} - 4_{0,4} AE + EA$	0.00995(0.002)	7.321(0.113)	1.323(0.201)	0.00706	0.00
	$CH_3OCH_34_{1.3} - 4_{0.4} EE$	0.01909(0.003)	7.973(0.132)	2.107(0.426)	0.00851	0.00
	$CH_3OCH_34_{1,3} - 4_{0,4}AA$	0.01617(0.002)	8.357(0.085)	1.431(0.217)	0.01061	0.00
3	t-HCOOH $2_{1,2} - 1_{1,1}$	-	-	-	-	0.003
,	t-HCOOH $2_{0,2} - 1_{0,1}$	_	_	_	_	0.003
	t-HCOOH $2_{1,1} - 1_{1,0}$	_	_	_	_	0.000
	$H_2CCO\ 2_{1,2} - 1_{1,1}$	0.0124(0.002)	7.711(0.04)	0.497(0.107)	0.02341	0.002
	$H_2CCO\ 2_{0,2} - 1_{0,1}$	0.0086(0.002)	7.767(0.054)	0.489(0.086)	0.01671	0.003
	$H_2CCO\ 2_{1,1} - 1_{1,0}$	0.0188(0.002)	7.701(0.034)	0.764(0.087)	0.02314	0.002
	CH ₃ OH $1_{0.1} - 0_{0.0}$ A	0.233(0.005)	7.639(0.007)	0.784(0.02)	0.2793	0.00
	CH ₃ OH $1_{-0,1} - 0_{-0,0}$ E	0.0204(0.004)	7.917(0.077)	0.646(0.16)	0.02974	0.00
	$CH_3CH_{1-0,1} = 0_{-0,0} E$ $CH_3CN_{21} - 1_1$	0.0165(0.002)	5.679(0.059)	0.983(0.159)	0.01582	0.002
	$CH_3CN 2_0 - 1_0$	0.0349(0.002)	7.212(0.034)	1.11(0.085)	0.02961	0.002
	$CH_3CHO 2_{1,2} - 1_{1,1} A$	0.00714(0.002)	7.76(0.101)	0.793(0.257)	0.00846	0.002
	CH ₃ CHO $2_{1,2} - 1_{1,1}$ A CH ₃ CHO $2_{1,2} - 1_{1,1}$ E	0.00714(0.002)	7.812(0.055)	0.535(0.15)	0.01371	0.002
	CH ₃ CHO $2_{1,2} - 1_{1,1}$ E CH ₃ CHO $2_{0,2} - 1_{0,1}$ E	0.0238(0.002)	7.703(0.03)	0.617(0.061)	0.03631	0.002
	CH ₃ CHO $2_{0,2} - 1_{0,1}$ E CH ₃ CHO $2_{0,2} - 1_{0,1}$ A	0.023(0.002)	7.621(0.044)	0.73(0.108)	0.03031	0.00
	CH ₃ CHO $2_{0,2} - 1_{0,1}$ A CH ₃ CHO $2_{1,1} - 1_{1,0}$ E		7.605(0.11)			0.00
	CH ₃ CHO $2_{1,1} - 1_{1,0}$ E CH ₃ CHO $2_{1,1} - 1_{1,0}$ A	0.0284(0.004) 0.0115(0.002)	7.671(0.042)	1.67(0.331) 0.429(0.107)	0.01593 0.02519	0.003
		0.0113(0.002)	7.486(0.083)	0.882 (0.180)	0.02319	0.002
	$CH_2CHCN 4_{1,4} - 3_{1,3}$	0.0041(0.001)	7.713 (0.041)	0.302 (0.556)	0.01106	0.002
1	$CH_2CHCN 4_{0,4} - 3_{0,3}$	` /	7.713 (0.041)	0.302 (0.330)		0.002
+	t-HCOOH 2 _{1,2} - 1 _{1,1}	0.0007(0.002)	6 91(0 054)	0.645(0.100)	- 0.01424	
	t-HCOOH 2 _{0,2} - 1 _{0,1}	0.0097(0.002)	6.81(0.054)	0.645(0.108)	0.01424	0.002
	t-HCOOH $2_{1,1} - 1_{1,0}$	0.00955(0.001)	- 6 721(0 04)	0.440(0.069)	0.0170	
	$H_2CCO\ 2_{1,2} - 1_{1,1}$	0.00855(0.001)	6.731(0.04)	0.449(0.068)	0.0179	0.002
	$H_2CCO\ 2_{0,2} - 1_{0,1}$	0.0144(0.002)	6.441(0.052)	0.818(0.103)	0.01651	0.002
	$H_2CCO\ 2_{1,1} - 1_{1,0}$	0.0189(0.003)	6.471(0.111)	1.22(0.206)	0.01456	0.002
	$CH_3OH 1_{0,1} - 0_{0,0} A$	0.43(0.004)	6.678(0.004)	0.759(0.009)	0.5324	0.007
	$CH_3OH\ 1_{-0,1} - 0_{-0,0} E$	0.0332(0.004)	6.783(0.038)	0.652(0.087)	0.04791	0.007
	$CH_3CN 2_1 - 1_1$	0.02(0(0.002)	-	1 45(0 152)	- 0.02202	0.003
	$CH_3CN 2_0 - 1_0$	0.0369(0.003)	6.078(0.06)	1.45(0.152)	0.02392	0.003
	$CH_3CHO\ 2_{1,2} - 1_{1,1}\ A$	0.00746(0.002)	6.407(0.115)	0.925(0.189)	0.00757	0.002
	$CH_3CHO\ 2_{1,2} - 1_{1,1} E$	0.0144(0.002)	6.552(0.081)	1.22(0.163)	0.01106	0.00
	CH ₃ CHO $2_{0,2} - 1_{0,1}$ E	0.0251(0.002)	6.603(0.033)	0.799(0.081)	0.02947	0.002
	CH ₃ CHO $2_{0,2} - 1_{0,1}$ A	0.0312(0.002)	6.643(0.032)	0.873(0.085)	0.03356	0.002
	CH ₃ CHO $2_{1,1} - 1_{1,0}$ E	0.0196(0.002)	6.465(0.044)	0.825(0.126)	0.02231	0.002
_	$CH_3CHO\ 2_{1,1} - 1_{1,0}\ A$	0.013(0.002)	6.709(0.045)	0.591(0.092)	0.0207	0.003
5	t-HCOOH $2_{1,2} - 1_{1,1}$	-	-	_	_	0.005
	t-HCOOH $2_{0,2} - 1_{0,1}$	-	-	_	_	0.00
	t-HCOOH $2_{1,1} - 1_{1,0}$	_	_	_	_	0.005
	$H_2CCO\ 2_{1,2}-1_{1,1}$	0.0112(0.002)	8.232(0.07)	0.552(0.121)	0.01902	0.003
	$H_2CCO\ 2_{0,2}-1_{0,1}$	0.0406(0.005)	8.455(0.17)	2.96(0.431)	0.01287	0.003
	H_2 CCO $2_{1,1} - 1_{1,0}$	0.00953(0.002)	8.041(0.05)	0.447(0.101)	0.02005	0.003

Table B2 - continued

Core	Line	Area (K-km s ⁻¹)	Vel (km s-1)	FWHM (km s ⁻¹)	$T_{ m mb}$ (K)	RMS (K)
	CH ₃ OH 1 _{0.1} – 0 _{0.0} A	0.325(0.005)	8.115(0.004)	0.634(0.011)	0.4824	0.0079
	$CH_3OH 1_{-0.1} - 0_{-0.0} E$	0.0258(0.004)	8.060(0.041)	0.506(0.079)	0.04794	0.0079
	$CH_3CN 2_1 - 1_1$	-	-	-	-	0.0027
	$CH_3CN 2_0 - 1_0$	_	_	_	_	0.0027
	$CH_3CHO\ 2_{1,2}-1_{1,1}\ A$	0.00983(0.002)	8.067(0.044)	0.525(0.137)	0.0176	0.0029
	$CH_3CHO\ 2_{1,2} - 1_{1,1} E$	0.0199(0.002)	8.289(0.075)	1.21(0.166)	0.01548	0.0027
	$CH_3CHO\ 2_{0,2}-1_{0,1}\ E$	0.0264(0.002)	8.13(0.025)	0.579(0.057)	0.04284	0.0036
	$CH_3CHO\ 2_{0,2} - 1_{0,1}\ A$	0.0222(0.002)	8.107(0.024)	0.512(0.065)	0.04076	0.0036
	$CH_3CHO\ 2_{1,1} - 1_{1,0}\ E$	0.015(0.003)	8.153(0.066)	0.585(0.161)	0.02416	0.0039
	$CH_3CHO\ 2_{1,1} - 1_{1,0}\ A$	0.0268(0.003)	8.079(0.064)	1.12(0.169)	0.0224	0.0035
527	t-HCOOH $2_{1,2} - 1_{1,1}$	-	-	-	_	0.0050
	t-HCOOH $2_{0,2} - 1_{0,1}$	-	-	-	-	0.0053
	t-HCOOH $2_{1,1} - 1_{1,0}$	_		_	_	0.0067
	$H_2CCO\ 2_{1,2} - 1_{1,1}$	0.0174(0.003)	8.48(0.065)	0.772(0.119)	0.02117	0.0041
	$H_2CCO\ 2_{0,2} - 1_{0,1}$	0.00948(0.003)	8.31(0.119)	0.766(0.213)	0.01163	0.0040
	$H_2CCO\ 2_{1,1} - 1_{1,0}$	0.0138(0.002)	8.298(0.05)	0.569(0.101)	0.02275	0.0041
	$CH_3OH \ 1_{0,1} - 0_{0,0} \ A$	0.176(0.004)	8.402(0.007)	0.482(0.013)	0.3425	0.0106
	CH ₃ OH $1_{-0,1} - 0_{-0,0}$ E CH ₃ CN $2_1 - 1_1$	0.0307(0.005)	8.378(0.035)	0.44(0.076)	0.06566	0.0106 0.0030
	$CH_3CN 2_1 - I_1$ $CH_3CN 2_0 - I_0$	0.0279(0.003)	7.796(0.056)	1.16(0.119)	0.02259	0.0030
	$CH_3CHO 2_{1,2} - 1_{1,1} A$	0.0186(0.003)	8.357(0.068)	0.957(0.237)	0.01829	0.0030
	$CH_3CHO 2_{1,2} - I_{1,1} A$ $CH_3CHO 2_{1,2} - I_{1,1} E$	0.00691(0.002)	8.415(0.074)	0.457(0.132)	0.01421	0.0032
	CH ₃ CHO $2_{0,2} - 1_{0,1}$ E	0.0255(0.003)	8.389(0.025)	0.53(0.084)	0.04528	0.0031
	CH ₃ CHO $2_{0,2} - 1_{0,1}$ A	.0288(0.003)	8.323(0.026)	0.581(0.064)	0.04654	0.0039
	CH ₃ CHO $2_{0,2}$ $1_{0,1}$ $1_{0,1}$ CH ₃ CHO $2_{1,1} - 1_{1,0}$ E	0.0109(0.001)	8.398(0.019)	0.291(0.296)	0.03522	0.0032
	CH ₃ CHO $2_{1,1} - 1_{1,0}$ A	0.0115(0.002)	8.416(0.046)	0.463(0.081)	0.02337	0.0037
	$CH_3OCH_33_{1,2} - 3_{0,3} EE$	0.0308(0.003)	7.645(0.158)	3.024(0.302)	0.00959	0.0022
09	t-HCOOH $2_{1,2} - 1_{1,1}$	_	_	_	_	0.0043
	t-HCOOH $2_{0,2} - 1_{0,1}$	0.0177(0.004)	9.023(0.085)	0.885(0.218)	0.01874	0.0047
	t-HCOOH $2_{1,1} - 1_{1,0}$	0.0192(0.004)	8.98(0.076)	0.688(0.185)	0.02628	0.0063
	$H_2CCO\ 2_{1,2}-1_{1,1}$	0.0379(0.003)	8.916(0.044)	1.18(0.088)	0.0301	0.0032
	$H_2CCO\ 2_{0,2} - 1_{0,1}$	0.0287(0.003)	8.873(0.077)	1.29(0.163)	0.02084	0.0038
	$H_2CCO\ 2_{1,1} - 1_{1,0}$	0.0429(0.004)	8.777(0.044)	1.08(0.11)	0.03722	0.0040
	$CH_3OH\ 1_{0,1} - 0_{0,0}\ A$	0.499(0.004)	8.619(0.003)	0.788(0.008)	0.5949	0.0086
	$CH_3OH 1_{-0,1} - 0_{-0,0} E$	0.0832(0.004)	8.605(0.018)	0.727(0.045)	0.1075	0.0086
	$CH_3CN 2_1 - 1_1$	0.0421(0.003)	6.88(0.054)	1.44(0.13)	0.02757	0.0035
	$CH_3CN \ 2_0 - 1_0$	0.0707(0.003)	8.337(0.028)	1.33(0.059)	0.0501	0.0035
	$CH_3CHO\ 2_{1,2} - 1_{1,1}\ A$	0.0168(0.002)	8.722(0.049)	0.882(0.117)	0.01795	0.0022
	CH ₃ CHO $2_{1,2} - 1_{1,1}$ E CH ₃ CHO $2_{0,2} - 1_{0,1}$ E	0.021(0.003) 0.0477(0.003)	8.855(0.064) 8.739(0.034)	1.12(0.167) 0.877(0.065)	0.01762 0.05106	0.0027 0.0050
	CH ₃ CHO $2_{0,2} - 1_{0,1}$ E CH ₃ CHO $2_{0,2} - 1_{0,1}$ A	0.0506(0.004)	8.75(0.034)	0.903(0.075)	0.05166	0.0050
	$CH_3CHO\ 2_{0,2} = I_{0,1}\ A$ $CH_3CHO\ 2_{1,1} - 1_{1,0}\ E$	0.0343(0.003)	8.702(0.04)	0.958(0.108)	0.03363	0.0035
	CH ₃ CHO $2_{1,1} - 1_{1,0}$ Z	0.0307(0.003)	8.717(0.055)	1.05(0.116)	0.02738	0.0039
	CH ₂ CHCN $4_{0,4} - 3_{0,3}$	0.0133(0.002)	8.989(0.090)	1.008(0.221)	0.0124	0.0027
15	t-HCOOH $2_{1,2} - 1_{1,1}$	_	_	_	_	0.0042
	t-HCOOH $2_{0,2} - 1_{0,1}$	0.0232(0.004)	9.102(0.073)	0.942(0.161)	0.02316	0.0048
	t-HCOOH $2_{1,1} - 1_{1,0}$	_	_	_	_	0.0058
	$H_2CCO\ 2_{1,2} - 1_{1,1}$	0.0255(0.003)	8.938(0.064)	1.15(0.131)	0.02076	0.0034
	$H_2CCO\ 2_{0,2} - 1_{0,1}$	0.0228(0.002)	8.73(0.042)	0.87(0.089)	0.0246	0.0029
	$H_2CCO\ 2_{1,1} - 1_{1,0}$	0.0173(0.002)	8.901(0.049)	0.685(0.113)	0.02371	0.0036
	$CH_3OH\ 1_{0,1} - 0_{0,0}\ A$	0.265(0.005)	8.89(0.001)	0.704(0.016)	0.3539	0.0077
	$CH_3OH 1_{-0,1} - 0_{-0,0} E$	0.011(0.004)	8.926(0.066)	0.328(0.089)	0.03161	0.0077
	$CH_3CN 2_1 - 1_1$	0.019(0.003)	6.691(0.095)	1.22(0.229)	0.01469	0.0033
	$CH_3CN 2_0 - 1_0$	0.0442(0.003)	8.241(0.043)	1.29(0.104)	0.0323	0.0033
	CH ₃ CHO $2_{1,2} - 1_{1,1}$ A	0.0118(0.002)	8.95(0.071)	0.818(0.173)	0.01351	0.0028
	CH ₃ CHO $2_{1,2} - 1_{1,1}$ E	0.015((0.002)	- 0.00(0.050)	- 0.59(0.146)	- 0.02521	0.0026
	CH ₃ CHO $2_{0,2} - 1_{0,1}$ E	0.0156(0.003)	8.899(0.058)	0.58(0.146)	0.02521	0.0040
	$CH_3CHO\ 2_{0,2} - 1_{0,1}\ A$	0.0304(0.003)	8.648(0.062)	1.06(0.113)	0.02693	0.0040
	$CH_3CHO\ 2_{1,1} - 1_{1,0} E$	0.0163(0.003)	8.877(0.07)	0.859(0.141)	0.01787	0.0036
	CH ₃ CHO 2 _{1,1} - 1 _{1,0} A	0.00805(0.002)	9.029(0.066)	0.573(0.134)	0.0132	0.0030
	$CH_2CHCN\ 4_{2,3} - 3_{2,2}$	0.0101(0.002)	8.233(0.064)	0.761(0.165) 2.367(0.451)	0.01256	0.0024 0.0025
	$HCOOCH_33_{2,2} - 2_{2,1} E$	0.0243(0.004)	8.363(0.162)		0.009643	

Table B2 - continued

Core	Line	Area (K-km s ⁻¹)	Vel	FWHM (km s ⁻¹)	$T_{ m mb}$ (K)	RMS (K)
 746	t-HCOOH 2 _{1,2} – 1 _{1,1}	0.0644(0.005)	8.839(0.139)	3.3(0.306)	0.01831	0.0038
	t-HCOOH $2_{0.2} - 1_{0.1}$	0.0199(0.004)	9.08(0.101)	0.956(0.213)	0.01951	0.0054
	t-HCOOH $2_{1,1} - 1_{1,0}$	0.0354(0.007)	9.604(0.291)	2.67(0.471)	0.01244	0.0062
	$H_2CCO\ 2_{1,2}-1_{1,1}$	0.033(0.003)	8.682(0.045)	0.974(0.101)	0.03184	0.0037
	$H_2CCO\ 2_{0,2} - 1_{0,1}$	0.0208(0.003)	8.684(0.042)	0.713(0.101)	0.02742	0.0037
	$H_2CCO 2_{1,1} - 1_{1,0}$	0.0336(0.003)	8.617(0.041)	0.939(0.078)	0.03359	0.0037
	$CH_3OH \ 1_{0,1} - 0_{0,0} \ A$	0.3800(0.006)	8.819(0.005)	0.7(0.013)	0.5101	0.0091
	$CH_3OH 1_{-0.1} - 0_{-0.0} E$	0.0298(0.006)	8.787(0.084)	0.799(0.166)	0.03504	0.0091
	$CH_3CN 2_1 - 1_1$	0.00669(0.002)	6.633(0.102)	0.692(0.156)	0.009092	0.0027
	$CH_3CN 2_0 - 1_0$	0.0403(0.003)	8.06(0.055)	1.53(0.125)	0.02478	0.0027
	$CH_3CHO\ 2_{1,2}-1_{1,1}\ A$	0.0302(0.005)	8.691(0.08)	1.42(0.408)	0.01999	0.0033
	$CH_3CHO\ 2_{1,2}-1_{1,1}\ E$	0.0259(0.002)	8.799(0.035)	0.802(0.092)	0.0303	0.0031
	$CH_3CHO\ 2_{0,2} - 1_{0,1} E$	0.0474(0.003)	8.764(0.022)	0.758(0.055)	0.05875	0.0046
	CH ₃ CHO $2_{0,2} - 1_{0,1}$ A	0.0446(0.003)	8.738(0.025)	0.815(0.057)	0.05145	0.0046
	CH ₃ CHO $2_{1,1} - 1_{1,0}$ E	0.018(0.002)	8.784(0.034)	0.606(0.071)	0.0279	0.0032
	CH ₃ CHO 2 _{1,1} - 1 _{1,0} Z	0.0269(0.003)	8.786(0.046)	0.824(0.12)	0.03069	0.0040
	$\begin{array}{c} \text{CH}_{3}\text{CHO} \ 2_{1,1} & 1_{1,0} \ \text{A} \\ \text{CH}_{2}\text{CHCN} \ 4_{0,4} - 3_{0,3} \end{array}$	0.0098(0.002)	9.147(0.117)	1.078(0.245)	0.00859	0.0040
752	t-HCOOH $2_{1,2} - 1_{1,1}$	0.0336(0.005)	7.81(0.213)	2.55(0.402)	0.01237	0.0024
132	t-HCOOH $2_{1,2} - 1_{1,1}$ t-HCOOH $2_{0,2} - 1_{0,1}$	0.00839(0.002)	7.64(0.062)	0.43(0.119)	0.01237	0.0042
	t-HCOOH $2_{0,2} - 1_{0,1}$ t-HCOOH $2_{1,1} - 1_{1,0}$	0.00639(0.002)	7.04(0.002)	0.43(0.119)		0.0041
			7 956(0 062)		- 0.0142	
	$H_2CCO\ 2_{1,2} - 1_{1,1}$	0.0122(0.002)	7.856(0.062)	0.801(0.146)	0.0143	0.0023
	$H_2CCO\ 2_{0,2} - 1_{0,1}$	0.0241(0.004)	7.615(0.144)	1.89(0.357)	0.01197	0.0031
	$H_2CCO\ 2_{1,1} - 1_{1,0}$	0.0131(0.003)	7.429(0.102)	0.951(0.233)	0.01295	0.0032
	CH ₃ OH $1_{0,1} - 0_{0,0}$ A	0.434(0.004)	7.503(0.003)	0.719(0.008)	0.5673	0.0066
	$CH_3OH 1_{-0,1} - 0_{-0,0} E$	0.0631(0.004)	7.512(0.021)	0.684(0.052)	0.0867	0.0066
	$CH_3CN 2_1 - 1_1$	0.0212(0.002)	5.683(0.058)	1.29(0.108)	0.01543	0.0023
	$CH_3CN 2_0 - 1_0$	0.0219(0.002)	7.232(0.061)	1.36(0.133)	0.01505	0.0023
	$CH_3CHO\ 2_{1,2} - 1_{1,1}\ A$	0.0147(0.002)	7.596(0.055)	0.887(0.122)	0.01559	0.0023
	$CH_3CHO\ 2_{1,2} - 1_{1,1} E$	0.0175(0.002)	7.73(0.052)	1.02(0.106)	0.01606	0.0021
	$CH_3CHO\ 2_{0,2} - 1_{0,1}\ E$	0.0289(0.002)	7.705(0.038)	0.913(0.086)	0.02969	0.0030
	$CH_3CHO\ 2_{0,2} - 1_{0,1}\ A$	0.0255(0.002)	7.63(0.038)	0.819(0.075)	0.02927	0.0030
	$CH_3CHO\ 2_{1,1} - 1_{1,0}\ E$	0.0204(0.002)	7.713(0.049)	0.866(0.119)	0.02207	0.0028
	$CH_3CHO\ 2_{1,1} - 1_{1,0}\ A$	0.0152(0.002)	7.664(0.07)	0.897(0.17)	0.01595	0.0027
768	t -HCOOH $2_{1,2} - 1_{1,1}$	_	_	-	_	0.0028
	t -HCOOH $2_{0,2} - 1_{0,1}$	-	-	-	-	0.0029
	t-HCOOH $2_{1,1} - 1_{1,0}$	_	_	_	_	0.0040
	$H_2CCO\ 2_{1,2}-1_{1,1}$	0.0129(0.002)	9.106(0.063)	0.787(0.125)	0.01535	0.0029
	$H_2CCO\ 2_{0,2}-1_{0,1}$	0.0113(0.002)	8.779(0.09)	0.958(0.184)	0.01103	0.0027
	$H_2CCO 2_{1,1} - 1_{1,0}$	0.0278(0.003)	8.74(0.079)	1.42(0.248)	0.01831	0.0030
	$CH_3OH \ 1_{0,1} - 0_{0,0} \ A$	0.199(0.004)	8.975(0.008)	0.774(0.019)	0.2418	0.0063
	$CH_3OH 1_{-0,1} - 0_{-0,0} E$	0.0125(0.003)	8.901(0.08)	0.556(0.166)	0.02104	0.0063
	$CH_3CN 2_1 - 1_1$	0.00871(0.002)	7.181(0.156)	1.4(0.28)	0.005846	0.0019
	$CH_3CN 2_0 - 1_0$	0.0145(0.002)	8.276(0.099)	1.52(0.207)	0.008931	0.0019
	$CH_3CHO 2_{1,2} - 1_{1,1} A$	0.0138(0.003)	8.982(0.122)	1.41(0.446)	0.009204	0.0019
	CH ₃ CHO $2_{1,2} - 1_{1,1}$ F	0.0096(0.002)	9.066(0.076)	0.86(0.206)	0.01048	0.0022
	$CH_3CHO\ 2_{0,2} - 1_{0,1} E$ $CH_3CHO\ 2_{0,2} - 1_{0,1} E$	0.0278(0.002)	8.894(0.041)	1(0.11)	0.02602	0.0027
	CH ₃ CHO 2 _{0,2} = 1 _{0,1} L CH ₃ CHO 2 _{0,2} = 1 _{0,1} A	0.0219(0.002)	8.901(0.028)	0.653(0.065)	0.03156	0.0027
		0.0219(0.002)	8.88(0.091)	1.14(0.314)	0.03130	0.0027
	$CH_3CHO\ 2_{1,1} - 1_{1,0} E$	` '	8.97(0.062)	0.556(0.144)		
	CH ₃ CHO 2 _{1,1} - 1 _{1,0} A	0.00919(0.002)	` /	` /	0.01552	0.0034
700	$HCOOCH_34_{1,4} - 3_{1,3} E$	0.0101(0.002)	9.080(0.101)	0.783(0.206)	0.0121	0.0032
799	t-HCOOH $2_{1,2} - 1_{1,1}$	_	_	-	_	0.0039
	t-HCOOH $2_{0,2} - 1_{0,1}$	_	_	_	_	0.0044
	t-HCOOH $2_{1,1} - 1_{1,0}$	-	10.10(0.056)	- 700(0.1(0)	-	0.0062
	$H_2CCO\ 2_{1,2} - 1_{1,1}$	0.0206(0.003)	10.19(0.056)	0.799(0.168)	0.02428	0.0032
	$H_2CCO\ 2_{0,2} - 1_{0,1}$	0.0154(0.002)	10.13(0.032)	0.491(0.118)	0.02948	0.0034
	$H_2CCO\ 2_{1,1}-1_{1,0}$	0.0154(0.002)	10.13(0.032)	0.491(0.118)	0.02948	0.0034
	$CH_3OH 1_{0,1} - 0_{0,0} A$	0.314(0.004)	10.150(0)	0.47(0.007)	0.6288	0.0079
	$CH_3OH \ 1_{-0,1} - 0_{-0,0} \ E$	0.0212(0.004)	10.289(0.037)	0.416(0.095)	0.04803	0.0079
	$CH_3CN 2_1 - 1_1$	-	-	-	-	0.0034
	$CH_3CN 2_0 - 1_0$	0.0281(0.004)	9.466(0.08)	1.38(0.255)	0.01907	0.0034
	$CH_3CHO\ 2_{1,2} - 1_{1,1}\ A$	0.0108(0.002)	10.06(0.052)	0.517(0.078)	0.01961	0.0031
	$CH_3CHO\ 2_{1,2}-1_{1,1}\ E$	0.0089(0.002)	10.18(0.051)	0.445(0.125)	0.01879	0.0031
	2113 2113 21,2 11,1 E	······-/	()	0.523(0.059)	0.01077	0.0021

Table B2 - continued

Core	Line	Area (K-km s ⁻¹)	Vel	FWHM (km s-1)	$T_{ m mb}$ (K)	RMS (K)
	CH ₃ CHO 2 _{0,2} – 1 _{0,1} A	0.0306(0.002)	10.11(0.017)	0.456(0.03)	0.06307	0.0033
	$CH_3CHO\ 2_{1,1} - 1_{1,0} E$	0.0135(0.002)	10.1(0.036)	0.395(0.067)	0.0321	0.0035
	$CH_3CHO\ 2_{1,1} - 1_{1,0}\ A$	0.0151(0.002)	10.12(0.032)	0.475(0.069)	0.02982	0.0033
800	t-HCOOH $2_{1,2} - 1_{1,1}$	0.0212(0.005)	9.853(0.169)	1.5(0.404)	0.01333	0.0041
	t-HCOOH $2_{0,2} - 1_{0,1}$	0.0199(0.005)	10.16(0.144)	1.26(0.404)	0.01479	0.0052
	t-HCOOH $2_{1,1} - 1_{1,0}$	_	_	_	_	0.0066
	$H_2CCO\ 2_{1,2}-1_{1,1}$	0.0134(0.002)	10.35(0.066)	0.743(0.123)	0.01697	0.0034
	$H_2CCO\ 2_{0,2} - 1_{0,1}$	0.0179(0.003)	10.29(0.063)	0.843(0.124)	0.01991	0.0037
	$H_2CCO\ 2_{1,1}-1_{1,0}$	0.0181(0.002)	10.1(0.036)	0.596(0.077)	0.02859	0.0038
	$CH_3OH 1_{0,1} - 0_{0,0} A$	0.448(0.004)	10.19(0.003)	0.671(0.007)	0.6272	0.0075
	$CH_3OH \ 1_{-0,1} - 0_{-0,0} \ E$	0.0266(0)	10.26(0.022)	0.378(0.049)	0.06617	0.0075
	$CH_3CN 2_1 - 1_1$	_	_	_	_	0.0028
	$CH_3CN 2_0 - 1_0$	-	-	-	_	0.0028
	$CH_3CHO\ 2_{1,2}-1_{1,1}\ A$	0.0121(0.002)	10.2(0.054)	0.752(0.114)	0.01506	0.0025
	$CH_3CHO\ 2_{1,2} - 1_{1,1} E$	0.018(0.003)	10.3(0.115)	1.4(0.395)	0.01211	0.0027
	$CH_3CHO\ 2_{0,2}-1_{0,1}\ E$	0.0333(0.002)	10.16(0.021)	0.66(0.059)	0.04747	0.0032
	$CH_3CHO\ 2_{0,2}-1_{0,1}\ A$	0.0334(0.002)	10.22(0.025)	0.729(0.063)	0.04302	0.0032
	$CH_3CHO\ 2_{1,1} - 1_{1,0} E$	0.0162(0.002)	10.12(0.032)	0.558(0.076)	0.02728	0.0031
	$CH_3CHO\ 2_{1,1} - 1_{1,0}\ A$	0.0153(0.002)	10.25(0.036)	0.566(0.1)	0.02543	0.0034

Note. Errors reported in parentheses next to the number.

APPENDIX C: DETAILS ON COLUMN DENSITY CALCULATIONS

Below we outline the specific steps taken for each molecule in the column density calculations reported in Section 4.4.

C1 Methanol, CH₃OH

Methanol was detected in all 35 cores targeted and therefore we start with this molecule in our column density calculations. The collisional rates for the torsional ground states of the A and E states are available (Rabli & Flower 2010) and we use the RADEX code to calculate N, $T_{\rm ex}$, and τ values for the various transitions that were observed (Table C1; spectroscopic work detailed in Xu et al. 2008). We note that the τ value, or optical depth, of the line is not a fitted parameter but a prediction of RADEX for the given parameters and transition. The method for calculating N is as described in Scibelli & Shirley (2020), where a grid of RADEX models (2000 total) with Nvarying from $1 \times 10^{10} - 1 \times 10^{14} \,\mathrm{cm}^{-2}$ were run for each CH₃OH transition. In the calculations we are able to utilize the physical conditions already derived for each core, i.e. the average volume density, $n_{\rm H_2}$, and the kinetic temperature, T_k (columns 9 and 10 in Table 1). The difference in the observed line peak versus the line peak RADEX calculates was then minimized in order to find the best-fitting column density. In Fig. C1 an example is shown where the difference in radiation temperature divided by observed RMS, i.e. $|T_{\rm mb} - T_{\rm radex}|/\sigma_T$, is plotted against the RADEX-derived column density, N for each transition line. For the Yebes 40 m subsample there are five or four separate transitions minimized (two A-states and two or three E-states), and for the remaining cores two or three transitions minimized (depending on if the weaker $2_{0.2} - 1_{0.1}$ E transition was detected).

Because of the difference in beam sizes of the ARO 12 m and Yebes 40 m CH₃OH transitions (62 and 37 arcsec, respectively; see Table 2), we could constrain the source size, $\theta_{\rm src}$, and account for the true filling factor, f, when calculating the column density for our 15 core sub-sample. To do this, we ran our minimization procedure for $\theta_{\rm src}$ values from 23 to 65 arcsec (intervals of 0.5 arcsec) in order to

find a 'best-fit' $\theta_{\rm src}$ value for each core when the two bright CH₃OH $2_{0,2}-1_{0,1}$ A and CH₃OH $1_{0,1}-0_{0,0}$ A are closest in N (see Fig. C1). The $\theta_{\rm src}$ ranges from 26.5-56.5 arcsec where the median $\theta_{\rm src}$ is 38.5 arcsec (5 arcsec median deviation).

The error in the observed linewidth, Δv , as well as a 10 per cent error on $n_{\rm H_2}$ and T_k are propagated through our calculations to produce an error in N, $T_{\rm ex}$, and τ from our RADEX calculations (shown as dashed lines in Fig. C1). The volume density may be more uncertain because it was calculated as an average within the ARO 12 m beam and used for all transitions. Though, as was found in Scibelli & Shirley (2020), we find that even an order of magnitude difference in volume density leads to only a factor of \sim 2 in column density. In Table C1 we present the minimized column density for each transition separately, as well as a total column density, $N_{\rm sum}$, which we calculate from the sum of the brightest A and E states seen for all 35 cores in the sample, i.e. the 96 GHz $2_{0.2}-1_{0.1}$ A and $2_{-1.2}-1_{-1.1}$ E transitions.

While it is also possible with RADEX to use multiple molecular line transitions to constrain T_k and $n_{\rm H_2}$ for both methanol sub-state, this is only possible for the sub-sample of cores with Yebes 40 m data (see Appendix D). And, because specifically the A-state transitions are probed by different beams, this would lead to degeneracy if one were to try to also minimize to find a best-fitting pair of $n_{\rm H_2}$ and T_k in addition to the source size, $\theta_{\rm src}$. For these reasons we have chosen the standardized approach to minimize for N and (where we can) f while fixing $n_{\rm H_2}$ and T_k .

Additionally, since we have two A state transitions of this molecule with different E_u values, i.e. the $2_{0,2}-1_{0,1}$ at $E_u=7.0$ K and $1_{0,1}-1_{0,0}$ line at $E_u=2.3$ K, we also employ the CTEX method to calculate N and $T_{\rm ex}$ while applying the same corrected filling factors. We find the CTEX-determined column densities are lower by factors of $\sim 2-6$ than the RADEX-determined column densities. This is similar to what had been found in the L1544 pre-stellar core (Bizzocchi et al. 2014; Vastel et al. 2014). Looking at Table C1, it is evident that an LTE assumption (which assumes $\tau_v \ll 1$) breaks down as the 1-0 transitions have lower $T_{\rm ex}$ values than the 2-1 transitions, where in some cases $\tau \sim 1$.

Table C1. Column densities: RADEX results for CH₃OH.

Core # ¹ (Herschel)	$\theta_{ m src}$ arcsec	$N (10^{13} \text{ cm}^{-2})$	T _{ex} (K)	τ	$N (10^{13} \text{ cm}^{-2})$	T _{ex} (K)	τ	$N (10^{13} \text{ cm}^{-2})$	T _{ex} (K)	τ	N_{sum}^{2} (10 ¹³ cm ⁻²)
			$2_{0.2} - 1_{0.1}E$	0.422±0.003		$2_{0.2} - 1_{0.1} A$	0.202±0.013		$2_{-1,2} - 1_{-1,1}$	E	
54	38.5	$4.16^{+0.10}_{-0.10}$	$4.78^{+0.00}_{-0.00}$	$0.132^{+0.003}_{-0.003}$	$2.11^{+0.10}_{-0.15}$	$7.43^{+0.01}_{-0.02}$	$0.293^{+0.013}_{-0.020}$	$1.86^{+0.05}_{-0.15}$	6.66 ^{+0.00} _{-0.02}	$0.246^{+0.006}_{-0.019}$	$3.97^{+0.11}_{-0.21}$
67	38.5	$1.41^{+0.15}_{-0.20}$	$4.99^{+0.00}_{-0.01}$	$0.036^{+0.004}_{-0.005}$	$2.16^{+0.10}_{-0.15}$	$7.96^{+0.01}_{-0.02}$	$0.266^{+0.012}_{-0.018}$	$2.01^{+0.10}_{-0.15}$	$7.21^{+0.01}_{-0.01}$	$0.235^{+0.011}_{-0.017}$	$4.17^{+0.14}_{-0.21}$
130	38.5	=	-	_	$1.71^{+0.10}_{-0.15}$	$7.15^{+0.02}_{-0.03}$	$0.339^{+0.019}_{-0.028}$	$1.66^{+0.05}_{-0.15}$	$6.39^{+0.01}_{-0.02}$	$0.304^{+0.009}_{-0.026}$	$3.37^{+0.11}_{-0.21}$
231	38.5	_	-	_	$1.91^{+0.10}_{-0.20}$	$7.59^{+0.02}_{-0.04}$	$0.408^{+0.020}_{-0.040}$	$1.71^{+0.05}_{-0.15}$	$6.78^{+0.01}_{-0.03}$	$0.374^{+0.010}_{-0.031}$	$3.62^{+0.11}_{-0.25}$
256	38.5	- 0.15			$1.96^{+0.10}_{-0.15}$	$7.54^{+0.02}_{-0.03}$	$0.385^{+0.019}_{-0.028}$	$1.91^{+0.10}_{-0.15}$	$6.75^{+0.01}_{-0.02}$	$0.348^{+0.017}_{-0.026}$	$3.87^{+0.14}_{-0.21}$
264	38.5	$9.31^{+0.15}_{-0.00}$	$5.68^{+0.00}_{-0.00}$	$0.086^{+0.001}_{-0.000}$	$5.81^{+0.20}_{-0.45}$	$9.12^{+0.01}_{-0.02}$	$0.468^{+0.015}_{-0.034}$	$4.86^{+0.10}_{-0.25}$	$8.36^{+0.01}_{-0.01}$	$0.392^{+0.008}_{-0.019}$	$10.67^{+0.22}_{-0.51}$
317	38.0	$16.06^{+0.05}_{-0.30}$	$7.32^{+0.00}_{-0.01}$	$0.195^{+0.001}_{-0.004}$	$11.11^{+0.30}_{-0.65}$	$12.13^{+0.01}_{-0.02}$	$0.637^{+0.016}_{-0.035}$	$10.01^{+0.10}_{-0.35}$	$11.18^{+0.00}_{-0.01}$	$0.495^{+0.005}_{-0.016}$	$21.12^{+0.32}_{-0.74}$
321	56.5	$10.66^{+2.40}_{-2.60}$	$7.53^{+0.07}_{-0.08}$	$0.122^{+0.030}_{-0.031}$	$9.06^{+1.95}_{-1.85}$	$11.54^{+0.04}_{-0.04}$	$0.481^{+0.098}_{-0.095}$	$8.06^{+1.95}_{-1.85}$	$10.83^{+0.02}_{-0.02}$	$0.375^{+0.087}_{-0.083}$	$17.12^{+2.76}_{-2.62}$
326	51.5	$17.76^{+2.25}_{-2.15}$	$9.16^{+0.03}_{-0.03}$	$0.116^{+0.016}_{-0.015}$	$26.01^{+3.30}_{-2.55}$	$11.87^{+0.02}_{-0.02}$	$0.910^{+0.107}_{-0.084}$	$24.26^{+3.95}_{-3.45}$	$11.32^{+0.00}_{-0.00}$	$0.663^{+0.102}_{-0.090}$	50.27 +5.15
339	38.5	$11.76^{+0.45}_{-0.35}$	$7.06^{+0.01}_{-0.01}$	$0.091^{+0.004}_{-0.003}$	$6.41^{+0.00}_{-0.05}$	$13.19^{+0.00}_{-0.00}$	$0.286^{+0.000}_{-0.002}$	$5.76^{+0.10}_{-0.05}$	$12.13^{+0.00}_{-0.00}$	$0.223^{+0.004}_{-0.002}$	12.17 +0.10
344	38.5	$2.01^{+0.25}_{-0.30}$	$5.35^{+0.01}_{-0.01}$	$0.042^{+0.005}_{-0.006}$	$1.21^{+0.00}_{-0.05}$	$8.95^{+0.00}_{-0.01}$	$0.117^{+0.000}_{-0.005}$	$1.06^{+0.00}_{-0.00}$	$8.07^{+0.00}_{-0.00}$	$0.099^{+0.000}_{-0.000}$	$2.27^{+0.00}_{-0.05}$
355	38.5	$4.96^{+0.25}_{-0.25}$	$4.57^{+0.01}_{-0.01}$	$0.164^{+0.008}_{-0.008}$	$3.16^{+0.30}_{-0.45}$	$7.17^{+0.05}_{-0.07}$	$0.684^{+0.060}_{-0.089}$	$2.76^{+0.20}_{-0.35}$	$6.40^{+0.03}_{-0.05}$	$0.585^{+0.039}_{-0.068}$	$5.92^{+0.36}_{-0.57}$
398	38.5	-	-		$0.51^{+0.00}_{-0.00}$	$6.62^{+0.00}_{-0.00}$	$0.118^{+0.000}_{-0.000}$	$0.41^{+0.00}_{-0.05}$	$5.92^{+0.00}_{-0.01}$	$0.100^{+0.000}_{-0.012}$	$0.92^{+0.0}_{-0.05}$
413	39.0	$2.81^{+0.25}_{-0.25}$	$4.78^{+0.01}_{-0.01}$	$0.079^{+0.007}_{-0.007}$	$2.76^{+0.15}_{-0.30}$	$7.68^{+0.02}_{-0.04}$	$0.402^{+0.021}_{-0.041}$	$2.56^{+0.10}_{-0.20}$	$6.88^{+0.01}_{-0.02}$	$0.352^{+0.013}_{-0.026}$	$5.32^{+0.18}_{-0.36}$
414	38.5	_	-	-	$0.91^{+0.10}_{-0.05}$	$5.30^{+0.02}_{-0.01}$	$0.310^{+0.033}_{-0.016}$	$0.71^{+0.05}_{-0.05}$	$4.78^{+0.01}_{-0.01}$	$0.324^{+0.022}_{-0.022}$	$1.62^{+0.11}_{-0.07}$
479	38.5	=	=	-	$5.11^{+0.20}_{-0.40}$	$8.90^{+0.01}_{-0.02}$	$0.530^{+0.020}_{-0.039}$	$4.61^{+0.05}_{-0.25}$	$8.24^{+0.00}_{-0.01}$	$0.431^{+0.005}_{-0.022}$	$9.72^{+0.21}_{-0.47}$
491	38.5	-	-	-	$1.16^{+0.05}_{-0.05}$	$7.28^{+0.01}_{-0.01}$	$0.185^{+0.008}_{-0.008}$	$1.01^{+0.00}_{-0.05}$	$6.50^{+0.00}_{-0.01}$	$0.150^{+0.000}_{-0.007}$	$2.17^{+0.05}_{-0.07}$
504	33.0	$5.66^{+0.35}_{-0.35}$	$5.23^{+0.01}_{-0.01}$	$0.151^{+0.010}_{-0.010}$	$6.76^{+0.60}_{-1.20}$	$8.28^{+0.04}_{-0.08}$	$0.989^{+0.081}_{-0.159}$	$5.91^{+0.40}_{-0.70}$	$7.52^{+0.02}_{-0.04}$	$0.790^{+0.049}_{-0.085}$	$12.67^{+0.72}_{-1.39}$
543	38.5	- 1.1.45	-		$1.51^{+0.10}_{-0.10}$	$6.80^{+0.02}_{-0.02}$	$0.330^{+0.021}_{-0.021}$	$1.36^{+0.05}_{-0.10}$	$5.98^{+0.01}_{-0.02}$	$0.298^{+0.010}_{-0.021}$	$2.87^{+0.11}_{-0.14}$
615	36.5	$4.56^{+1.45}_{-1.70}$	$4.56^{+0.04}_{-0.04}$	$0.107^{+0.034}_{-0.040}$	$4.31^{+1.30}_{-1.55}$	$7.50^{+0.17}_{-0.23}$	$0.797^{+0.212}_{-0.267}$	$3.96^{+1.10}_{-1.35}$	$6.62^{+0.12}_{-0.16}$	$0.674^{+0.166}_{-0.214}$	$8.27^{+1.7}_{-2.06}$
627	40.5	$4.16^{+1.05}_{-1.20}$	$4.77^{+0.03}_{-0.03}$	$0.102^{+0.026}_{-0.030}$	$1.96^{+0.05}_{-0.15}$	$8.14^{+0.01}_{-0.04}$	$0.420^{+0.010}_{-0.030}$	$1.76^{+0.10}_{-0.10}$	$7.16^{+0.02}_{-0.02}$	$0.392^{+0.021}_{-0.021}$	$3.72^{+0.11}_{-0.18}$
642	38.5	_	-	-	$0.46^{+0.00}_{-0.05}$	$7.24^{+0.00}_{-0.02}$	$0.117^{+0.000}_{-0.012}$	$0.41^{+0.05}_{-0.00}$	$6.33^{+0.01}_{-0.00}$	$0.098^{+0.012}_{-0.000}$	$0.87^{+0.05}_{-0.05}$
656	38.5	$2.26^{+1.45}_{-1.75}$	$4.34^{+0.06}_{-0.07}$	$0.104^{+0.067}_{-0.080}$	$1.81^{+0.85}_{-1.05}$	$6.64^{+0.18}_{-0.25}$	$0.540^{+0.230}_{-0.303}$	$1.66^{+0.85}_{-1.00}$	$5.97^{+0.15}_{-0.20}$	$0.507^{+0.234}_{-0.296}$	$3.47^{+1.2}_{-1.45}$
657	38.5	-	-	-	$1.21^{+0.05}_{-0.10}$	$6.63^{+0.01}_{-0.02}$	$0.280^{+0.011}_{-0.022}$	$1.06^{+0.00}_{-0.10}$	$5.90^{+0.00}_{-0.02}$	$0.239^{+0.000}_{-0.022}$	$2.27^{+0.05}_{-0.14}$
658	38.5	$5.16^{+2.10}_{-2.55}$	$4.24^{+0.06}_{-0.07}$	$0.166^{+0.067}_{-0.082}$	$3.71^{+1.40}_{-1.85}$	$6.72^{+0.24}_{-0.37}$	$1.039^{+0.336}_{-0.484}$	$3.31^{+1.35}_{-1.75}$	$5.94^{+0.20}_{-0.30}$	$0.929^{+0.323}_{-0.461}$	$7.02^{+1.94}_{-2.55}$
709	33.5	$14.26^{+0.25}_{-0.50}$	$5.92^{+0.01}_{-0.02}$	$0.214^{+0.004}_{-0.008}$	$7.81^{+0.35}_{-0.65}$	$10.58^{+0.03}_{-0.05}$	$0.591^{+0.024}_{-0.045}$	$6.61^{+0.25}_{-0.45}$	$9.38^{+0.02}_{-0.03}$	$0.476^{+0.017}_{-0.030}$	$14.42^{\ +0.43}_{\ -0.79}$
715	26.5	$6.26^{+1.65}_{-1.85}$	$5.87^{+0.05}_{-0.05}$	$0.085^{+0.023}_{-0.025}$	$5.31^{+1.70}_{-1.75}$	$11.38^{+0.16}_{-0.19}$	$0.470^{+0.136}_{-0.146}$	$4.76^{+1.50}_{-1.55}$	$10.09^{+0.13}_{-0.15}$	$0.382^{+0.109}_{-0.118}$	$10.07^{\ +2.27}_{\ -2.34}$
739	38.5	-	-	-	$2.46^{+0.15}_{-0.25}$	$7.18^{+0.02}_{-0.03}$	$0.412^{+0.024}_{-0.040}$	$2.11^{+0.05}_{-0.15}$	$6.54^{+0.01}_{-0.01}$	$0.332^{+0.008}_{-0.023}$	$4.57^{+0.16}_{-0.29}$
746	35.0	$4.26^{+0.35}_{-0.30}$	$4.99^{+0.01}_{-0.01}$	$0.093^{+0.008}_{-0.007}$	$5.46^{+0.40}_{-0.75}$	$8.34^{+0.04}_{-0.07}$	$0.728^{+0.049}_{-0.091}$	$4.91^{+0.30}_{-0.55}$	$7.47^{+0.03}_{-0.04}$	$0.620^{+0.035}_{-0.063}$	$10.37^{+0.5}_{-0.93}$
747	38.5	$7.71^{+0.50}_{-0.50}$	$4.59^{+0.01}_{-0.02}$	$0.184^{+0.012}_{-0.012}$	$3.56^{+0.25}_{-0.45}$	$7.83^{+0.05}_{-0.09}$	$0.642^{+0.040}_{-0.072}$	$3.06^{+0.20}_{-0.35}$	$6.75^{+0.03}_{-0.06}$	$0.554^{+0.033}_{-0.056}$	$6.62^{+0.32}_{-0.57}$
752	46.5	$8.36^{+0.05}_{-0.10}$	$4.65^{+0.00}_{-0.00}$	$0.189^{+0.001}_{-0.002}$	$4.21^{+0.30}_{-0.50}$	$8.15^{+0.05}_{-0.09}$	$0.564^{+0.036}_{-0.059}$	$3.91^{+0.25}_{-0.45}$	$7.01^{+0.04}_{-0.07}$	$0.526^{+0.030}_{-0.053}$	$8.12^{+0.39}_{-0.67}$
768	48.0	$1.96^{+0.35}_{-0.35}$	$5.00^{+0.01}_{-0.01}$	$0.055^{+0.010}_{-0.010}$	$1.96^{+0.05}_{-0.15}$	$8.09^{+0.01}_{-0.02}$	$0.258^{+0.006}_{-0.019}$	$1.81^{+0.05}_{-0.05}$	$7.28^{+0.00}_{-0.00}$	$0.218^{+0.006}_{-0.006}$	$3.77^{+0.07}_{-0.16}$
780	38.5	$3.66^{+0.30}_{-0.40}$	$4.54^{+0.01}_{-0.01}$	$0.092^{+0.008}_{-0.010}$	$1.56^{+0.10}_{-0.15}$	$7.16^{+0.02}_{-0.03}$	$0.335^{+0.020}_{-0.030}$	$1.41^{+0.10}_{-0.10}$	$6.37^{+0.02}_{-0.02}$	$0.301^{+0.020}_{-0.020}$	$2.97^{+0.14}_{-0.18}$
799	41.0	$3.81^{+0.25}_{-0.25}$	$4.52^{+0.01}_{-0.01}$	$0.127^{+0.008}_{-0.008}$	$3.81^{+0.40}_{-0.65}$	$7.52^{+0.07}_{-0.11}$	$0.911^{+0.086}_{-0.136}$	$3.41^{+0.30}_{-0.55}$	$6.65^{+0.05}_{-0.08}$	$0.825^{+0.065}_{-0.116}$	$7.22^{+0.5}_{-0.85}$
800	29.5	$7.16_{-0.10}^{+0.15}$	$5.76^{+0.00}_{-0.00}$	$0.147^{+0.003}_{-0.002}$	$8.56^{+0.65}_{-1.20}$	$9.92^{+0.04}_{-0.07}$	$0.953^{+0.066}_{-0.120}$	$7.51^{+0.40}_{-0.80}$	$8.91^{+0.02}_{-0.04}$	$0.758^{+0.037}_{-0.073}$	$16.07 {}^{+0.76}_{-1.44}$
			$1_{0,1} - 0_{0,0} A$			$1_{-0,1} - 0_{-0,0}$ E	E				
264	38.5	$5.81^{+0.25}_{-0.25}$	$6.84^{+0.02}_{-0.02}$	$0.195^{+0.008}_{-0.008}$	-	-	-	-	-		-
317	38.0	$11.11^{+0.45}_{-0.40}$	$8.50^{+0.03}_{-0.03}$	$0.310^{+0.011}_{-0.010}$	$14.46^{+0.60}_{-0.50}$	$7.52^{+0.05}_{-0.04}$	$0.388^{+0.014}_{-0.011}$	-	_	=	-
321	56.5	$9.06^{+0.40}_{-0.35}$	$7.90^{+0.03}_{-0.02}$	$0.232^{+0.009}_{-0.008}$	$9.36^{+0.35}_{-0.20}$	$7.43^{+0.03}_{-0.02}$	$0.239^{+0.008}_{-0.005}$	=	=	=	=
326	51.5	$26.01^{+0.95}_{-0.75}$	$8.88^{+0.03}_{-0.03}$	$0.462^{+0.014}_{-0.011}$	$18.51^{+0.55}_{-0.30}$	$9.94^{+0.03}_{-0.01}$	$0.348^{+0.009}_{-0.005}$	-	-	=	_
413	39.0	$2.76^{+0.10}_{-0.10}$	$6.35^{+0.01}_{-0.01}$	$0.165^{+0.006}_{-0.006}$	$3.46^{+0.65}_{-0.70}$	$4.34^{+0.06}_{-0.06}$	$0.203^{+0.034}_{-0.038}$	-	-	-	-
504	33.0	$6.81^{+0.20}_{-0.10}$	$6.66^{+0.01}_{-0.01}$	$0.380^{+0.010}_{-0.005}$	$5.61^{+0.50}_{-0.50}$	$4.92^{+0.04}_{-0.05}$	$0.320^{+0.025}_{-0.026}$	-	-	-	_
615	36.5	$4.31^{+0.05}_{-0.05}$	$6.43^{+0.01}_{-0.01}$	$0.320^{+0.003}_{-0.003}$	$4.61^{+0.50}_{-0.50}$	$4.32^{+0.05}_{-0.05}$	$0.340^{+0.032}_{-0.032}$	-	-	-	-
627	40.5	$1.96^{+0.05}_{-0.05}$	$6.91^{+0.01}_{-0.01}$	$0.169^{+0.004}_{-0.004}$	$4.81^{+0.65}_{-0.65}$	$4.60^{+0.07}_{-0.08}$	$0.367^{+0.041}_{-0.042}$	=	=	=	=
709	33.5	$7.76^{+0.25}_{-0.20}$	$8.18^{+0.02}_{-0.02}$	$0.288^{+0.008}_{-0.006}$	$12.96^{+0.60}_{-0.50}$	$5.91^{+0.05}_{-0.04}$	$0.444^{+0.017}_{-0.014}$	=	=	=	=
715	26.5	$5.31^{+0.30}_{-0.20}$	$8.57^{+0.04}_{-0.03}$	$0.204^{+0.010}_{-0.007}$	$2.56^{+0.65}_{-0.65}$	$5.45^{+0.14}_{-0.15}$	$0.106^{+0.024}_{-0.025}$	=	=	=	=
746	35.0	$5.41^{+0.15}_{-0.10}$	$6.80^{+0.02}_{-0.01}$	$0.320^{+0.008}_{-0.005}$	$5.21^{+0.85}_{-0.85}$	$4.60^{+0.06}_{-0.07}$	$0.309^{+0.043}_{-0.045}$	-	-	-	_
752	46.5	$4.21^{+0.05}_{-0.00}$	$7.58^{+0.01}_{-0.00}$	$0.220^{+0.002}_{-0.000}$	$9.16^{+0.50}_{-0.40}$	$4.51^{+0.03}_{-0.03}$	$0.410^{+0.017}_{-0.014}$	-	-	-	-
768	48.0	$1.96^{+0.10}_{-0.05}$	$6.46^{+0.01}_{-0.01}$	$0.113^{+0.005}_{-0.003}$	$1.76^{+0.40}_{-0.45}$	$4.43^{+0.05}_{-0.05}$	$0.102^{+0.022}_{-0.025}$	-	-	-	-
799	41.0	$3.81^{+0.00}_{-0.00}$	$6.52^{+0.00}_{-0.00}$	$0.376^{+0.000}_{-0.000}$	$3.51^{+0.60}_{-0.65}$	$4.24^{+0.07}_{-0.08}$	$0.350^{+0.051}_{-0.057}$	=	=	=	=
800	29.5	$8.56^{+0.25}_{-0.10}$	$7.65^{+0.02}_{-0.01}$	$0.414^{+0.010}_{-0.004}$	$4.76_{-0.45}^{+0.50}$	$5.61^{+0.08}_{-0.08}$	$0.249^{+0.023}_{-0.021}$	_		_	

Note. The cores observed with both the ARO 12 m and Yebes 40 m are bolded. We chose to calculate the total column density, N_{sum} , by summing the $2_{0,2} - 1_{0,1}$ A and $2_{-1,2} - 1_{-1,1}$ E column densities. Errors quoted as '0.00' or '0.000' are < 0.005 or < 0.0005, respectively.

Table C2. Column densities: CH₃CHO A.

Core #1	$\theta_{ m src}$	CH ₃ CH	Ю А
(Herschel)	arcsec	$N (\times 10^{12} \text{ cm}^{-2})$	$T_{\mathrm{ex}}\left(\mathbf{K}\right)$
54	38.5	< 1.70	5.55
67	38.5	$0.68^{+0.61}_{-0.16}$	5.55 ± 0.9
130	38.5	< 2.05	5.55
231	38.5	< 1.51	5.55
256	38.5	< 1.97	5.55
264	38.5	$1.63^{+0.20}_{-0.20}$	$5.78^{\ +0.34}_{\ -0.44}$
317	38.0	$5.63^{+0.37}_{-0.38}$	$6.83_{-0.08}^{+0.08}$
321	56.5	$3.70^{+0.21}_{-0.21}$	$6.28 ^{+0.13}_{-0.14}$
326	51.5	$8.08^{+0.17}_{-0.17}$	$6.24^{+0.11}_{-0.11}$
339	38.5	< 2.07	5.55
344	38.5	< 1.46	5.55
355	38.5	< 1.79	5.55
398	38.5	< 1.79	5.55
413	39.0	$1.49^{+0.23}_{-0.24}$	$4.97^{\ +0.16}_{\ -0.22}$
414	38.5	< 2.09	5.55
479	38.5	< 2.38	5.55
491	38.5	< 1.75	5.55
504	33.0	$2.21 ^{+0.17}_{-0.14}$	$5.24^{\ +0.50}_{\ -0.62}$
543	38.5	< 1.94	5.55
615	36.5	$2.10^{+0.18}_{-0.17}$	$4.54^{\ +0.22}_{\ -0.28}$
627	40.5	$1.92^{+0.19}_{-0.18}$	$4.27^{\ +0.17}_{\ -0.23}$
642	38.5	< 2.31	5.55
656	38.5	< 1.56	5.55
657	38.5	< 2.03	5.55
658	38.5	$0.59 ^{+0.52}_{-0.14}$	$5.55^{+0.92}_{-0.92}$
709	33.5	$4.65^{+0.41}_{-0.41}$	$5.74^{+0.06}_{-0.07}$
715	26.5	$2.69^{+0.30}_{-0.29}$	$4.45^{\ +0.23}_{\ -0.31}$
739	38.5	< 1.84	5.55
746	35.0	$4.27 ^{\ +0.44}_{\ -0.45}$	$4.68 ^{+0.04}_{-0.04}$
747	38.5	< 2.37	5.55
752	46.5	$1.94 ^{+0.16}_{-0.16}$	$5.88^{\ +0.22}_{\ -0.27}$
768	48.0	$1.74^{+0.25}_{-0.26}$	$7.07^{\ +0.23}_{\ -0.28}$
780	38.5	< 1.72	5.55
799	41.0	$1.79 ^{+0.14}_{-0.13}$	$4.52^{+0.21}_{-0.25}$
800	29.5	$3.95^{+0.32}_{-0.32}$	$6.71^{+0.33}_{-0.38}$

Note. ¹ The cores observed with both the ARO 12 m and Yebes 40 m are bolded, their values calculated from the RD method. For the italicized cores 67 and 658, the values are calculated with the LTE method based on the single A state transition detected with the ARO 12 m, assuming the median CH₃CHO A-state $T_{\rm ex}$ value of 4.94 K. For the remaining cores, a 3σ upper limit is calculated via the LTE method.

C2 Acetaldehyde, CH₃CHO

For the total 35 cores from the initial ARO 12 m survey, column densities or upper limits were derived for CH₃CHO given our observations of the $5_{0.5} - 4_{0.4}$ transitions with $E_u/k \sim 14$ K. We note that original laboratory spectroscopic work is detailed in Kleiner, Lovas & Godefroid (1996). Since there are no calculated collisional rate coefficients for this molecule, we are not able to use RADEX. For the 15 cores with Yebes 40 m observations, there are additional transitions with varying E_u/k values from $\sim 3 - 5$ K, which allows us to use the RD method, which we chose to employ for the A-state transitions in order to robustly derive N and $T_{\rm ex}$ (see Fig.

12 and Table C2). Overall, we find N for CH₃CHO A ranges from $0.59-8.08\times10^{12}\,\mathrm{cm^{-2}}$, with a median value (and median standard deviation) of $2.10\pm0.61\times10^{12}\,\mathrm{cm^{-2}}$. Additionally, T_{ex} ranges from 4.27-7.07 with a median value of $5.55\,\mathrm{K}$ and median standard deviation of $0.9\,\mathrm{K}$. This is within the range but slightly higher than the T_{ex} values derived using the CTEX method for the Taurus cores, which range from $3.09-5.39\,\mathrm{K}$, with a median of $3.57\,\mathrm{K}$ (Scibelli & Shirley 2020). For the starless core L1521E the T_{ex} value for CH₃CHO A, derived using the same RD method but with different transitions, is $\sim 4.5\,\mathrm{K}$ (Scibelli et al. 2021), slightly lower than the median for the Perseus core sample.

For cores 67 and 658, for which CH₃CHO was detected with the ARO 12 m at a $\sigma_{T_{\rm mb}} = 2.5$ mK limit and no Yebes 40 m data is available, the *N* values are calculated with the LTE method based on the single A state transition detected with the ARO 12 m, assuming the median CH₃CHO A $T_{\rm ex}$ value of 5.55 K. For these cores *N* for CH₃CHO A is $\sim 0.7 \times 10^{12} \, {\rm cm}^{-2}$. For the remaining cores, a 3σ upper limit is calculated via the LTE method, with the same mean $T_{\rm ex}$ assumed (see Table C2).

Because we need to worry again about the differences in beam sizes between the ARO 12 m and Yebes 40 m CH₃CHO transitions, we take this into account by assuming the same source size, $\theta_{\rm src}$, that was derived for CH₃OH, as these molecules are believed to trace each other spatially and has been done for the Taurus core L1521E (Scibelli et al. 2021) and predicted by the chemical models of Vasyunin et al. (2017). The $\theta_{\rm src}$ is then plugged into equation (1), where $\theta_{\rm beam}$ for these A-state transitions of CH₃CHO are listed in Table 2, in order to account for the filling factor, f. We note that if f is set to 1 for all transitions, the N values would decrease by factors from \sim 1.4 to 3.3.

C3 Ketene, H₂CCO

A nearly prolate symmetric rotor, H_2CCO is a molecule with no calculated collisional rates, whose laboratory spectroscopy at the frequencies cited in this study is detailed in Brown et al. (1990). In our Yebes 40m sub-sample, three transitions were observed with different E_u/k values (15.9, 2.9, and 16 K). However, the two transitions with the similar E_u/k values of 15.9 K and 16.0 K are ortho species (meaning $K_a = \text{odd}$ with a statistical weight of 3) and the other transition is a para species (meaning $K_a = \text{even}$ with a statistical weight of 1). Thus, we use the LTE method to find N for both ortho and para species separately and assume three different excitation temperatures at 5 K, 10 K, and 20 K (see Table C3 for all estimates).

There is not a straightforward reference to guide an estimate for a true filling factor for H₂CCO since each transition was observed with the Yebes 40 m and has roughly the same beam size, and we know for the pre-stellar core L1544 the spatial distribution of H₂CCO does not follow that of CH₃OH (Spezzano et al. 2017). We therefore assume f=1 to find, for $T_{\rm ex}$ of 10 K, N(o-H₂CCO) range from $1.8-7.6\times10^{12}\,{\rm cm}^{-2}$ and N(p-H₂CCO) range from $0.8-4.4\times10^{12}\,{\rm cm}^{-2}$. Even so, an f=1 assumption is still likely underestimating N and if we do assume the average f value from our CH₃OH analysis (f=0.4) this would increase our N values by a factor of 2.5. These column densities are still found to be on average lower than updated estimates at the dust peak of pre-stellar core L1544, where Jiménez-Serra et al. (2021) find for H₂CCO $T_{\rm ex}=5-6$ K and $N=1.5\pm0.2\times10^{13}\,{\rm cm}^{-2}$.

Under LTE assumptions the ortho-to-para ratios for the cores in most cases are > 1, with a median value of 2.4. In some Taurus cores, such as TMC-1 and L1689B, this ratio is close to the statistical ratio

Table C3. Column densities: The 5-atom COMs, H₂CCO, and t-HCOOH.

Core # (Herschel)	$T_{\rm ex}$ (K)	H_2 CCO o- (p-) $N \times 10^{12} \text{ cm}^{-2}$	t-HCOOH $N \times 10^{12} \text{ cm}^{-2}$	$T_{\rm ex}$ (K)	H_2 CCO o- (p-) $N \times 10^{12} \text{ cm}^{-2}$	t-HCOOH $N \times 10^{12} \text{ cm}^{-2}$	$T_{\mathrm{ex}}\left(\mathrm{K}\right)$	H_2 CCO o- (p-) $N \times 10^{12} \text{ cm}^{-2}$	t-HCOOH $N \times 10^{12} \text{ cm}^{-2}$
264	5	<5.0 (< 0.8)	14.7	10	< 1.8 (< 1.1)	15.1	20	< 2.0 (2.3)	27.4
317	5	5.6 (1.1)	1.3	10	2.0 (1.5)	1.8	20	2.2 (3.2)	3.7
321	5	12.8 (0.6)	< 1.5	10	4.7 (0.8)	< 2.0	20	4.3 (1.7)	< 4.3
326	5	20.8 (2.5)	4.1	10	7.6 (3.4)	5.7	20	8.5 (7.3)	12.1
413	5	7.7 (0.7)	< 1.5	10	2.8 (0.9)	< 2.1	20	3.1 (2.0)	< 4.3
504	5	6.8 (1.1)	1.3	10	2.5 (1.6)	1.8	20	2.7(3.4)	3.7
615	5	5.1(3.3)	< 2.2	10	1.8 (4.4)	< 3.1	20	2.1 (9.5)	< 6.7
627	5	7.7 (0.7)	< 2.0	10	2.8 (1.0)	< 2.9	20	3.1 (2.2)	< 6.1
709	5	20.1 (2.3)	2.2	10	7.3 (3.1)	3.1	20	8.1 (6.7)	6.7
715	5	10.6 (1.8)	3.0	10	3.9 (2.5)	4.2	20	4.3 (5.3)	8.8
746	5	16.5 (1.6)	2.5	10	6.0 (2.2)	3.5	20	6.7 (4.8)	7.5
752	5	6.2 (1.9)	1.1	10	2.3 (2.6)	1.5	20	2.5 (5.6)	3.2
768	5	10.1 (0.9)	< 1.1	10	3.7 (1.2)	< 1.6	20	4.1 (2.6)	< 3.4
799	5	8.7 (1.2)	< 1.7	10	3.2 (1.6)	< 2.4	20	3.5 (3.6)	< 5.1
800	5	7.8 (1.4)	2.5	10	2.8 (1.9)	3.5	20	3.1 (4.2)	7.5

Note. The ortho states and para states (in parentheses) for H_2CCO are calculated separately, where N based on each ortho transition ($2_{1,2} - 1_{1,1}$ o- and $2_{1,1} - 1_{1,0}$ o-) is done using a simultaneous fit to both lines. Estimates for t-HCOOH calculated from the $2_{0,2} - 1_{0,1}$ transition, with the exception of core 264 for which only the $2_{1,2} - 1_{1,1}$ transition was detected and thus used in the LTE calculation.

Table C4. Column densities: RADEX results for CH₃CN.

	CH ₃ CN 2	$2_1 - 1_1$	CH ₃ CN 2 ₀		
Core # (<i>Herschel</i>)	$(\times 10^{12} \text{ cm}^{-2})$	<i>T</i> _{ex} (K)	$N \times 10^{12} \text{ cm}^{-2}$	<i>T</i> _{ex} (K)	$N_{\rm avg} \ (\times 10^{12} \ {\rm cm}^{-2})$
264	_	_	$0.171^{\ +0.02}_{\ -0.02}$	8.66^{a}	_
317	_	_	$0.106^{+0.03}_{-0.03}$	12.3^{a}	_
321	_	_	< 0.05	12.5	_
326	$0.271^{+0.04}_{-0.06}$	$13.2^{\ +0.6}_{\ -0.6}$	$0.326^{+0.05}_{-0.04}$	13.2^{a}	0.298(0.028)
413	$0.336^{+0.01}_{-0.03}$	$6.54^{+1.9}_{-1.9}$	$0.196^{+0.02}_{-0.01}$	6.53^{a}	0.266(0.070)
504	_	-	$0.196^{+0.02}_{-0.02}$	7.39^{a}	_
615	_	_	< 0.05	5.94	_
627	_	_	$0.166^{+0.02}_{-0.02}$	6.30^{a}	_
709	$0.766^{+0.01}_{-0.04}$	$8.71^{+3.6}_{-3.6}$	$0.401 ^{+0.03}_{-0.02}$	8.70^{a}	0.584(0.182)
715	$0.351^{+0.03}_{-0.06}$	$9.22^{+4.4}_{-4.4}$	$0.251^{+0.03}_{-0.02}$	9.22^{a}	0.301(0.050)
746	$0.146^{+0.02}_{-0.03}$	$7.02^{+2.1}_{-2.1}$	$0.221 {}^{+0.02}_{-0.01}$	7.02^{a}	0.183(0.038)
752	$0.396^{+0.01}_{-0.01}$	$5.57^{+2.0}_{-2.0}$	$0.151^{+0.02}_{-0.01}$	5.57 ^a	0.274(0.122)
768	$0.201_{-0.03}^{+0.02}$	$7.14^{+2.2}_{-2.2}$	$0.076^{+0.01}_{-0.01}$	7.14^{a}	0.139(0.063)
799	_	-	$0.081^{+0.01}_{-0.02}$	5.81^{a}	_
800	_	_	< 0.05	8.67	_

Note.^a RADEX associated errors for these $T_{\rm ex}$ values are < 0.001.

of 3 (Ohishi et al. 1991; Bacmann et al. 2012) and in others, such as L1517B, they find a value of \sim 1 (Megías et al. 2023). For ratios > 3 this is consistent with the 'high temperature limit' whereas for ratios < 3 this would be consistent with equilibrium at 10 K (Ohishi et al. 1991). These ratios for the Perseus cores should be taken lightly, however, since we are assuming LTE and f=1. It is also likely f varies from source to source (as it does for CH₃OH) and for the different ortho and para species of H₂CCO, which can alter the true ortho-to-para ratio.

C4 Formic acid, t-HCOOH

There are three energetically favourable 2-1 transitions available to analyse for the *trans* isomer of formic acid, t-HCOOH, from the

Yebes 40 m observations (Table 2; spectroscopic work detailed in Bellet et al. 1971; Winnewisser et al. 2002). We first attempted to use the CTEX method to constrain the excitation temperature, $T_{\rm ex}$. This method was unsuccessful, however, because unlike H₂CCO the E_u/k values for these transitions do not span a wide enough range, i.e. values of 3.2 K, 6.2 K, and 6.5 K. Instead, we implement the LTE method to calculate N (assuming f=1) by using the more favourable $2_{0,2}-1_{0,1}$ transition detected in all cores, with the exception of core 264 for which only the $2_{1,2}-1_{1,1}$ transition was detected and thus used in the LTE calculation. We calculate N for three different $T_{\rm ex}$ values at 5 K, 10 K, and 20 K (Table C3). For the $T_{\rm ex}=10$ K case N values range from $1.5-15\times10^{12}$ cm⁻². We note that, similar to H₂CCO, if we instead assume the average f value from our CH₃OH analysis this would increase N by a factor of 2.5.

Compared to pre-stellar core L1544, where Vastel et al. (2014) find $N=5\times 10^{11}~\rm cm^{-2}$ for a $T_{\rm ex}=10~\rm K$ and Jiménez-Serra et al. (2021) similarly find 4.8 \pm 0.9 $\times 10^{11}~\rm cm^{-2}$ for $T_{\rm ex}=12.6\pm6.9~\rm K$, the Perseus cores with t-HCOOH detections have an order of magnitude higher N values (\sim a few $\times 10^{12}~\rm cm^{-2}$ for f=1).

C5 Methyl cyanide, CH3CN

The RADEX method is used for CH₃CN, since there are collisional rates calculated (Green 1986). Following the standardized procedure described for CH₃OH (Section C1), we use the two 2-1 transitions (Table 2; spectroscopic work detailed in Kukolich 1982) to minimize over a grid of RADEX calculations to find the best fit N values while fixing the volume density, $n_{\rm H_2}$, and the kinetic temperature, T_k (columns 9 and 10 in Table 1). Since these transitions were observed close in frequency with the Yebes 40 m (Fig. 7) and the spatial distribution of this N-bearing molecule is not known in these sources, we assume f=1 while constraining N for this 15 core sub-sample (see Table C4 and Fig. C2). If one were to assume the average f=0.4 (i.e. from our CH₃OH analysis), we find this can increase N by factors of 2.4–2.5.

In cores 264, 317, 504, 627, and 799 only the brighter $2_0 - 1_0$ transitions is detected above 3σ and used to constrain N. We note that for the remaining cores with constraints for both 2-1 transitions. the best-fitting N value calculated for each separate transition differ at minimum by a factor of 1.2 for core 326 and at maximum a factor of 2.6 for core 768 (see Fig. C2), and report an average N_{avg} value in Table C4. For cores 326 and 746 the $2_0 - 1_0$ line finds a higher N value whereas for the rest of the cores a higher N is found from the $2_1 - 1_1$ fit. It is shown in Fig. 7 that the disagreement is likely due to the deviation in peak intensity. For core 326 the $2_0 - 1_0$ and $2_1 - 1_1$ ratio is 2.8 whereas in core 768 the ratio is 1.5. Note that for the seven cores with more than two transitions, we do explore simultaneous minimization with varying $n_{\rm H_2}$ and T_k and find N values differ by no more than factors of < 3 from our values in Table C4 (see Appendix D for more detail). For cores 321, 615, and 800, where CH₃CN is not detected at $> 3\sigma$ we report an upper limit for N from our RADEX grid where the peak $2_0 - 1_0$ intensity from the model equals 3σ .

C6 Vinyl cyanide, CH₂CHCN

For the large N-bearing molecule CH₂CHCN, an LTE method needed to be used. We first attempted the CTEX method on core 413 as two transitions of CH₂CHCN were detected, the $4_{1,4}-3_{1,3}$ and $4_{0,4}-3_{0,3}$ lines (Table 2; spectroscopic work detailed in Stolze & Sutter 1985; Cazzoli & Kisiel 1988). However, due to their similar upper energies at $E_u=6.6\,\mathrm{K}$ and $E_u=4.5\,\mathrm{K}$, respectively, this method was unable to constrain an excitation temperature, T_{ex} . Instead, for this N-bearing species we assume the T_{ex} is comparable to CH₃CN. In Table C5 are the predicted column densities and 3σ upper limits based on LTE calculations assuming, for the Yebes 40 m 15 core sub-sample, that core's CH₃CN T_{ex} value, and, for the remaining cores with only ARO 12 m constraints, the median CH₃CN T_{ex} value from that 15 core sub-sample.

For the cores with at least one transition detected from the Yebes 40 m data, the observed peak intensity from the $4_{1,4} - 3_{1,3}$ (for cores 264 and 413), $4_{0,4} - 3_{0,3}$ (for cores 709 and 746) or $4_{2,3} - 3_{2,2}$ (core 715) transition is used. For other cores with Yebes spectra the 3σ value is used to estimate N based on the LTE-predicted brightest $4_{0,4} - 3_{0,3}$ transition. And, for the remaining cores, with constraints from just the ARO 12 m data, we use 3σ values based on

the noise level from the 94.27 GHz line, the $10_{0,10}-9_{0,9}$ transition. Our N estimates range from $0.18-0.72\times10^{12}\,\mathrm{cm}^{-2}$. The median, however, is $0.27\times10^{12}\,\mathrm{cm}^{-2}$ and in only core 715 is the higher value of $0.72\times10^{12}\,\mathrm{cm}^{-2}$ found from the line intensity of the $4_{2,3}-3_{2,2}$ transition where, according to LTE estimates, should be $\sim 5-8\times$ weaker than the other 4-3 transitions. As is assumed for CH₃CN, we have calculate our N values where f=1 and if instead an average value from the CH₃OH analysis is applied, i.e. f=0.4, this would increase our N values by a factor of 2.5.

C7 Methyl Formate, HCOOCH₃

HCOOCH₃ is an asymmetric rotor with internal rotation due to its methyl group, CH₃, which splits rotational levels into A and E substates (as in CH₃OH and CH₃CHO). Laboratory spectroscopy in the frequency range described here has been detailed in Bauder (1979), Karakawa et al. (2001), Ogata et al. (2004), and Ilyushin, Kryvda & Alekseev (2009). Collisional rates for the A-state transition of HCOOCH₃ are also available (Faure et al. 2014; van der Tak et al. 2020). We therefore use RADEX in our estimates of the column density for the Yebes 40 m sub-sample of cores. As done for CH₃OH and CH₃CN, a grid of RADEX models are run and minimized to find a best-fitting N while fixing the volume density, $n_{\rm H_2}$, and the kinetic temperature, T_k , (columns 9 and 10 in Table 1).

For core 326 we are again in a position where we have multiple transitions that could potentially span a wide enough frequency range where the beam size varies enough so it is possible to try and account for the true filling factor, f. We run the minimization procedure for the detected $3_{0,3} - 2_{0,2}$ A transition at 36.102 GHz, the $3_{2,2} - 2_{2,1}$ transition at 36.657 GHz, and the $4_{0,4} - 3_{0,3}$ transition at 47.536 GHz, which have beam sizes of 50, 49, and 38 arcsec, respectively. If we assume the emission is coming from the same source size as found from CH₃OH constraints, i.e. for core 326 this is $\theta_{\rm src} = 51.5$ arcsec, the minimized N value for the transitions are in slightly worse agreement (e.g. between the $3_{0.3} - 2_{0.2}$ and $4_{0.4} - 3_{0.3}$ transitions by a factor of 1.6) than for the f = 1 case (by a factor of 1.3). If the minimization code is then run for a variety of $\theta_{\rm src}$ values, we find $\theta_{\rm src} \gg \theta_{\rm beam}$ is still the best match, i.e. when f = 1. This could suggest that the CH₃OH emission does not trace the HCOOCH₃ emission, at least for the core 326, or that this beam size range is not wide enough to set a strong constraint. Since an f = 1 is a better fit to the data for core 326, compared to assuming the methanol source size, and we have no other f constraints from the remaining cores, we adopt the assumption that f = 1 in our calculations for all of the cores (note: if f = 0.4 is assumed N values increase by factors of 2.4-2.5).

To help remedy the disagreement between the $3_{0,3} - 2_{0,2}$ and $4_{0,4} - 3_{0,3}$ transitions for core 326 (see Table C6), we also attempt to fit simultaneously all A transitions while letting $n_{\rm H_2}$ and T_k vary, finding elevated T_k values more consistent with $\sim 20\,\rm K$ (see Appendix D for more details). Still, the N values derived in this method are consistent (within less than a factor of 2) with the median N derived calculated from minimizing each transitions separately and thus for consistency we report for each core the N from our fixed $n_{\rm H_2}$ and T_k , calculations.

It is in Table C6 where the RADEX derived column densities, N, excitation temperatures, $T_{\rm ex}$, and opacity, τ , values are listed for each of the detected transitions in cores 264, 321, 326, 715, and 768. Note for core 768 only the E-state $4_{1,4} - 3_{1,3}$ transition is detected and therefore used to constrain N. For the remaining cores, an upper limit

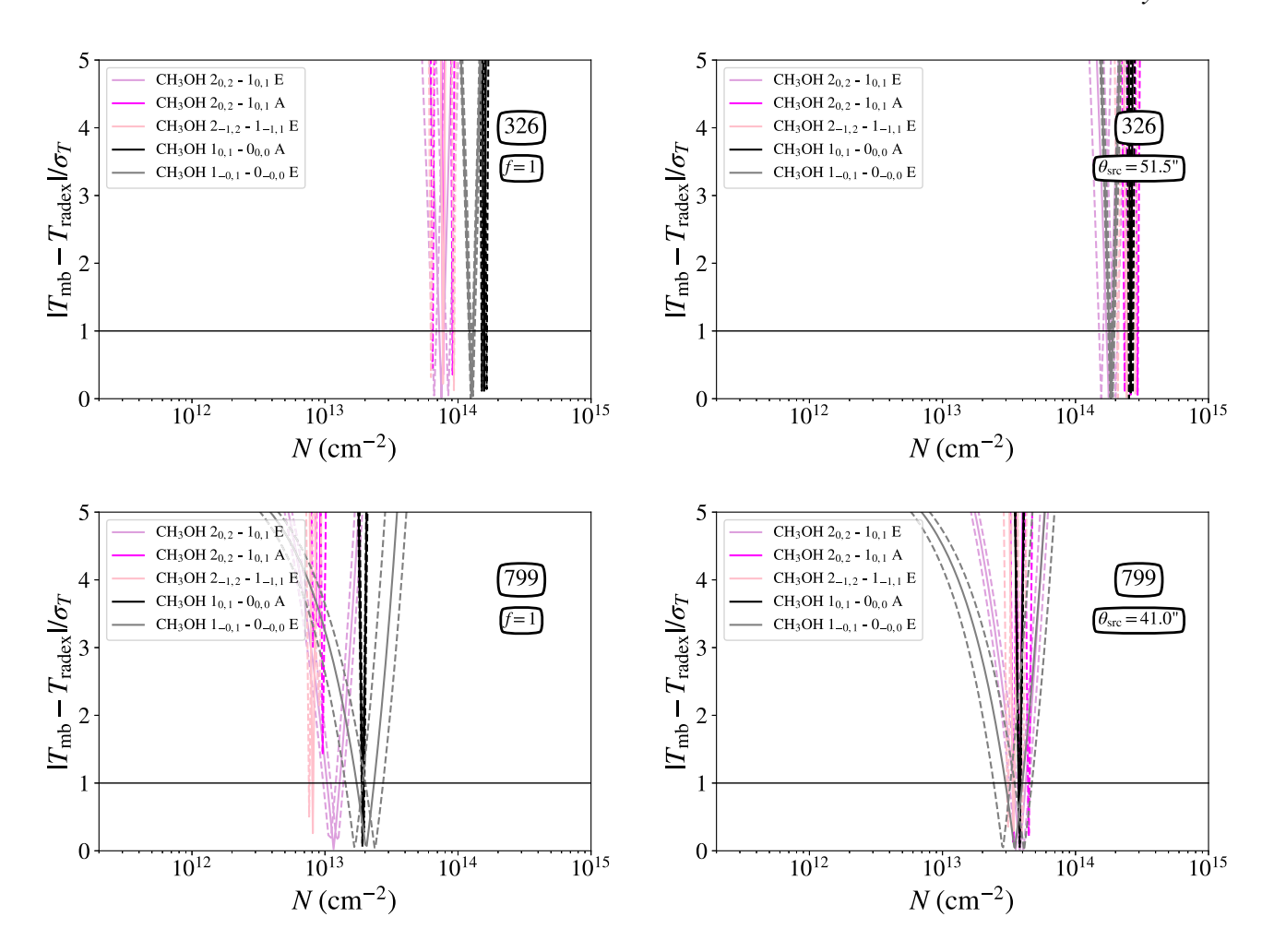


Figure C1. Representative RADEX CH₃OH minimization plots for cores 326 (top) and 799 (bottom). Plotted in each panel is the difference in the observed brightest temperature, $T_{\rm mb}$, and the RADEX-derived brightness temperature, $T_{\rm radex}$, divided by the rms level, σ_T , versus the RADEX-derived column density, N. When the observations best-match the RADEX model, $|T_{\rm mb}-T_{\rm radex}|/\sigma_T$ is minimized and the best N is found while $T_{\rm ex}$ is being optimized for each transition. Solid lines reflect which CH₃OH transition is plotted (ARO 12 m transitions in shaded of pink, Yebes 40 m transitions in shades of black) and the dashed lines represent the spread in error. In the left panels a standard filling factor, f=1, is assumed and in the right panels the minimization is shown when the best-fitting source size, $\theta_{\rm src}$, is found (for core 326 $\theta_{\rm src}=51.5$ arcsec and core 799 $\theta_{\rm src}=41.0$ arcsec).

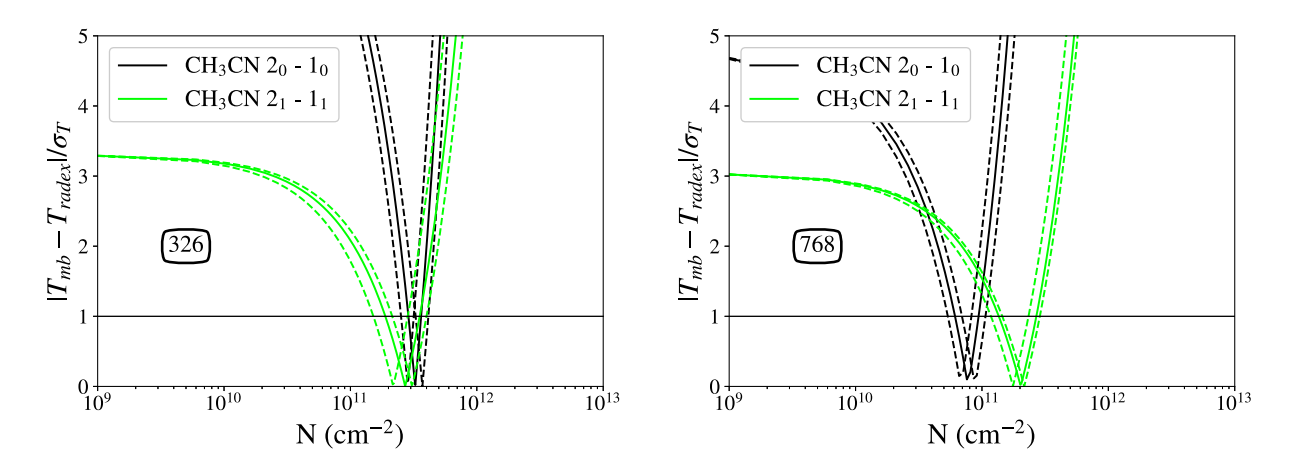


Figure C2. RADEX minimization plots for CH₃CN for the two extreme cases where (top panel) for core 326 both 2-1 lines agree very well, within a factor of 1.2, and (bottom panel) for core 768 when the 2-1 lines differ by a factor of 2.6 (bottom panel). Plotted in each panel is the difference in the observed brightest temperature, $T_{\rm mb}$, and the RADEX-derived brightness temperature, $T_{\rm radex}$, divided by the RMS level, σ_T , versus the RADEX-derived column density, N. When the observations best-match the RADEX model, $|T_{\rm mb}-T_{\rm radex}|/\sigma_T$ is minimized and the best N is found. The dashed lines represent the spread in error.

Table C5. Column densities: CH₂CHCN.

Core # ¹	CH₂CHCN				
(Herschel)	$N (\times 10^{12} \text{ cm}^{-2})$	$T_{\rm ex}\left({\rm K}\right)$			
54	< 0.686	7.39			
67	< 0.286	7.39			
130	< 0.884	7.39			
231	< 0.720	7.39			
256	< 0.735	7.39			
264	$0.227 {}^{+0.055}_{-0.055}$	8.66			
317	< 0.212	12.3			
321	< 0.153	12.5			
326	< 0.192	13.2			
339	< 0.833	7.39			
344	< 0.833	7.39			
355	< 0.752	7.39			
398	< 0.734	7.39			
413	$0.283 ^{+0.054}_{-0.054}$	6.54			
414	< 0.840	7.39			
479	< 1.10	7.39			
491	< 0.749	7.39			
504	< 0.131	7.39			
543	< 0.848	7.39			
615	< 0.156	5.93			
627	< 0.169	6.29			
642	< 1.51	7.39			
656	< 0.929	7.39			
657	< 1.33	7.39			
658	< 0.368	7.39			
709	$0.269^{+0.040}_{-0.040}$	8.71			
715	$0.727^{\ +0.143}_{\ -0.143}$	9.22			
739	< 0.963	7.39			
746	$0.181 ^{+0.036}_{-0.036}$	7.02			
747	< 1.80	7.39			
752	< 0.145	5.57			
768	< 0.118	7.14			
780	< 1.04	7.39			
799	< 0.106	5.80			
800	< 0.159	8.67			

Note. ¹ The cores observed with both the ARO 12 m and Yebes 40 m are bolded. For the italicized cores 67 and 658, the RMS is lower at \sim 2 mK.

for *N* is derived from the RADEX grid where the peak $3_{0,3} - 2_{0,2}$ intensity from the model equals 3σ to give the tightest constraint.

C8 Dimethyl ether, CH₃OCH₃

For CH₃OCH₃, a more complex asymmetric rotor with two methyl groups, the rotational levels are are split into AA, EE, EA, and AE substates (spectroscopic details in Durig, Li & Groner 1976; Lovas, Lutz & Dreizler 1979; Endres et al. 2009). We use only the brightest EE state to calculate column densities using the CTEX and LTE methods. Because we do not know how extended the emission is, we assume f = 1. For core 326 there are two bright EE transitions, $3_{1,2} - 3_{0,3}$ and $4_{1,3} - 4_{0,4}$, with a large enough E_u gap, at 7 K and 11 K, respectively, that the CTEX method can constrain both N and $T_{\rm ex}$ (Table C7). Note that if instead we do assume the CH₃OH source size found for core 326, our N

Table C6. Column densities: RADEX Results for HCOOCH₃ A.

		HCOOCH ₃ A	
Core #	Transition	N	T_{ex}
(Herschel)		$(\times 10^{12} \text{ cm}^{-2})$	(K)
264	$4_{1,4} - 3_{1,3}$	$2.51^{\ +0.55}_{\ -0.55}$	10.6 ^a
	$4_{0,4} - 3_{0,3}$	$2.31^{+0.80}_{-0.75}$	10.7^{a}
317	$3_{0,3} - 2_{0,2}$	< 1.26	14.3
321	$4_{1,4} - 3_{1,3}$	$7.26^{+1.25}_{-1.25}$	12.6^{a}
326	$3_{2,2} - 2_{2,1}$	$8.16^{+1.15}_{-1.10}$	12.4 ^a
	$3_{0,3} - 2_{0,2}$	$1.26^{+0.30}_{-0.30}$	12.5^{a}
	$4_{0,4} - 3_{0,3}$	$5.36^{+0.95}_{-0.95}$	12.3^{a}
413	$3_{0,3} - 2_{0,2}$	< 1.16	11.1
504	$3_{0,3} - 2_{0,2}$	< 1.16	10.0
615	$3_{0,3} - 2_{0,2}$	< 1.21	11.0
627	$3_{0,3} - 2_{0,2}$	< 1.11	13.9
709	$3_{0,3} - 2_{0,2}$	< 1.21	14.8
715	$3_{0,3} - 2_{0,2}$	$1.26^{+0.60}_{-0.50}$	16.5^{a}
746	$3_{0,3} - 2_{0,2}$	< 1.16	11.2
752	$3_{0,3} - 2_{0,2}$	< 1.06	18.2
768	$4_{1,4} - 3_{1,3} E^*$	$1.71 ^{\ +0.05}_{\ -0.05}$	10.5^{a}
799	$3_{0,3} - 2_{0,2}$	< 0.91	11.1
800	$3_{0,3} - 2_{0,2}$	< 1.36	12.3

*Note.** The peak intensity from the detected E-state is used to constrain N, as no A-state transition is detected for this core. ^a RADEX associated errors for these $T_{\rm ex}$ values are < 0.001.

Table C7. Column densities: CH₃OCH₃ EE.

Core #1	CH ₃ OCH	I ₃ EE	
(Herschel)	$N (\times 10^{12} \text{ cm}^{-2})$	$T_{\rm ex}$ (K)	
264	4.54±0.48	11.4	
317	< 2.04	11.4	
321	5.91 ± 0.72	11.4	
326	4.32 ± 0.57	11.4 ± 5.1	
413	< 1.77	11.4	
504	< 1.21	11.4	
615	< 1.72	11.4	
627	7.46 ± 0.72	11.4	
709	< 1.75	11.4	
715	< 1.90	11.4	
746	< 1.60	11.4	
752	< 1.32	11.4	
768	< 1.24	11.4	
799	< 1.67	11.4	
800	< 1.53	11.4	

Note. ¹ Calculation for Core 326 done via the CTEX method, the remaining with the LTE method assuming the same $T_{\rm ex}$ value. For all cores f=1.

increases by a factor of 2, to $N = 9.47 \pm 4.05 \times 10^{12}$ cm⁻² for a $T_{\rm ex} = 6.02 \pm 1.8$ K. Using the constraints from the f = 1 case, at $T_{\rm ex} = 11.4$ K the N for the remaining cores is constrained, which range from $N = 4.54 - 7.46 \times 10^{12}$ cm⁻² (Table C7).

APPENDIX D: PHYSICAL PARAMETERS FROM RADEX CALCULATIONS

The sub-sample of 15 cores from the Yebes 40 m data have enough transitions (>1) for each of the CH₃OH A and E substates that we can attempt to independently constrain a volume density, $n(H_2)$, and

Table D1. RADEX derived best-fitting physical parameters.

Molecule	Core #	T_{k}	$n(H_2)$	N	T_{ex}	τ	
	(Herschel)	(K)	(10^5 cm^{-3})	(cm^{-2})	(K)		$\frac{ T_{\rm mb} - T_{\rm radex} }{\sigma_T}$
CH ₃ OH E	264	6, 5, 6	0.33e5, 1.5e5, 0.13e5	16e13, 16e13, 37e13	5, 5, 5	2.7, 2.7, 6.7	< 2
	317	10, 20, 21	2.8e5, 2.8e5, 2.8e5	10e13, 10e13, 10e13	9, 19, 20	0.637, 0.193, 0.176	< 1
	321	7, 6	2.8e5, 1.5e5	10e13, 16e13	6, 6	0.992, 1.956	< 2
	326	9, 10	0.45e5, 0.18e5	37e13, 57e13	7, 7	2.3, 3.9	< 2
	413	13, 11, 7	0.33e5, 0.61e5, 0.45e5	2.9e13, 2.9e13, 4.5e13	8, 8, 5	0.36, 0.32, 0.88	< 0.8
	504	11	0.18e5	10e13	6	1.8	< 1
	615	13, 12, 12, 9	0.45e5, 0.61e5, 0.18e5, 1.0e5	4.5e13, 4.5e13, 6.9e13, 6.9e13	8, 9, 6, 6	0.526, 0.507, 1.2, 1.2	< 1
	627	5, 5, 6, 6	1.1e5, 1.5e5, 0.18e5, 0.13e5	6.9e13, 6.9e13, 10e13, 16e13	5, 5, 5, 5	2.6, 2.5, 4.2, 6.3	< 2
	709	7	2.8e5	10e13	7	1.15	< 1
	715	14, 20	1.1e5, 1.1e5	4.5e13, 4.5e13	11, 18	0.273, 0.146	< 0.4
	746	21, 17	0.33e5, 0.13e5	4.5e13, 6.9e13	12, 7	0.306, 1.0	< 0.4
	752	8, 8	1.1e5, 0.18e5	6.9e13, 16e13	7, 5	0.910, 3.0	< 2
	768	10	0.61e5	1.9e13	7	0.232	< 0.5
	799	12, 11	0.33e5, 0.45e5	4.5e13, 4.5e13	8, 8	0.913, 0.8829	< 1
	800	16, 11	0.61e5, 0.33e5	6.9e13, 10e13	12, 7	0.465, 1.4	< 1
CH ₃ CN	326	10, 9	2.8e5, 3.7e5	0.29e12, 0.29e12	10, 9	0.003, 0.004	< 0.15
	413	16	0.13e5	0.29e12	5	0.015	< 0.2
	709	22, 20	0.10e5, 0.13e5	0.69e12, 0.69e12	4, 5	0.028, 0.026	< 1.2
	715	15, 16	0.10e5, 0.10e5	0.45e12, 0.45e12	4, 4	0.025, 0.023	< 0.15
	746	6	0.13e5	0.45e12	4	0.034	< 0.15
	752	21, 22	0.10e5, 0.10e5	0.29e12, 0.29e12	4, 4	0.012, 0.011	< 2
	768	22	0.13e5	0.13e12	5	0.003	< 0.7
HCOOCH ₃ A	264	21,19,18	1.1e5, 1.5e5, 2.1e5	2.9e12, 2.9e12, 2.9e12	21, 19, 18	0.001, 0.001, 0.001	< 0.1
	326	22, 21	1.1e5, 1.5e5	2.9e12, 2.9e12	22, 21	0.0007, 0.0008	< 4.1

Note. If multiple models fit the minimization criteria (column 8) they are listed sequentially in the table. Note the T_{ex} and τ values for CH₃OH from the $2_{-1,2} - 1_{-1,1}$ fit, CH₃CN from the $2_0 - 1_0$ fit, and for HCOOCH₃ A from the $4_{0,4} - 3_{0,3}$ fit.

kinetic temperature, T_k while also fitting for N. In this exercise, we create a model suite with a a range of T_k from 3 to 23 (intervals of 1 K), with $n(H_2)$ sampled evenly in log space from 4 to 6.5 (20 grid points), and N sampled evenly in log space from 12 to 15.5 (20 grid points). Models (8000 total) are minimized over $|T_{mb} - T_{radex}|/\sigma_T$ (as in Section C1) for the two 2 – 1 E-state transitions observed with the same beam size from ARO 12 m observations. We also include in our inputs the best-fitting source sizes derived from our analysis in the main text (from minimizing over the $2_{0,2} - 1_{0,1}$ A and $1_{0,1} - 0_{0,0}$ A transitions). In Table D1 we list the best-fitting models. Considering we sample a much coarser grid, we find N values in general consistent, within factors <3, when compared to our fixed $n(H_2)$ and T_k method (listed in Table C1).

For a handful of cores (seven total) we can simultaneously fit the $2_1 - 1_1$ and $2_0 - 1_0$ lines of CH₃CN by running a grid with a range of T_k from 3 to 23 K (intervals of 1 K), with $n(H_2)$ sampled evenly in log space from 4 to 6.5 (20 grid points), and N sampled evenly in log space from 10 to 13.5 (20 grid points). We find N values consistent,

within factors <3, when compared to our fixed $n(H_2)$ and T_k method (listed in Table C4). Our best-fitting T_k values span a wide range, however, from 6 - 22 K when minimized (see Table D1).

In the case of HCOOCH₃, there are two cores (264 and 326) with multiple A state transitions we can use to attempt to constrain T_k and $n(H_2)$. We run our grid with a range of T_k from 3 to 23 (intervals of 1 K), with $n(H_2)$ sampled evenly in log space from 4 to 6.5 (20 grid points), and N sampled evenly in log space from 11 to 14.5 (20 grid points).

We find for cores 264 and 326 they are both minimized for N at 2.9×10^{12} cm⁻², which is consistent with the median values derived in the main text from Table C6 within a factor of 2 (see Table D1). We do find $2 \times$ higher T_k values, ~ 20 K, than what has been derived from NH₃ as well as $n(H_2)$ values varying within a factor of 3 when compared to our beam-averaged assumption (see Table 1 for reference).

This paper has been typeset from a TEX/LATEX file prepared by the author.